Search for exotic bound states and measurement of the (anti-)alpha production yield in Pb–Pb collisions with ALICE at the LHC (CERN)

Suche nach exotischen gebundenen Zuständen und Messung der Produktionsrate von (Anti-)Alpha in Pb–Pb Kollisionen mit ALICE am LHC (CERN)
Dem Fachbereich Physik der Technischen Universität Darmstadt zur Erlangung des Grades eines Doktors der Naturwissenschaften (Dr. rer. nat.)
genehmigte Dissertation von M. Sc. Nicole Alice Löher geb. Martin aus Wiesbaden
Tag der Einreichung: 11. Dezember 2017, Tag der Prüfung: 22. Januar 2018
Darmstadt 2018 — D 17

1. Gutachten: Prof. Dr. Braun-Munzinger
2. Gutachten: Prof. Dr. Moore

TECHNISCHE
UNIVERSITÄT
DARMSTADT

Fachbereich Physik
Institut für Kernphysik

Search for exotic bound states and measurement of the (anti-)alpha production yield in Pb–Pb collisions with ALICE at the LHC (CERN)
Suche nach exotischen gebundenen Zuständen und Messung der Produktionsrate von (Anti-)Alpha in Pb–Pb Kollisionen mit ALICE am LHC (CERN)

Genehmigte Dissertation von M. Sc. Nicole Alice Löher geb. Martin aus Wiesbaden

1. Gutachten: Prof. Dr. Braun-Munzinger
2. Gutachten: Prof. Dr. Moore

Tag der Einreichung: 11. Dezember 2017
Tag der Prüfung: 22. Januar 2018

Darmstadt 2018 — D 17

Bitte zitieren Sie dieses Dokument als:
URN: urn:nbn:de:tuda-tuprints-82225
URL: https://tuprints.ulb.tu-darmstadt.de/id/eprint/8222
Jahr der Veröffentlichung der Dissertation auf TUprints: 2018

Für meinen Mann Bastian,
der mir immer zur Seite steht und
mich immer wieder ermutigt hat, diese Doktorarbeit zu schreiben

und

für meine wundervolle Tochter Mara,
die mich auch im größten Stress jeden Tag zum Lachen bringt.

Erklärung zur Dissertation

Hiermit versichere ich, die vorliegende Dissertation ohne Hilfe Dritter nur mit den angegebenen Quellen und Hilfsmitteln angefertigt zu haben. Alle Stellen, die aus Quellen entnommen wurden, sind als solche kenntlich gemacht. Diese Arbeit hat in gleicher oder ähnlicher Form noch keiner Prüfungsbehörde vorgelegen.

Darmstadt, den 26. November 2018

(Nicole Alice Löher)

Abstract

The ALICE detector system has excellent particle identification (PID) capabilities employing a variety of techniques. One of these is the specific energy loss $\mathrm{d}E/\mathrm{d}x$ measurement in the Time Projection Chamber (TPC). The $\mathrm{d}E/\mathrm{d}x$ is different for each particle species and can be used to identify charged particles including also (anti-)nuclei. The time-of-flight method uses the m^2/z^2 distributions (m = mass of the particle, z charge number of the particle), which are determined from the flight time and the length of the particle trajectory measured with the Time-Of-Flight (TOF) detector, and the momentum extracted through combined tracking in the ALICE setup in the mid-rapidity region.

Within this doctoral thesis these techniques are used for the search for two exotic bound states, the $\overline{\Lambda\mathrm{n}}$ bound state and the H-dibaryon, as well as for the measurement of the production yield per unit of rapidity $\mathrm{d}N/\mathrm{d}y$ of alpha and anti-alpha particles. Both, the searches for the exotica and the measurement of the (anti-)alpha, are performed on data from Pb–Pb collisions at $\sqrt{s_{\mathrm{NN}}} = 2.76$ TeV.

The searches for the two investigated exotica are carried out in the decay channel $\overline{\Lambda\mathrm{n}} \rightarrow \overline{\mathrm{d}} + \pi^+$ and $\mathrm{H} \rightarrow \Lambda + \mathrm{p} + \pi^-$. The different decay products are identified using the specific energy loss measurements in the TPC and their invariant mass is determined. For both investigated bound states no signals are observed in the resulting invariant mass distributions. Therefore, upper limits on the production rates are estimated for eight different assumed lifetimes between 4 cm and 3 m. In addition, the upper limits are determined independent of the branching ratio of the investigated decay channel and are compared to different theory predictions.

The alpha particle is the heaviest nucleus produced and detected during ultra-relativistic heavy-ion collisions at LHC energies and the anti-alpha is even the heaviest anti-nucleus observed so far at all. The particles are identified using the $\mathrm{d}E/\mathrm{d}x$ measurement in the TPC and the m^2/z^2 distributions determined with the measurements of the TOF. The efficiency × acceptance is determined using a Monte Carlo production. As the observed statistics does not allow for the determination of the transverse momentum p_{T}-spectrum, a Blast-Wave extrapolation is used, which is based on the measurements of the spectra of deuterons and ^{3}He. This allows for the p_{T}-integrated determination of the efficiency. Systematic uncertainties are calculated and the resulting rapidity density $\mathrm{d}N/\mathrm{d}y$ is comparable with the prediction from a thermal model.

Zusammenfassung

Das ALICE Detektorsytem weist verschiedene exzellente Möglichkeiten zur Teilchenidentifizierung auf. Eine dieser Möglichkeiten ist der für jede Teilchensorte verschiedene, spezifische Energieverlust $\mathrm{d}E/\mathrm{d}x$, der in der ALICE Zeitprojektionskammer gemessen wird und zur Identifizierung von geladenen Teilchen und Anti-Teilchen, inklusive (Anti-)Kerne, genutzt werden kann. Eine weitere Teilchenidentifizierungsmethode verwendet m^2/z^2-Verteilungen (m = Masse des Teilchens, z Ladungszahl des Teilchens). Diese Verteilungen werden bestimmt durch die Messung der Flugzeit, der Länge der Flugbahn der Teilchen mit dem Flugzeitdetektor (TOF) und der Messung des Impulses, der aus der kombinierten Spurrekonstruktion im ALICE Aufbau in der mittleren Rapiditäts-Region extrahiert wurde.

In der vorliegenden Doktorarbeit wurden unter anderem diese Techniken benutzt, um nach zwei exotischen gebundenen Zuständen, dem $\overline{\Lambda\mathrm{n}}$ und dem H-dibaryon, zu suchen und um die Produktionsrate von Alpha and Anti-Alpha Teilchen zu messen. Für alle vorgestellten Analysen wurden Daten aus Pb–Pb Kollisionen bei $\sqrt{s_{\mathrm{NN}}} = 2.76$ TeV ausgewertet.

Die Suchen nach den beiden untersuchten exotischen Teilchen werden in den Zerfallskanälen $\overline{\Lambda\mathrm{n}} \rightarrow \overline{\mathrm{d}} + \pi^+$ und H-dibaryon $\rightarrow \Lambda + \mathrm{p} + \pi^-$ durchgeführt. Die verschiedenen Tochterteilchen werden mit Hilfe des spezifischen Energieverlustes in der TPC identifiziert und ihre invariante Masse wird bestimmt. In beiden Fällen wurde kein Signal in der resultierenden Verteilung der invarianten Massen gefunden. Daher wurden obere Grenzen für die Produktionsraten für acht verschiedene mögliche Lebensdauern zwischen 4 cm und 3 m bestimmt. Außerdem wurden die oberen Grenzen unabhängig von dem Verzweigungsverhältnis des untersuchten Zerfallskanals bestimmt und mit mehreren theoretischen Vorhersagen verglichen.

Das Alpha-Teilchen ist der schwerste Kern, der bisher in ultra-relativistischen Schwerionenkollisionen bei LHC Energien nachgewiesen werden konnte, wobei das dazugehörige Anti-Teilchen sogar das schwerste seiner Art ist, das jemals beobachtet wurde. Die Teilchen werden mit Hilfe der $\mathrm{d}E/\mathrm{d}x$ Messung in der TPC und der m^2/z^2-Verteilung, die aus den Messungen des Flugzeitdetektors bestimmt wurden, identifiziert. Für die Effizienzkorrektur wurde eine Monte Carlo Produktion mit Alpha und Anti-Alpha Teilchen angereichert. Da die Anzahl der detektierten Teilchen zu klein ist, um ein Transversalimpulsspektrum zu messen, wurde eine Blast-Wave Extrapolation, die auf den Messungen der Spektren von Deuteronen und ^{3}He beruht, benutzt. Diese erlaubt die Bestimmung der p_{T} integrierten Effizienz. Desweiteren wurden systematische Fehler bestimmt. Die resultierenden Rapiditätsdichten $\mathrm{d}N/\mathrm{d}y$ sind in guter Übereinstimmung mit den Vorhersagen des thermischen Modells.

Contents

1 Introduction

This doctoral thesis is organized as follows. After a short overview of basic principles and models in this chapter, the experimental apparatus of ALICE is introduced (chapter 2) and different particle identification methods are explained (chapter 3). In the main parts of the thesis, the analysis for the search of two exotic bound states, the Λn bound state and the H-dibaryon (chapter 4), followed by the measurement of alpha and anti-alpha particles (chapter 5) are presented. Finally the obtained results are discussed (chapter 6) and compared to theoretical models (which are introduced in this chapter).

The present understanding of the fundamental fermions and the forces between them is manifested in the standard model of particle physics. According to this model, the fundamental fermions, which are the constituents of matter, are quarks and leptons. The only force that is not included in the standard model is gravity, because there exists no theory yet, which can include the quantisation of the gravitation in a reasonable manner. The standard model has 26 external parameters, among which are the masses of the six quarks, the six leptons and the three vector bosons ($W^{+/-}$ and Z). In addition to them there are two coupling constants: the electromagnetic coupling constant α, which represents the strength of the electromagnetic interaction, and the strong coupling constant α_s, which represents the strength of the strong interaction between quarks and gluons. Finally, there are the eight mixing parameters, which are used to describe the change of flavor of quarks or neutrinos, and one scale parameter (Λ_{QCD}).

Leptons				**Quarks**		
flavor	**mass [GeV/c^2]**	**electric charge [e]**	**family**	**flavor**	**approx. mass [GeV/c^2]**[1]	**electric charge [e]**
electron neutrino ν_e	$< 2 \cdot 10^{-9}$	0	1	up u	0.002	2/3
electron e	0.000511	-1		down d	0.005	$-1/3$
myon neutrino ν_μ	< 0.00019	0	2	charm c	1.3	2/3
myon μ	0.106	-1		strange s	0.1	$-1/3$
tau neutrino ν_τ	< 0.0182	0	3	top t	173	2/3
tau τ	1.777	-1		bottom b	4.2	$-1/3$

Table 1.1: The fundamental fermions (properties taken from [1]).

Leptons and quarks each exist in six flavors, which are organized in three families (see Table 1.1). Leptons ("light" particles) can be observed freely in nature, whereas quarks are confined within mesons ("middle" particles, built out of a quark and an anti-quark) and baryons ("heavy" particles, which are built out of three quarks). All fermions are particles with half-spin (1/2, 3/2, 5/2,..). Fundamental gauge bosons mediate the forces between the fermions. They carry in contrast to fermions integer-spin (0, 1 or 2). The electromagnetic force is mediated by the photon, whereas the weak force can be either mediated by the two W-bosons (W^+ or W^-) or the Z-boson. Gluons g mediate the strong force. Gravity should be mediated by a hypothetical "Graviton". All four forces and the mediating particles are summarized in Table 1.2. The photon and the gluon are massless particles, whereas the three W- and Z-bosons

---

[1] As the masses of the quarks can not be measured directly (due to the confinement of quarks in hadrons), the masses are not known exactly. The values are instead estimated with different models based on the hadronic observations and calculated numerically.

are massive particles (mass$_{W^{-/+}} = 80.4$ GeV/c^2 [1] and mass$_{Z^0} = 91.2$ GeV/c^2 [1]).

The underlying relativistic field theory for the fundamental electromagnetic force is *QED* or quantum electrodynamics. The underlying relativistic field theory for the strong interaction is called *QCD*, quantum chromodynamics. The underlying gauge symmetries are $U(1)_{EM}$ and $SU(3)_{col}$. Whereas, in QED there is only one electric charge e, in QCD there are three colour charges (red, green and blue). Therefore, also in QED there is only one massless gauge boson, namely the photon. It carries no electric charge and is not self-interacting. On the other hand in QCD there exist eight massless gauge bosons, namely the gluons. They carry the three colour charges or a linear combination of them. There are "only" eight different gluons, because the ninth combination $(1/\sqrt{3})(r\overline{r} + g\overline{g} + b\overline{b})$ is colourless. As the gluons carry colour charge they are also self-interacting. Another big difference is the range of the forces. Whereas the electromagnetic force has in principle an infinite range, the strong force has a very limited range (only a few femtometers (1 fm = 10^{-15} m)). Mediated by gluons, the strong force acts directly between quarks and gluons. It ensures that the nucleons (protons and neutrons) are held together inside the atomic nucleus. It also acts on the confined quarks and gluons inside mesons and baryons. Mesons and baryons are themselves colourless objects.

property	**gravitational interaction**	**weak interaction**	**electromagnetic interaction**	**strong interaction**
acts on:	mass - energy	flavor	electric charge	color charge
experiencing particles:	all particles	quarks and leptons	electrically charged particles	quarks and gluons
occurs in:	massive particles massive bodies	radioactive beta decay	atomic shell	atomic nucleus
mediating boson	graviton[2]	W^+,W^-,Z^0	photon γ	gluons
intensity of force relative to the strong force	10^{-38}	10^{-5}	10^{-3}	1

Table 1.2: Summary of the four fundamental forces.

The different phases of nuclear matter can be summarized in the QCD phase diagram, where the temperature T is shown on the y-axis and the baryo-chemical potential μ_{B} on the x-axis, see Figure 1.1. Its understanding is a key topic of modern nuclear physics. Normal (nuclear) matter has a $\mu_{\text{B}} = 938$ MeV. If either T or μ_{B} or both are changed, a hadron gas is formed, where the quarks and gluons are still confined inside hadrons. At high T or μ_{B} the quarks and gluons are no longer confined inside hadrons, but are freely moving inside the so called quark-gluon plasma (QGP). The phase transition between the confined and the deconfined state can either be of first or second order or it can be a crossover. In the present understanding, supported by lattice calculations [2, 3], at low μ_{B} close to zero the phase transition is a "crossover" and therefore not a true phase transition in the thermodynamic sense (indicated with the dashed line in Figure 1.1). Whereas at higher μ_{B} there is a phase transition of first order expected (indicated with the full line in Figure 1.1). The two phase transitions should be connected with a critical point, which has not been found yet experimentally. At a critical point a first order phase transition and a crossover takes place. The critical point is the end point of a first order phase transition (indicated with the full line in Figure 1.1). There are also considerations about a triple point, which

---

[2] Not yet observed.

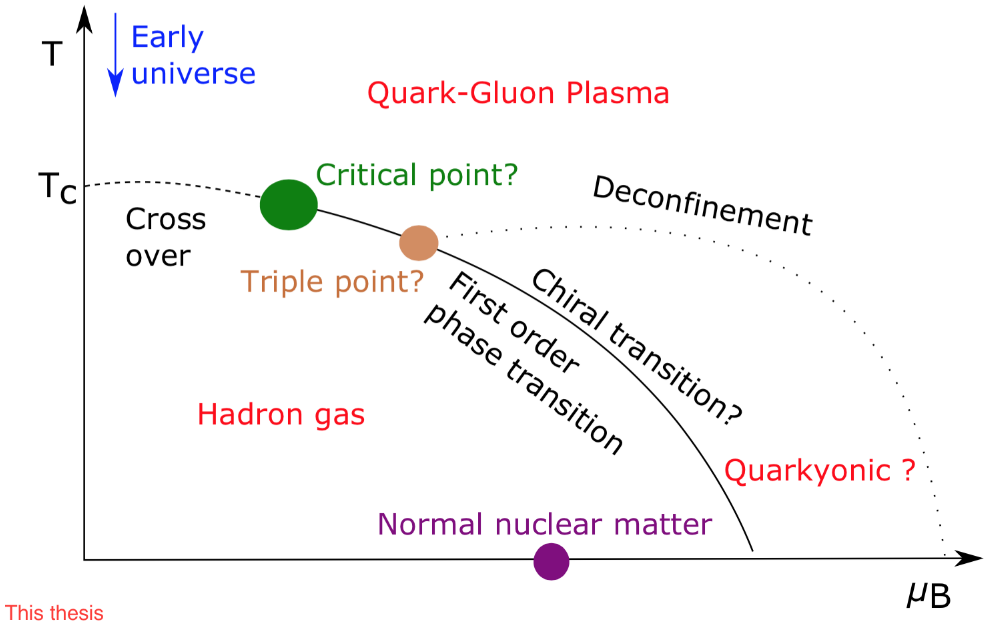

Figure 1.1: The QCD phase diagram.

would separate the QGP, hadron gas and quarkyonic phase. The temperature for the phase transition between the hadron gas and the QGP is called (pseudo-)critical temperature T_c. Most recent thermal analyses (see section 1.4) of the experimental available data as well as lattice calculations suggest a $T_c \approx$ 156 MeV [4, 5] at $\mu_B = 0$ or close to zero.

1.1 Light nuclei and hypernuclei

The study of nuclei and hypernuclei have a very long tradition in nuclear physics, but only high energy heavy-ion collisions (HIC) offer the unique possibility to look as well for their anti-particles. In comparison to nuclei, which are built out of neutrons (udd) and protons (uud), in hypernuclei one or more of the bound neutrons is exchanged with a hyperon, which contain one or more strange quarks (s). Hyperons are unstable and decay via the weak interaction. The lightest hyperon is the Λ-particle (uds) and the lightest observed hypernucleus is the hypertriton (pnΛ). It has a mass of 2.99 GeV/c^2 and a lifetime similar to the lifetime of the free Λ-particle [6]. Until now the anti-particles of nuclei up to anti-alpha as well as the anti-hypertriton have been measured in HIC. Both the heaviest anti-nucleus (anti-alpha) as well as the only anti-hypernucleus (anti-hypertriton) observed so far have been first measured by the STAR experiment at BNL [7, 8]. Recently the measurements of deuteron, triton and ^{3}He in pp and Pb–Pb collisions [9] as well as the hypertriton measurements [6] in Pb–Pb collisions with the ALICE experiment have been published. On the other hand a confirmation of the measurement of alpha and anti-alpha particles in HIC has not been done yet. This measurement is part of this thesis. The ALICE measurement is not only a repetition of the results from the STAR collaboration, but are the first results of alpha and anti-alpha measurements at the energy of $\sqrt{s_{\mathrm{NN}}} = 2.76$ TeV and therefore also will be an additional particle[3], which can be used to test the predictions of the different production models described below.

---

[3] In addition to the already measured lighter particles [6, 9–13]

1.2 Exotica

The two exotic bound states investigated in this doctoral thesis are the Λn bound state and the H-dibaryon. This states could either be true bound states or resonance states. Besides the search of two new bound states and the first measurement of a six quark state, the finding or exclusion of these particles will help in the understanding of the Λ-nucleon and Λ-Λ interaction. So far there is very little knowledge about these interactions, which is also very important for the understanding of neutron stars [14–17].

The interaction between a Λ and a nucleon has been already studied by Downs and Dalitz in 1959 [18]. From their studies it is unlikely that a bound Λ-nucleon system exists. Nevertheless there have been several experimental searches for Λn and Λp states (resonance or bound states) in the past [19–21]. Whereas [19, 20] did not find evidence for a Λp resonance state, the HypHI collaboration recently claimed the observation of a Λn bound state [22]. Although later this observation was corrected to be a resonance [21], this renewed the interest in this topic. Within this doctoral thesis the search for the antiparticle, the $\overline{\Lambda \mathrm{n}}$ bound state, is performed. The investigated decay channel is $\overline{\Lambda \mathrm{n}} \rightarrow \overline{\mathrm{d}} + \pi^+$.

The H-dibaryon is a hypothetical six quark bound state (uuddss). These six quarks either form the bound state directly or are confined in two Λ-particles (uds), which then from the H-dibaryon. The H-dibaryon was predicted by Jaffe in 1977 in a bag model calculation [23]. Since then several experiments [24, 25] have conducted searches for this particle, but so far it has not been found. In addition, no signal has been observed in the measurement of $\Lambda\Lambda$ correlations by the STAR collaboration [26] and a theoretical analysis of this data [27]. On the other hand, recently performed lattice calculations support the idea of a bound $\Lambda\Lambda$-particle, which should be bound by 20-50 MeV/c^2 [28] or by 13 MeV/c^2 [29] depending on the details of calculation. If these lattice calculations are chirally extrapolated to the physical pion mass, the H-dibaryon is found to be unbound by 13 ± 14 MeV/c^2 [30] or it lies close to the Ξp threshold [31]. Within this doctoral thesis the H-dibaryon is investigated in the decay channel H-dibaryon $\rightarrow \Lambda + \mathrm{p} + \pi^-$, while the Λ is reconstructed in the decay channel p + π^-.

The prediction of the thermal model (at a temperature of 156 MeV) (see section 1.4) for the hypertriton rapidity density $\mathrm{d}N/\mathrm{d}y$ agrees with the ALICE measurement [6]. Therefore, also the investigated bound states should be produced with a $\mathrm{d}N/\mathrm{d}y$ predicted by the thermal model, if they are stable against strong decays. As visible in Figure 1.3 the predicted $\mathrm{d}N/\mathrm{d}y$ for the H-dibaryon is a factor of 300 higher as the one of the hypertriton and the Λn should be produced even more often. This relatively high expected yield will allow for the observation of a signal for both exotica in the investigated data, in case these particles exist. The high production rate also compensates for the fact that the analysis of the H-dibaryon requires the reconstruction of four daughter particles in comparison to two daughters in the hypertriton measurement.

1.3 Heavy-Ion collisions

In nature the QGP is believed to have existed directly after the big bang. In order to study its properties it has to be recreated in relativistic HIC. Figure 1.2 shows a schematic illustration of such a collision. First the nuclei (for example Pb ions) are accelerated until they nearly reach the speed of light and have a very high energy of up to a few hundred GeV per nucleon (at the Relativistic Heavy-Ion collider at Brookhaven National Laboratory) or even a few TeV per nucleon (at the Large Hadron collider at the European Organization for Nuclear Research (CERN)). At these conditions the ions are Lorentz contracted. When the two nuclei collide the matter is compressed and heated. The nucleons break up and a fireball (in a pre-equilibrium) is formed. An equilibrium is established (thermalization, $t \lesssim 1\,\mathrm{fm}/c$) a QGP is formed, which further expands and cools down. After $t < 10 - 15\,\mathrm{fm}/c$ hadronization starts, which ends when inelastic collisions stop and the chemical freeze-out happens. At this point the particle

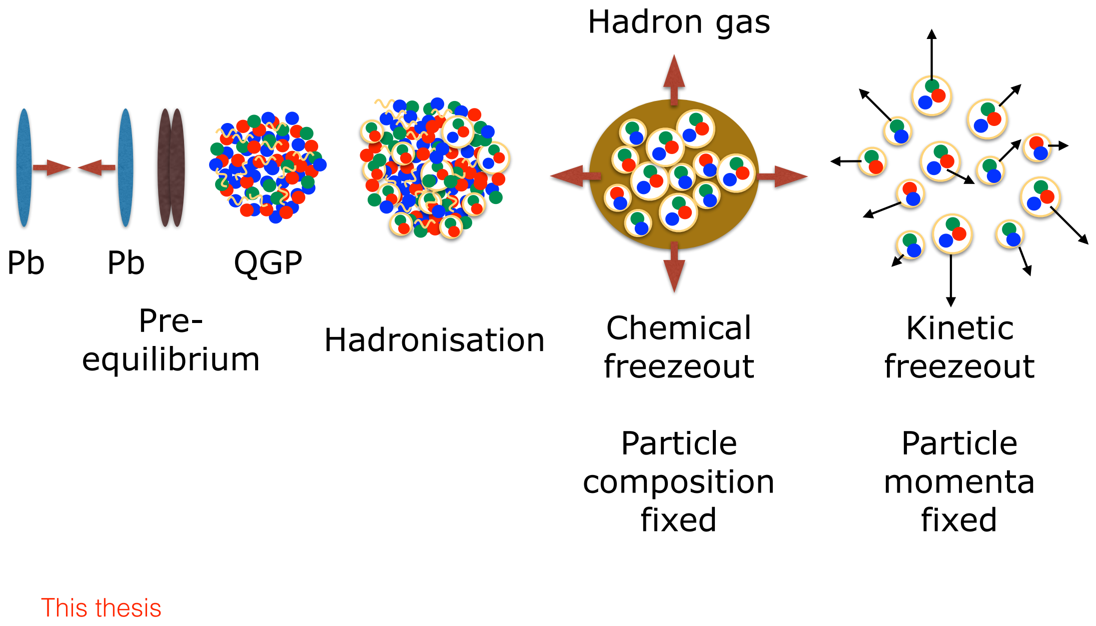

Figure 1.2: Schematic illustration of an heavy-ion collision.

composition is fixed and the quarks and gluons are again confined inside the hadrons. They create a hadron gas, which further expands. After the kinetic freeze-out, also the elastic collisions stop and the momenta of the particles are fixed. These particles can finally be detected, as described chapter 2.

1.4 Production Models

There exist several different models to describe the production yields of particles in a HIC.

Statistical-thermal models [32–35] use, as the name indicates, a statistical ansatz in order to describe the abundance of particle species after a HIC. This ansatz is (usually) based on a grand canonical ensemble, which assumes that all hadrons are produced from a medium in thermodynamic equilibrium, which means from a kinetically and chemically equilibrated state (hadro-chemical equilibrium). All particles are produced at the same temperature (chemical freeze-out temperature T_{ch}) and the same chemical potential (the baryo-chemical potential μ_B). The advantage of these models is, that besides T_{ch} and μ_B, only the volume V is needed as free parameter in order to describe the observed particle production. The three parameters are fixed by fits using the measured particle yields as input. At LHC energies μ_B is close to zero and thus the key parameter is T_{ch}. Therefore, the abundance of the particles can be approximately described by an exponential dependence on the mass m of the particles and the T_{ch}: yield $\mathrm{d}N/\mathrm{d}y \sim \exp\left(-m/T_{\mathrm{ch}}\right)$ [4]. The particle yields are therefore determined by T_{ch}, if the expansion afterwards is isentropic. This idea of an isentropic expansion is supported by the success of the models to describe the observed particle abundances. Consequently, starting from the QGP phase the system

---

[4] The exact formula for the abundance of a particle i with strangeness S_i, baryon number B_i, electric charge Q_i and spin-isospin degeneracy factor g_i is given in equation 8 in [32] as $\frac{VTg_i}{2\pi^2}\sum_{k=1}^{\infty}\frac{(\pm1)^{k+1}}{k}\lambda_i^k m_i^2 K_2\left(\frac{km_i}{T}\right)$ with the modified Bessel function K_2 and $\lambda_i(T,\vec{\mu}) = \exp\frac{B_i\mu_B+S_i\mu_S+Q_i\mu_Q}{T}$.

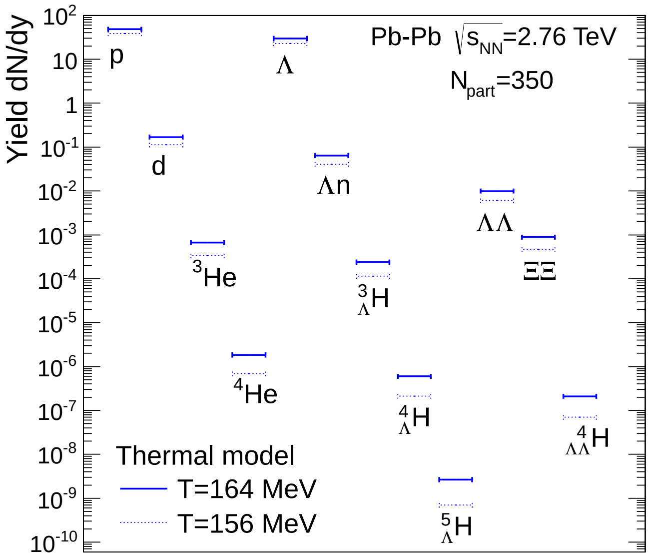

Figure 1.3: dN/dy from the statistical hadronization model [36].

evolves through the phase diagram along isentropes. Besides the chemical freeze-out temperature T_{ch}, the limiting temperature T_{lim}, above which hadrons can not be heated, is of interest and was found to be $T_{\mathrm{lim}} = 159 \pm 2$ MeV [34].

As already mentioned above recent thermal model fits to experimental available data have led to $T_{\mathrm{ch}} \approx 156$ MeV [4]. Using this temperature the measured particle yields of a variety of particles can be described, among which is also the very loosely bound hypertriton, which has a binding energy of only 0.13 MeV [34]. Therefore, this model is expected to properly predict the particle yield of the Λn bound states, the H-dibaryon[5] and the alpha particle. The predictions are summarized in Figure 1.3.

Besides the equilibrium thermal models there also exist non-equilibrium approaches [37, 38]. These approaches have one or two more parameters γ_s and γ_q, as strangeness (and light quarks) are allowed to be in non-equilibrium. They usually lead to lower chemical freeze-out temperatures (∼140 MeV).

Another model to describe the production of particles in HICs is the coalescence picture where particles can be formed by quarks (quark coalescence) or by hadrons (hadron coalescence), which are close in space and have a similar velocity. In this picture for example nuclei, which have been produced at chemical freeze-out can break apart and be recreated again by final-state coalescence. The concept of coalescence was first applied by Butler and Pearson in 1961 and 1963 [39, 40]. In the most simple form of this approach the deuteron to proton ratio in HIC for example increases with increasing multiplicity, as more protons would directly imply a higher production of deuterons.

The result of the search for the H-dibaryon is also compared to predictions from hybrid UrQMD calculations [41]. UrQMD is the abbreviation for Ultrarelativistic Quantum Molecular Dynamics model, which is a microscopic transport model. For these comparisons the UrQMD code uses ideal hydrodynamic calculations for the fireball as input. Afterwards the resulting hydrodynamic cells are converted to particles by the Cooper-Frye equation. The UrQMD code is used to transport the particles between the chemical

---

[5] under the assumption that these are stable against strong decays

and kinetic freeze-out. Therefore, ideally all cross-sections for interaction between all possible particle species need to be implemented, which are however not known.

1.5 Blast-Wave Model

The Blast-Wave model is a phenomenological model, which describes particle spectra (e.g. transverse momentum p_{T}-spectra, transverse mass m_{T}[6]-spectra and rapidity distributions) in heavy-ion collisions [42]. It assumes an expanding source (fireball) in local thermal equilibrium with temperature T. This thermal source is built out of several cells, which move and expand, while they are emitting the particles. The rate of expansion can vary in the different directions and due to this expansion the emitted particles have an additional velocity, which is called flow. The flow in the direction of the beam is called longitudinal flow, whereas the flow due to the expansion of the fireball is called transverse flow. Whereas the longitudinal flow affects the rapidity distributions, the transverse mass spectra are influenced by the transverse flow. The Blast-Wave model has only a few collective variables, among which is the averaged velocity β of the particles at the surface of the fireball and the local kinetic temperature T at freeze-out. This temperature and the flow dynamics are reflected in the shape of the measured spectra. On the other hand, the size of the collision zone and amount of chemical equilibrium among the particle species are connected to the absolute normalisation of the spectra. For example the shapes of the transverse momentum p_{T}-spectra measured with ALICE are indeed described by this model quite well, using only one set of parameters [10]. This works not only for light particles, but also for the deuteron and ^{3}He transverse momentum spectra [9]. Therefore, within this doctoral thesis the Blast-Wave model is used to predict the p_{T}-spectra of two possible bound states and the alpha particle based on measured spectra of lighter hadrons, see chapter 4 and 5.

---

[6] transverse mass $m_{\mathrm{T}} = \sqrt{m^2 + p_{\mathrm{T}}^2}$

2 The Experimental Apparatus

The analysed data have been collected using the ALICE detector system [43] at the **L**arge **H**adron **C**ollider (LHC) at CERN in Geneva, Switzerland. The LHC provides proton and lead (Pb) beams with the highest energies ever reached in the laboratory. ALICE has recorded collisions in three different modi: proton-proton, Pb–Pb or proton-Pb collisions. So far proton-proton collisions at a center-of-mass energy of 900 GeV, 2.76 TeV and 7 TeV, Pb–Pb collisions at a center-of-mass energy of 2.76 TeV and proton-Pb collisions at a center-of-mass energy of 5.02 TeV have been measured during the first run. After the long shutdown one (from spring 2013 to the beginning of 2015), the LHC is back in operation since spring of 2015 and data from proton-proton collisions at 13 TeV and 5.02 TeV as well as Pb–Pb collisions at 5.02 TeV have been collected. For the presented work of this thesis Pb–Pb collisions at 2.76 TeV from the campaign of 2011 have been analysed.

The LHC is hosted in a 27 km long tunnel, which lies at a depth between 50 and 175 meters below the earth's surface at the border between France and Switzerland. The accelerator is divided into eight arcs and eight straight parts of 528 meters each in between. The beams circulate in opposite directions inside two beam pipes, which are contained inside the same vessel. The accelerator is operated at a temperature of 4.5 K, whereas the superconducting dipole and quadrupole magnets, which bend and focus the beams, are even further cooled down to 1.9 K in order to reach the superfluid state of helium. In order to obtain the protons, electrons are removed from hydrogen atoms, whereas a source of vaporized lead provides Pb ions. The particles do not enter the LHC directly, but are accelerated in several smaller machines before: The protons are first accelerated by the linear accelerator LINAC2 and then injected into the PS Booster. The Pb ions are first accelerated by the linear accelerator LINAC3 and the Low Energy Ion Ring (LEIR). Afterwards, both the protons and the Pb ions are further accelerated in the Proton Synchrotron (PS) and the Super Proton Synchrotron (SPS). At the end of this chain the particles have reached an energy of 450 GeV per proton and are finally injected into the LHC. A schematic sketch of the accelerator complex at CERN is shown in Figure 2.1.

The ALICE detector system is located at Point 2 of the LHC in St. Genis-Pouilly in France. Its design is illustrated in Figure 2.2. Most of its sub-detectors are situated in the central barrel inside a large solenoid magnet. The magnet has a magnetic field of up to 0.5 T, which deflects the charged particles. This allows for the measurement of the momentum of the charged particles, which can be determined by the strength of the deflection. In addition to the central barrel there are the single arm backward muon spectrometer and two Zero Degree Calorimeters (ZDC). For the analysis presented in this thesis mainly the Inner Tracking System (ITS), the Time Projection Chamber (TPC), the Time-Of-Flight (TOF) detector as well as the T0 and the VZERO detector are used. Therefore, only these sub-detectors will be discussed in more detail in the following. In addition to these detectors ALICE also has a Transition Radiation Detector (TRD) to separate electrons from pions (and other hadrons), two electromagnetic calorimeters, EMCal+Dcal for efficient triggering on high energy jets and PHOS to investigate jet quenching, a Photon Multiplicity Detector (PMD) to study event shapes and fluctuations and the High Momentum Particle Identification Detector (HMPID). More details on the detectors not used in the analysis presented here can be found in [43].

In order to help understanding the detector geometry as well as the explanations of the analyses described in chapters 4 and 5, the ALICE coordinate system is introduced next followed by the description of the involved sub-detectors.

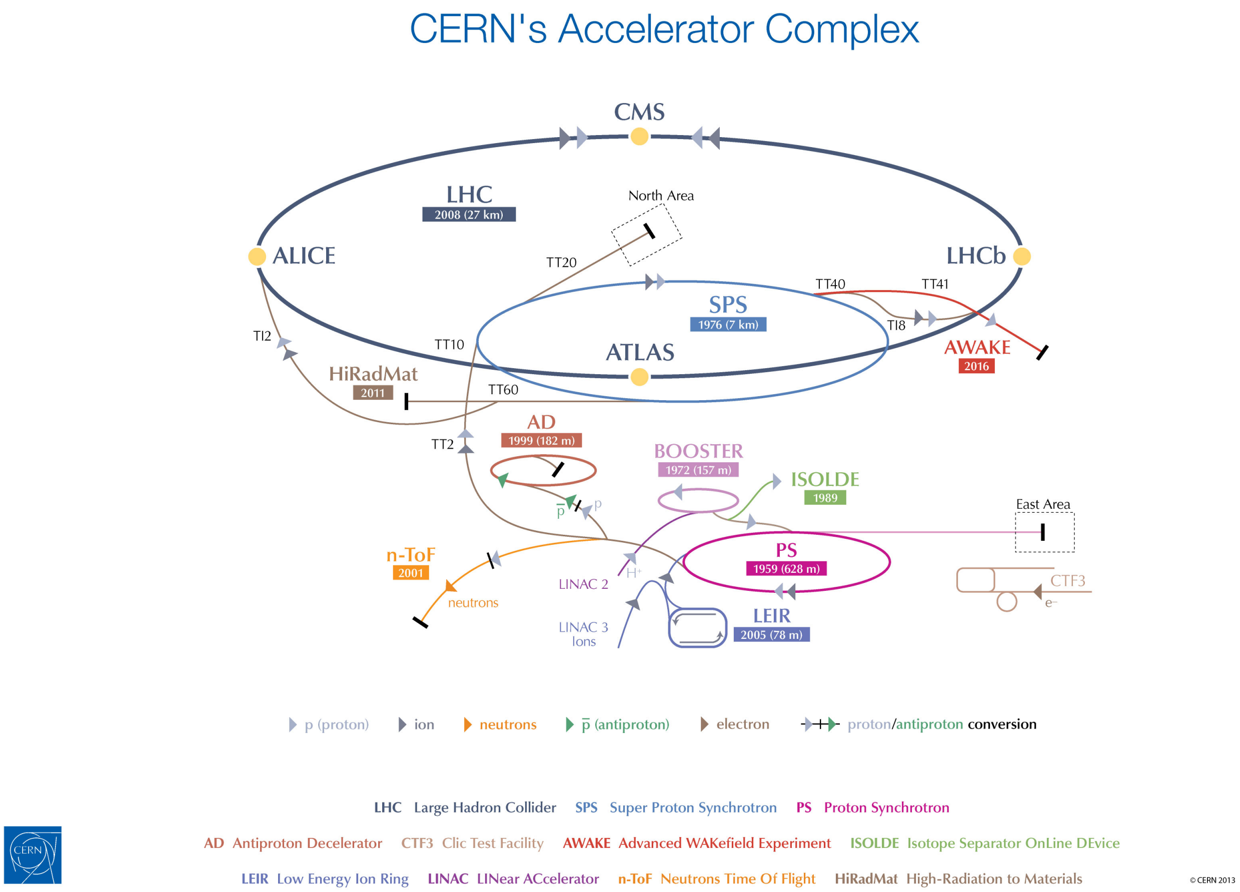

Figure 2.1: Schematic layout of the accelerator complex at CERN [44].

ALICE coordinate system

The ALICE coordinate system [45] is a right-handed orthogonal Cartesian system. It is shown together with the polar coordinates ϕ and θ in Figure 2.2. The origin (x=y=z=0) of the coordinate system is at the interaction point (IP) of the two colliding beams. Parallel to the beam axis and the magnetic field is the z-axis. From the point of origin the positive z-axis points towards the ATLAS experiment, whereas the negative z-axis points towards the CMS experiment. The ALICE muon arm is located at negative z values. Aligned with the local horizon and perpendicular to the beam direction the x-axis is defined. The positive x-axis points to the inside direction towards the accelerator center, while the negative x-axis points outwards. Finally, the positive y-axis points upwards, whereas the negative y-axis points downwards from the point of origin. As the ALICE central barrel has a cylindrical shape it is helpful to define in addition the spherical coordinates r, ϕ and θ. The two angles are defined as follows: The azimuthal angle ϕ increases counter-clockwise from the positive x-axis ($\phi = 0$) to positive y-axis ($\phi = \frac{\pi}{2}$), whereas the polar angle θ increases from the positive z-axis ($\theta = 0$) to the (x,y)-plane ($\theta = \frac{\pi}{2}$). The transformation between the two coordinate systems is given by

$$\begin{aligned} x &= r \cdot \sin\theta \cdot \cos\phi & \qquad r &= \sqrt{x^2 + y^2 + z^2} \\ y &= r \cdot \sin\theta \cdot \sin\phi & \qquad \theta &= \arccos\frac{z}{r} \\ z &= r \cdot \cos\theta & \qquad \phi &= \arctan\frac{y}{x} \end{aligned}$$

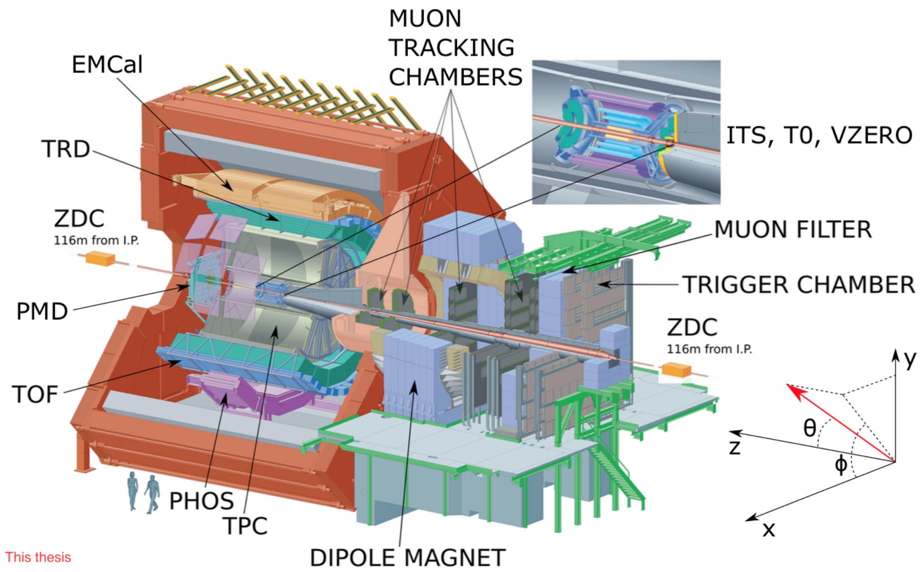

Figure 2.2: The ALICE detector system together with the coordinate system.

The ITS, the TPC as well as the TOF detector cover together a pseudorapidity η interval of $|\eta| \leqslant 0.9$, which is equivalent to ±45°, over the full azimuth.

ITS

The **I**nner **T**racking **S**ystem [46] is the innermost sub-detector. It is placed directly around the beam pipe and consists of six cylindrical layers, which are constructed out of three different types of silicon detectors. The innermost two layers consist of two silicon pixel detectors (SPD) followed by two silicon drift detectors (SDD) and two double-side silicon microstrip detectors (SSD). The four outer layers (SDD and SSD) have an analogue readout for particle identification (PID), which is done via specific energy loss ($\mathrm{d}E/\mathrm{d}x$) measurements in the non-relativistic region (see section 3.1). Due to its position close to the beam pipe the ITS is also used for tracking of low momentum particles, down to $p_\mathrm{T} \approx 100$ MeV/c. However, more important for the analyses performed in the presented thesis, is the precise determination of the primary vertex (collision vertex) and the secondary vertex (decay vertex), which allows for an excellent separation between primary and secondary particles. For particles with high transverse momenta ($p_\mathrm{T} > 1.5$ GeV/c) this separation goes below 50 μm, for particles with low transverse momenta ($p_\mathrm{T} < 200$ MeV/c) this separation goes up to 300 μm [47].

TPC

The **T**ime **P**rojection **C**hamber [48] is a cylindrical gas detector, which surrounds the ITS. The general parameters of the TPC are listed in table 2.1. It has an overall length in beam direction of about 500 cm. The inner radius of the active volume is about 85 cm, whereas the outer radius is about 250 cm. In the middle, orthogonal to the beam pipe a high voltage central electrode divides the TPC into two 2.5 m long drift regions. In addition, the TPC is divided in ϕ into 18 sections of 20° each. In each section an inner and an outer Multi-Wire Proportional Chamber (MWPC) are installed at the endcaps, leading to $18 \times 2 = 36$ readout chambers in each drift region and to 72 readout chambers in the whole TPC. In total, all readout chambers have a gas volume of 90 m^3, which is filled with a gas mixture of 85.7% Ne, 9.5% CO_2 and 4.8% N_2. Charged particles that travel through the TPC ionize this gas along their way. Throughout the drift regions a highly uniform electrostatic field (up to 400 V/cm) guarantees that the released electrons are transported in z-direction towards the readout end-plates. At the end-plates, 557 568 pads read out the electric signal, which is used to determine the particle trajectory. As the charged particles are deflected by the surrounding magnetic field, the knowledge of the particle trajectory allows directly the determination of the rigidity p/z of the particle. Here p is the momentum and z the charge

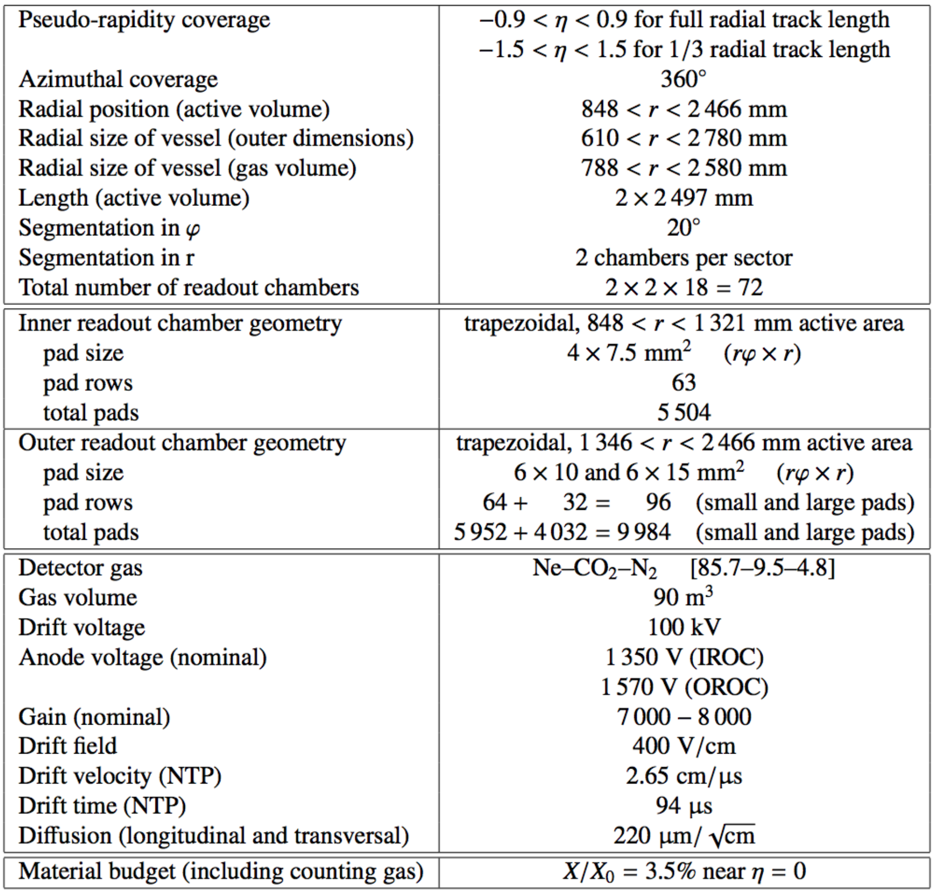

Pseudo-rapidity coverage	$-0.9 < \eta < 0.9$ for full radial track length $-1.5 < \eta < 1.5$ for 1/3 radial track length
Azimuthal coverage	360°
Radial position (active volume)	$848 < r < 2\,466$ mm
Radial size of vessel (outer dimensions)	$610 < r < 2\,780$ mm
Radial size of vessel (gas volume)	$788 < r < 2\,580$ mm
Length (active volume)	$2 \times 2\,497$ mm
Segmentation in φ	20°
Segmentation in r	2 chambers per sector
Total number of readout chambers	$2 \times 2 \times 18 = 72$
Inner readout chamber geometry	trapezoidal, $848 < r < 1\,321$ mm active area
pad size	4×7.5 mm^2 $(r\varphi \times r)$
pad rows	63
total pads	5 504
Outer readout chamber geometry	trapezoidal, $1\,346 < r < 2\,466$ mm active area
pad size	6×10 and 6×15 mm^2 $(r\varphi \times r)$
pad rows	$64 + 32 = 96$ (small and large pads)
total pads	$5\,952 + 4\,032 = 9\,984$ (small and large pads)
Detector gas	Ne–CO$_2$–N$_2$ [85.7–9.5–4.8]
Gas volume	90 m^3
Drift voltage	100 kV
Anode voltage (nominal)	1 350 V (IROC) 1 570 V (OROC)
Gain (nominal)	7 000 – 8 000
Drift field	400 V/cm
Drift velocity (NTP)	2.65 cm/µs
Drift time (NTP)	94 µs
Diffusion (longitudinal and transversal)	$220\ \mu\mathrm{m}/\sqrt{\mathrm{cm}}$
Material budget (including counting gas)	$X/X_0 = 3.5\%$ near $\eta = 0$

Table 2.1: General parameters of the ALICE TPC taken from [48].

number of the particle. In addition, the TPC is used for particle identification via the specific energy loss $\mathrm{d}E/\mathrm{d}x$, which is described in detail in section 3.1.

TOF

The **T**ime-**O**f-**F**light detector [49] has, like the ITS and the TPC, a cylindrical shape. Following the TPC segmentation the detector is as well divided into 18 sections of 20° in ϕ. The detector consists of 1638 **M**ultigap **R**esistive **P**late **C**hambers (MRPC strips), which are organized in 5 modules per section. At intermediate p_{T} (around 1 GeV/c) the time resolution in Pb–Pb collisions is 80 ps for pions [47]. The TOF detector allows for the identification of pions and kaons up to 2.5 Gev/c and for protons up to 4 GeV/c [47]. Further, the measured velocity β_{TOF} can be used to calculate the m^2/z^2 for each particle (m is the mass of the particle, z is the charge number of the particle), which allows for example to distinguish between ^{3}He and ^{4}He at higher momenta, where the TPC alone can not be used anymore (for details see also section 3.2). For the TOF measurements a starting time is required, which is provided by the T0 detector (described next).

T0 and VZERO

The T0 and VZERO detector [51] consist of two sub-detectors each, which are placed on opposite sides of the interaction point on the left and right side of the ITS. The two T0 detectors (T0C and T0A) are arrays of Cherenkov radiators, which are located at pseudorapidity intervals of $-3.28 \leq \eta \leq -2.97$ and $4.61 \leq \eta \leq 4.92$. The T0 provides fast timing signals with a time resolution of 20-25 ps in Pb–Pb collisions. Besides the above mentioned starting time for the TOF measurements, these timing signals can be used as L0 trigger and as wake-up calls for the TRD. The two VZERO detectors (VZERO-A and the

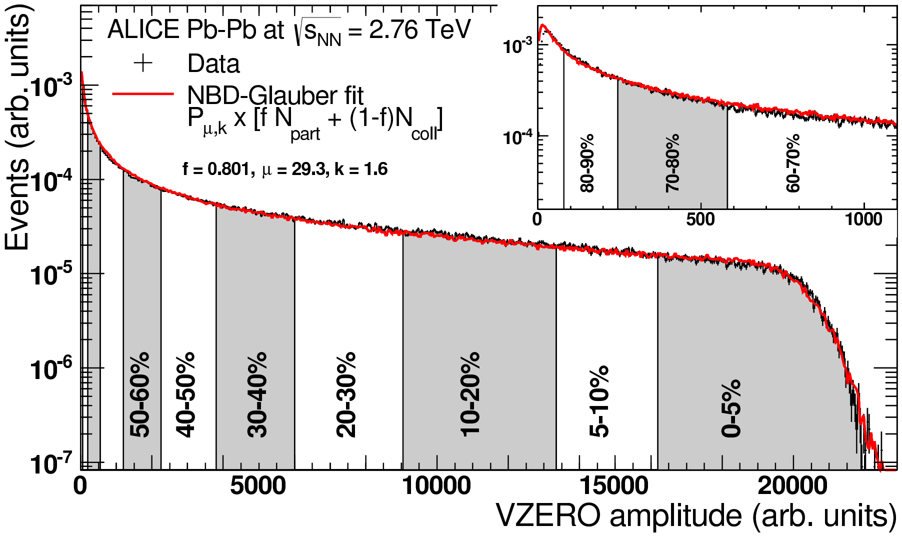

Figure 2.3: Sum of the amplitudes measured with the VZERO detector. The different centrality classes are indicated. The plot is taken from [50], where also the fit function and the procedure is described in more detail.

VZERO-C) are placed at pseudorapidity intervals of $-3.7 \leq \eta \leq -1.7$ and $2.8 \leq \eta \leq 5.1$. Each VZERO detector is a ring of plastic scintillators. Due to the good time resolution, better than 1 ns, the VZERO is used to distinguish between beam-beam collisions and background (beam-gas) events.

In addition, the sum of the measured amplitudes from each scintillator allows for the determination of the centrality of a Pb–Pb event. The centrality is related to the impact parameter of a collision, which can not be measured directly. The impact parameter b is the offset of the two colliding nuclei. This means that for $b = 0$ the nuclei collide exactly at their centers ("head on") and the centrality is 0%. The impact parameter is also related to the number of nucleons (N_{part}) that have taken part in the collision (participants). The nucleons which have not participated in the collision are called spectators. The energy deposit measured in the VZERO is higher for central collisions than for peripheral collisions, as in this case more nucleons have participated in the collision. Therefore, also the measured sum of the amplitudes from the scintillators is higher. This relation between the measured amplitude in the VZERO detector and number of participant nucleons is used to determine the centrality. The resulting distribution is shown in Figure 2.3. The centralities are divided into several centrality classes, which are also shown. The red curve is a Glauber model fit, which can be used to describe the relation between b and N_{part}. In this model the nuclear density function, which determines the position of the nucleons inside the nucleus, is modeled by a modified Woods-Saxon potential. The collisions themselves are treated as a sequence of independent binary nucleon-nucleon collisions N_{coll}. In this procedure the particles are produced from a number of sources. These sources generate particles based on a Negative Binomial Distribution, which has the mean multiplicity per collision μ as a parameter as well as an additional parameter κ which controls the tail towards higher multiplicities. The number of these particle-producing sources is given by $f \times N_{\text{part}} + (1 - f) \times N_{\text{coll}}$, where f is the relative contribution between N_{part} and N_{coll}. More details on the implementation of the Glauber model in ALICE and the determination of the centrality can be found in [50].

3 Particle Identification

For the analyses presented in this thesis several different **P**article **Id**entification (PID) methods are used. This includes the PID via the TPC specific energy loss $\mathrm{d}E/\mathrm{d}x$ and via TOF m^2/z^2 distributions for stable particles as well as topological identification and the identification in invariant mass distributions for unstable particles. These methods are explained in this chapter.

3.1 Specific energy loss

The PID via the specific energy loss $\mathrm{d}E/\mathrm{d}x$ measurement is based on the principle that charged particles that traverse a material (for example the gas in the TPC) interact with the electrons of the atoms. Thus the atoms are ionized[1] and the traveling particle loses energy. The energy loss $\mathrm{d}E$ of the crossing charged particle per traveled distance $\mathrm{d}x$ is described by the Bethe-Bloch formula. In 1930 Hans Bethe first derived the non-relativistic version [52], which he extended in 1932 to the relativistic formula [53]

$$-\frac{dE}{dx} = Kz^2\frac{Z}{A}\frac{1}{\beta^2}\left[\frac{1}{2}\ln\left(\frac{2m_e c^2\beta^2\gamma^2 T_{max}}{I^2}\right) - \beta^2 - \frac{\delta(\beta\gamma)}{2}\right], \tag{3.1}$$

with the following variables:

- $\beta = \frac{v}{c}$
- $\gamma = \frac{1}{\sqrt{1-\left(\frac{v}{c}\right)^2}}$
- velocity v
- speed of light c
- charge number of the projectile particle z
- elementary charge e
- rest mass of the electron m_e
- atomic number of absorber Z
- atomic mass of absorber A
- mean excitation energy I
- maximum kinetic energy which can be passed to a free electron in a single collision T_{max}
- constant $K = 4\pi N_A r_e^2 m_e c^2$
- Avogadro's number N_A
- classical electron radius r_e
- density effect correction to ionization energy loss $\delta(\beta\gamma)$

---

[1] The atoms can also be excited.

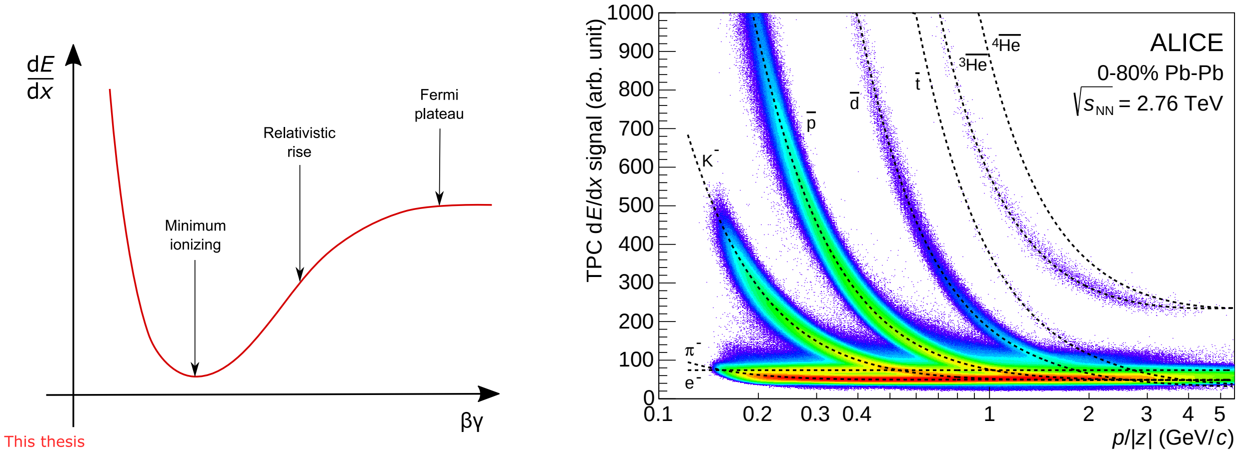

This thesis

Figure 3.1: Right side: Shape of the specific energy loss as function of $\beta\gamma$. Left side: Measured TPC energy-loss signal versus rigidity for negative particles. In addition the Bethe-Bloch parametrization for the different particle species is shown as black dotted lines [55].

The Bethe-Bloch formula is only valid in the region $0.1 < \beta\gamma < 1000$. For $\beta\gamma < 0.1$ the velocity of the traversing particle becomes comparable to the velocity of the atomic electrons. At higher $\beta\gamma$ radiative effects are important. The general shape of the specific energy loss as function of $\beta\gamma$, in the range where the Bethe-Bloch formula is valid, is shown on the left side in Figure 3.1. For increasing $\beta\gamma$ the energy loss becomes smaller until the minimum is reached. The particles with the $\beta\gamma$ at the minimum are called "minimum-ionizing particles" or MIP's. Then the energy loss increases again ("relativistic rise") until it finally saturates on a constant value ("Fermi plateau"). As $\beta\gamma = p/Mc$ (p = momentum M = mass of the crossing particle) the energy loss is different for different particle species and can therefore be used for the PID of charged particles.

In order to have a convenient way to deal with the formula in experiments the ALEPH collaboration proposed a parameterized Bethe-Bloch formula [54], which is given by

$$f(\beta\gamma) = \frac{P_1}{\beta^{P_4}} \cdot \left[P_2 - \beta^{P_4} - \ln\left(P_3 + \frac{1}{(\beta\gamma)^{P_5}} \right) \right], \tag{3.2}$$

where $P_{1\ldots5}$ are free parameters, which depend on the crossed material (for example the gas in the TPC or the silicon in ITS). This parametrization is also used in ALICE. For negatively charged particles the measured $\mathrm{d}E/\mathrm{d}x$ in the TPC is shown as function of the rigidity ($p/\mid z\mid$) together with the parametrization for different particles species on the right side in Figure 3.1.

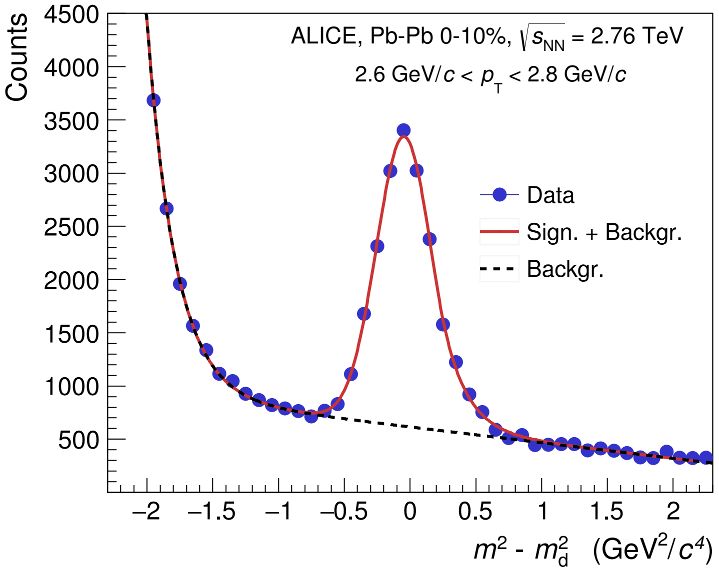

Figure 3.2: Example of a mass distribution obtained combining the TOF and TPC detector [9].

3.2 Time-Of-Flight - m^2/z^2 distribution

The determination of the m^2/z^2 distribution (m = mass of the particle, z charge number of the particle) can also be used for PID. The value of m^2/z^2 for each particle is not measured directly, but can be determined from the measured rigidity $p\ z$, the length l of the reconstructed particle track inside the detectors and the flight time t, which is measured with the TOF detector. If these three quantities are known, the m^2/z^2 can be calculated as follows:

$$\frac{m^2}{z^2} = \frac{p^2}{z^2 c \sqrt{\gamma^2 - 1}} \tag{3.3}$$

where $\gamma = \frac{1}{\sqrt{1-\beta^2}}$ and $\beta = \frac{l}{c \cdot t}$.
An example of the resulting distribution of deuterons measured in Pb-Pb collisions is shown in Figure 3.2. As deuterons have a $z = 1$, m^2/z^2 is reduced to m^2 in this case. In addition, it is often good to subtract the deuteron mass m_d^2 from the measured m^2. Therefore the deuterons show up as a peak around zero. Within this thesis this method is used for the identification of alpha and anti-alpha particles, as discussed in chapter 5.

3.3 Invariant mass distribution

The identification using an invariant mass distribution is used in case of unstable particles, where the mother particles can not be measured directly. Instead, only the daughter particles are measured and the mass of the mother is calculated with the four-momentum-vectors $\left(p = \left(E, \overrightarrow{p}\right)\right)$ of the daughters. In case of a two-body decay the invariant mass is given by

$$m_{\text{mother}} = \sqrt{\left(E_1 + E_2\right)^2 - \left(\overrightarrow{p_1} + \overrightarrow{p_2}\right)^2 / c^2}. \tag{3.4}$$

This can be transformed by using the relation

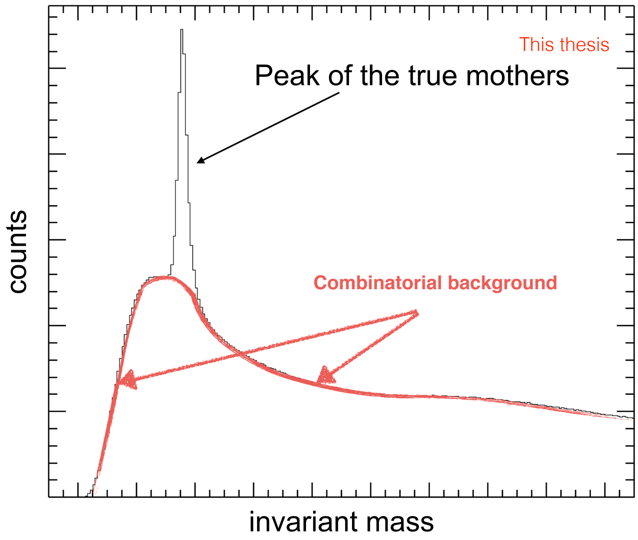

Figure 3.3: Illustration of an invariant mass distribution.

$$E^2 = \vec{p}^{\,2} \cdot c^2 + m^2 \cdot c^4 \tag{3.5}$$

into the finally used equation:

$$m_{mother} = \sqrt{{m_1}^2 + {m_2}^2 + 2\sqrt{\left(\vec{p_1}^{\,2}/c^2 + {m_1}^2\right) \cdot \left(\vec{p_2}^{\,2}/c^2 + {m_2}^2\right)} - 2\vec{p_1}\vec{p_2}/c^2}\,. \tag{3.6}$$

The invariant mass is determined for all possible particle combinations. If the combined particles correspond to a decay of the same mother, their invariant mass is equal to the true mass of the mother [2]. In the other case, if the combined particles do not correspond to a decay of the same mother, they share energy and momentum statistically. Therefore, this method does not allow the identification of a single mother particle, but a certain amount of statistics is needed to identify the signal of the mother particles in an invariant mass distribution. An illustration of such a distribution is shown in Figure 3.3. At the invariant mass of the true mother a peak is formed in the spectrum, whereas the rest contributes to the combinatorial background. This background can be reduced for example with topological restrictions on the determined properties of possible mothers and daughters (see 3.4). Within this thesis the invariant mass technique is used for the search of two exotic bound states, the $\overline{\Lambda \mathrm{n}}$ and $\Lambda\Lambda$ bound states, see chapter 4.

3.4 Topological identification

To reduce the combinatorial background in an invariant mass distribution (see section 3.3) topological properties can be used and thus allowing for a cleaner identification. Figure 3.4 illustrates a two-body decay of a neutral mother and shows the different criteria which can be used. Such a decay is also called a V^0 decay, as the shape, which is visible inside a detector if the daughter particles experience a magnetic field, resembles the letter V. As the mother particle does not carry an electrical charge, it will

---

[2] The measured invariant mass in experiments is not at the exact value of the mass of the mother, but due to the finite resolution of the detector the value is "smeared". Therefore the detected invariant mass has a width, which corresponds to the detector resolution.

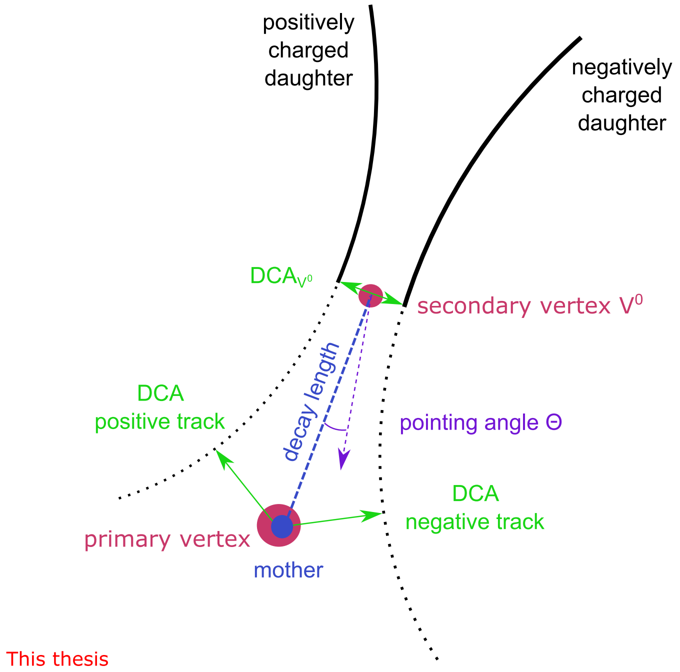

Figure 3.4: Illustration of a V^0 decay.

not leave any trace (track) inside the detector. The tracks of the two opposite charged daughters on the other hand form the two legs of the V. As the daughters are created at the decay point (secondary vertex), two oppositely charged particles, which do not originate from the primary vertex, are combined. To ensure that a track does not come from the primary vertex the ***D**istance-of-**C**losest **A**pproach (DCA)* between a track and the primary vertex can be used. The *DCA* in the plane perpendicular to the beam axis is called DCA_{xy}, whereas the *DCA* in the beam direction is called DCA_z. In order to select secondary particles, these *DCAs* should not be smaller than a certain value, which depends on the particles involved and in particular on the lifetime of the mother, but typically is in order of a few cm. The exact value of choice can be evaluated with a Monte-Carlo simulation. On the contrary, the DCA_{V^0}, which is the *DCA* between the two daughter tracks should be smaller as the two tracks are originating from the same mother. Therefore, this is the second criterion which can be used. The (online) V^0 finder algorithm in ALICE for example restricts the DCA_{V^0} to be smaller than 1 cm. Additional properties, which can be used are related to the mother, which has to be created at the interaction point. If the mother is a primary particle, it can be determined with the use of the *pointing angle* Θ, which is the angle between the reconstructed flight-line and reconstructed momentum vector of the mother particle. In practice the *cosine of the pointing angle* is used instead of the angle itself. If the value of the cos(Θ) is close to 1, the angle Θ is small and the probability that the mother was created in a collision is large. Finally, also for the decay length, minimum and maximum values can be set. Within this thesis the different topological properties and the invariant mass determination are used for the search of two weakly decaying bound states (as shown in the next chapter 4).

4 Search for weakly decaying $\overline{\Lambda \mathrm{n}}$ and $\Lambda\Lambda$ bound states

The lightest naturally occurring bound state is the deuteron, which is a bound state of a proton and a neutron. This raises the interesting question whether or not bound states with any of the heavier baryons and a nucleon can exist. The lightest of such hypothetical bound states would be a bound state of a Λ particle and a nucleon. The theoretical description of the deuteron is already very challenging, as the calculation of the binding energy requires a precision of at least 10^{-3}. Therefore, experimental evidence for the existence or exclusion of such bound states is of great importance. The ALICE detector is very well suited for such an investigation. Its excellent PID capabilities and the firm control of the systematic uncertainties have already been demonstrated in the measurement of deuterons and ^{3}He [9]. Furthermore, even the production of ^{4}He has been measured for the first time within this thesis, see chapter 5.

This chapter presents the search for two such hypothetical weakly decaying bound states, which is also published in [55]. The first one is a possible bound state of an $\overline{\Lambda}$ and an $\overline{\mathrm{n}}$ (see section 4.1). The second one is the H-dibaryon ($\Lambda\Lambda$) (see section 4.2). Both searches are performed by analyzing $19.3 \cdot 10^6$ events in a centrality range of 0-10% from the data set of Pb–Pb collisions at $\sqrt{s_{\mathrm{NN}}} = 2.76$ TeV from 2011. The centrality selection is done using the VZERO detector (see chapter 2) and only events for which the primary vertex falls within $\mid V_z \mid < 10$ cm are accepted.

Improving the current knowledge of such light bound states constitutes a valuable contribution to the physics of hadrons. Yet, as shown below, there are strong indications that the investigated states do not exist.

4.1 $\overline{\Lambda \mathrm{n}}$ bound state

The analysis strategy for the $\overline{\Lambda \mathrm{n}}$ bound state assumes a V0 decay topology (see section 3.4), in particular a strange decay with a lifetime of typically a few cm. For this type of decay a specialized algorithm is implemented in the analysis framework (V0 finder) [47]. As sketched in the schematic picture of the decay in Figure 4.1, the search for the $\overline{\Lambda \mathrm{n}}$ bound state is performed in the decay channel $\overline{\Lambda \mathrm{n}} \rightarrow \overline{\mathrm{d}} + \pi^+$. The search is done on the anti-particle, because of the reduced secondary contamination from knock-out processes in the detector material compared to the particle side. This is demonstrated in Figure 4.2, which shows the number of (anti-)deuterons as a function of the ***D****istance-of-****C****losest* ***A****pproach (DCA)*[1] in the plane perpendicular to the beam axis (DCA_{xy}). The nominal interaction point is located at $DCA_{xy} = 0$, whereas for increasing values of $|DCA_{xy}|$ the distance to the interaction point grows in transversal direction. The peak at 0 therefore indicates that all of the (anti-)particles are produced during the collision. The width of the peaks reflects the resolution, whereas the very small plateau is a result of multiple scattering. The amount of produced particles and anti-particles should in principle be the same at LHC energies, which is a big advantage compared to lower energy experiments. There are also background particles produced from knock-out processes in the detector material, which are visible in the right and left plateaus extending towards larger values of the DCA_{xy}. The total number of deuterons increases, if the DCA_z (along the beam axis) is increased from 1 cm (black distribution) to 20 cm (red distribution), see left panel of Figure 4.2. These additional deuterons are stemming from knock-out processes in the

---

[1] Between the track of a particle and the primary vertex

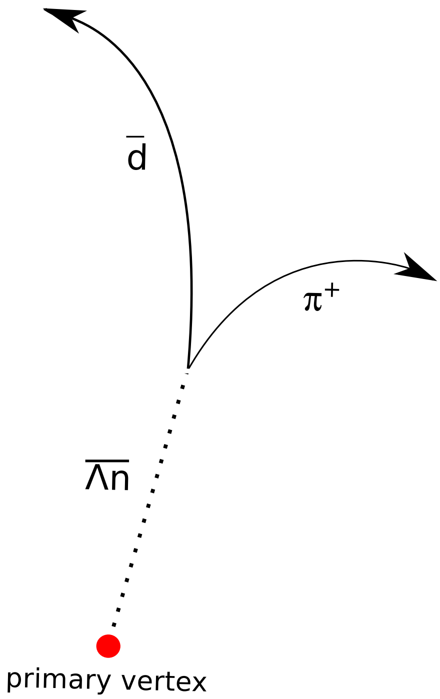

Figure 4.1: Decay topology of the $\overline{\Lambda n}$ bound state [56].

detector material. This increase is clearly not visible for anti-deuterons, see right panel of Figure 4.2. Since for the reconstruction of a Λn bound state a secondary deuteron is needed, the secondary contamination from knock-out processes in the detector material produces a substantial background. In order to avoid this complication, only the anti-particle side is investigated. Nevertheless the particle side has been analysed as a cross-check as well and it was found to be indeed less sensitive than the anti-particle side.

The track cuts applied to the daughter tracks, as well as the topological selections on the V0 and the kinematic cuts, which were used in the analysis are summarized in Table 4.1. The anti-deuterons and pions are selected in a 3σ band around their specific energy loss $\mathrm{d}E/\mathrm{d}x$ in the TPC as described in section 3.1. The cuts on the *cosine of pointing angle* ($\cos(\Theta)$) and the *DCA*[2] between the V0 daughters were chosen after a careful Monte-Carlo study. For this study around 4×10^4 HIJING events enhanced with (anti-)Λn bound state, (anti-)H-dibaryon and (anti-)Hypertriton (in its two and three body decay) were simulated. For each species 5 to 10 particles and anti-particles have been added on top of a minimum bias Monte-Carlo event. They have been injected flat in p_T from 0 to 10 GeV/c and flat in rapidity from -1 to 1. In addition, several Monte-Carlo productions with a number of different assumed lifetimes have been used to study the influence of the lifetime on the efficiency (see section 4.1.3).

The left panel of Figure 4.3 shows the $\cos(\Theta)$ distribution for correctly associated $\overline{\Lambda n}$ bound states in Monte-Carlo in black. The red points indicate which percentage of the correctly associated $\overline{\Lambda n}$ bound states have a $\cos(\Theta)$ with this value up to this bin. The right panel of Figure 4.3 shows the same for the background, which includes all $\overline{\Lambda n}$ bound state candidates found in Monte-Carlo, which could not be correctly associated to a generated $\overline{\Lambda n}$ bound state. A cut of $\cos(\Theta) > 0.999$ was chosen, because it only cuts away 5% of the signal, but 80% of the background. The same study was done for the *DCA* between

---

[2] Between to tracks

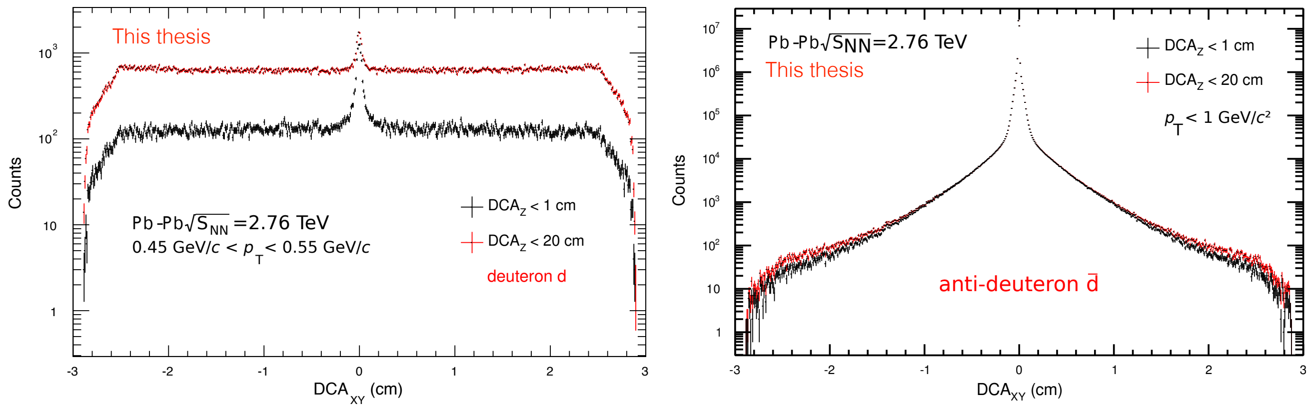

Figure 4.2: Number of deuterons (left) and anti-deuterons (right) as a function of DCA_{xy}, shown for different DCA_z (1 cm in black and 20 cm in red).

cut	**value**
Track cuts	
Kink daughters	rejected
TPC	refit[3]
$\mathrm{n}_{\mathrm{clusters}}$(TPC)	> 70
χ^2/clusters	< 5
Pseudo-rapidity η	$\lvert\eta\rvert < 0.9$
V0 and kinematic cuts	
Cosine of pointing angle	$\cos(\Theta) > 0.999$
DCA between the V0 daughters	$DCA < 0.3$ cm
Momentum p_{tot} of the $\overline{\mathrm{d}}$	$p_{tot} > 0.2$ GeV/c
Energy loss dE/dx $\overline{\mathrm{d}}$	$dE/dx > 110$
PID cut $\overline{\mathrm{d}}$	3σ (TPC)
PID cut π^+	3σ (TPC)
Rapidity of mother	$\lvert y\rvert < 1$

Table 4.1: Cuts for $\overline{\Lambda\mathrm{n}}$ analysis.

the V0 daughters ($\overline{\mathrm{d}}$ and π^+). The two distributions are shown in Figure 4.4. Here the cut was chosen to be $DCA < 0.3$ cm, because this cuts away 34% of the background, but only 13% of the signal. A possible cut on the *decay radius* of the $\overline{\Lambda\mathrm{n}}$ bound states was also investigated. However the decay radius strongly depends on the lifetime, which is unknown. For this reason this cut is not used.

In order to keep the anti-deuteron identification as clean as possible, by avoiding contamination from lighter particles, a lower cut on the energy loss dE/dx was used. This was chosen in such a way that a contamination with lighter particles is as small as possible, but on the other hand not too many anti-deuterons are lost. A cut of dE/dx > 110 (corresponding to a 1.5 GeV/c cut, see Figure 4.5) was chosen. The remaining contamination can be determined via fits to the TPC signal of the different particle species in the rigidity region between 1.2 GeV/c and 1.5 GeV/c. Generalized Gaussians[4] are used as fit functions. All functions are fitted simultaneously and the contamination of each species is determined by the ratio

---

[3] Details on the tracking can be found in [47].

[4] Gauss multiplied with its error function.

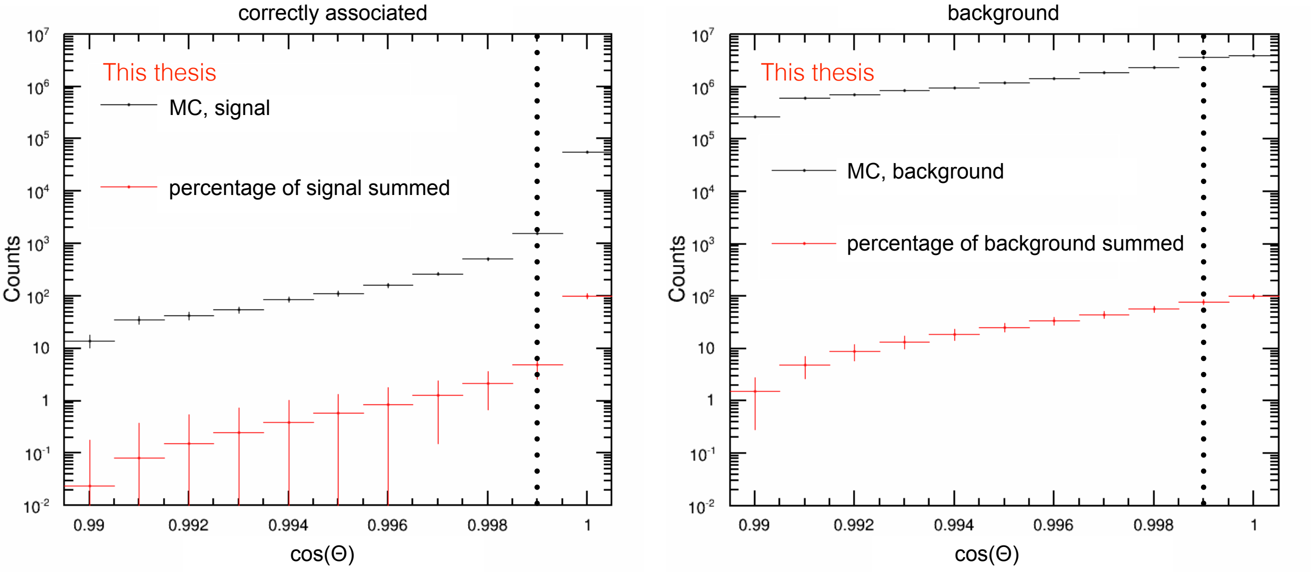

Figure 4.3: *Cosine of pointing angle* distribution for the correctly associated (left) and incorrectly associated (right) $\overline{\Lambda}$n bound states in Monte-Carlo. The vertical dotted line indicates the used cut.

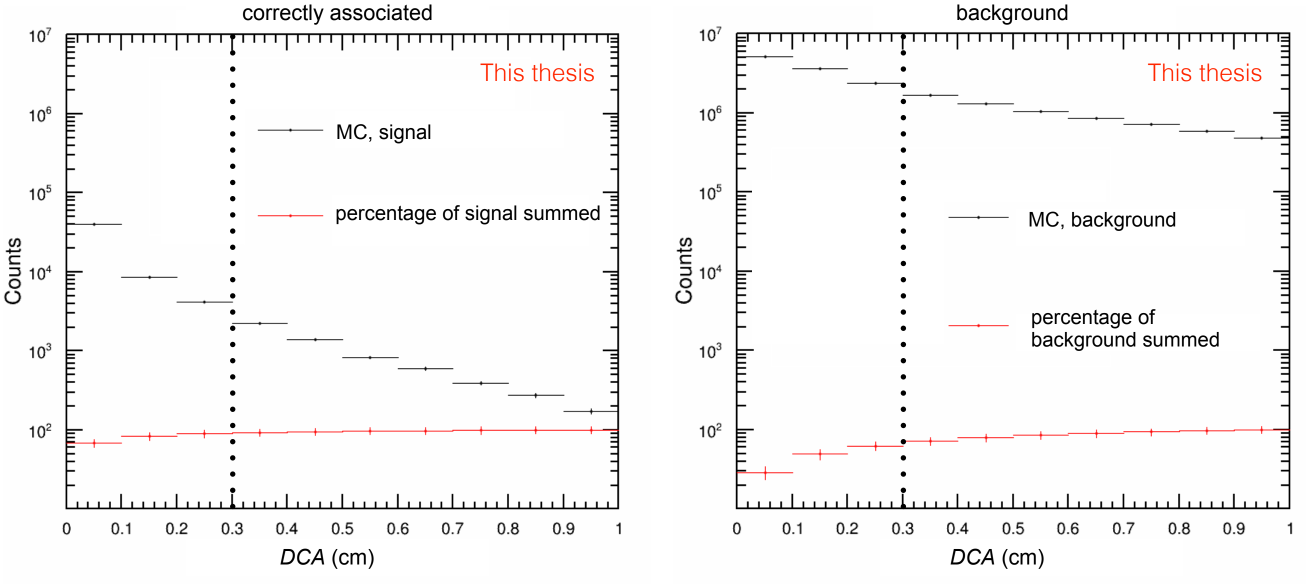

Figure 4.4: Distribution of the *DCA* between the V0 daughters for the correctly associated (left) and incorrectly associated (right) $\overline{\Lambda}$n bound states in Monte-Carlo. The vertical dotted line indicates the used cut.

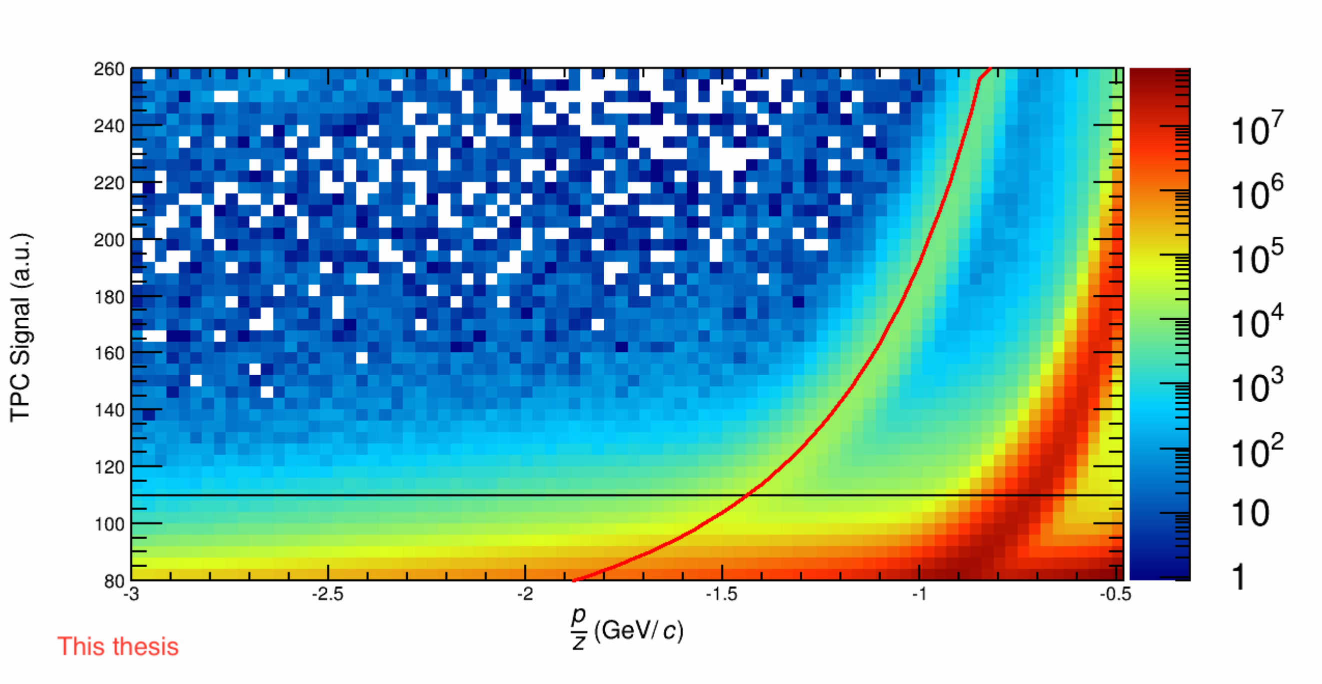

Figure 4.5: The TPC signal versus the rigidity for LHC11h data for negative particles. In addition, the Bethe-Bloch parametrization for anti-deuterons is shown in red, whereas the black line indicates the cut at a TPC signal of 110.

of the integral of the fit function of this particle above $\mathrm{d}E/\mathrm{d}x > 110$ divided by the integral of the deuterons above $\mathrm{d}E/\mathrm{d}x > 110$. The contamination is found to be negligible ($< 10^{-6}$).
The invariant mass of all anti-deuteron and π^+ pairs in real data, which fulfill the above described criteria, is determined and shown in Figure 4.6. The possible background sources, which can contribute to the distribution, are discussed in section 4.1.2.

The efficiency was determined by using the above described Monte-Carlo production and is shown in Figure 4.7. Since the efficiency is p_T dependent, it has to be weighted with the shape of the p_T spectrum. To take into account this dependence, a Blast-Wave calculation (see section 1.5) is used, which is shown in Figure 4.8. This calculation uses a Blast-Wave fit to the deuteron and ^{3}He spectra as input [9]. The true efficiency is the integral of the distribution after the convolution of the efficiency with the Blast-Wave calculation (see Figure 4.9). Due to the $\mathrm{d}E/\mathrm{d}x > 110$ cut used to select clean $\bar{\mathrm{d}}$, this distribution has an upper bound at 2 GeV/c, which leads to an overall p_T weighted efficiency of 3%.

From the statistical hadronization model (described in section 1.4) a value for the possible yield per rapidity unit $\mathrm{d}N/\mathrm{d}y$ in central Pb–Pb collisions is predicted, see Figure 1.3. For the $\overline{\Lambda\mathrm{n}}$ bound state this is $\mathrm{d}N/\mathrm{d}y = 4.06 \cdot 10^{-2}$, corresponding to a chemical freeze-out temperature of 156 MeV for 0 - 10% central Pb–Pb events ($N_\mathrm{part} = 350$). The value of 156 MeV is the result from the current best fit, which can also describe the nuclei within 1σ accuracy up to ^{3}He, see Figure 4.10.

In order to determine the number of expected $\overline{\Lambda\mathrm{n}}$ bound states in the analyzed data set using this prediction it is necessary to know the branching ratio as well. It is 0.54 for a binding energy of the Λn bound state around 1.3 MeV (see Figure 4.11). The binding energy is chosen from the first measurement of the HypHI experiment which claims its discovery [22][5]. The expected signal can finally be calculated as the product of the number of events, efficiency, branching ratio, expected yield and rapidity window:

---

[5] Meanwhile, the HypHI collaboration has published their results which show a resonance at 2.06 GeV/c^2 instead of a bound state at 2.054 GeV/c^2 [21].

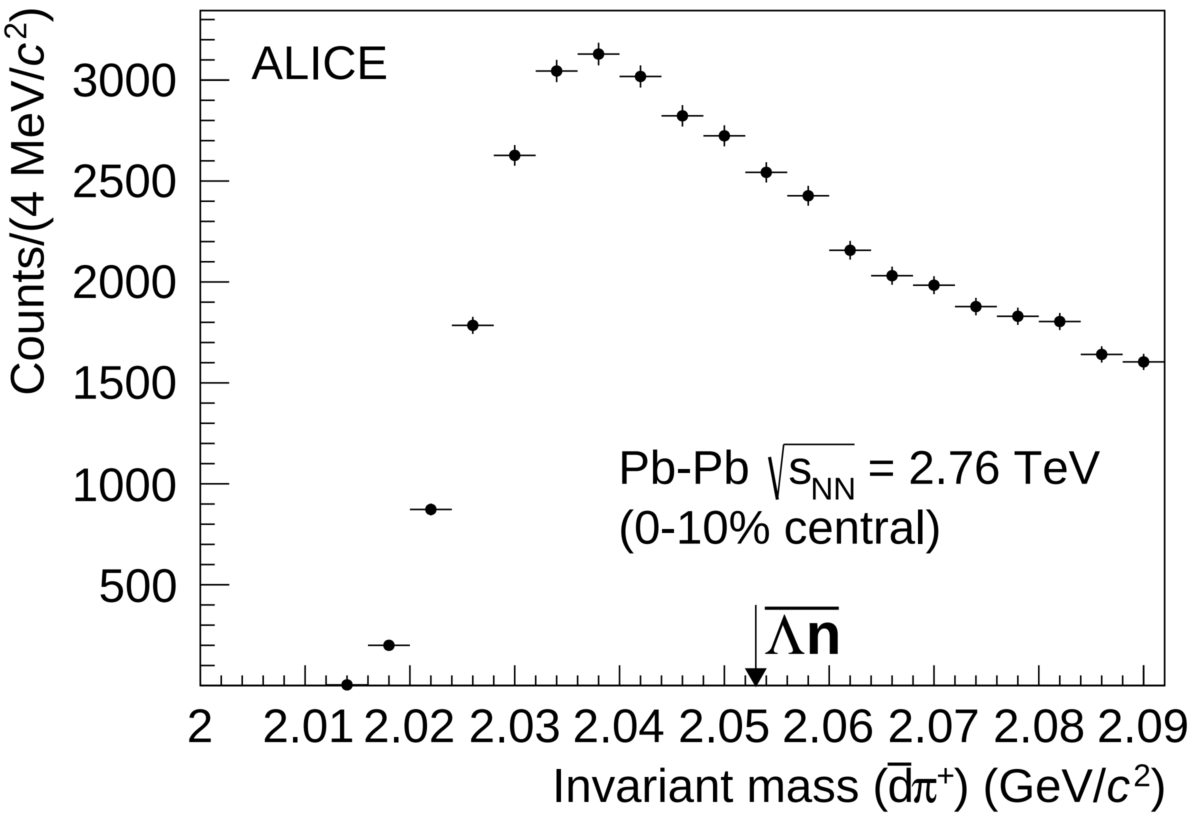

Figure 4.6: Invariant mass of the $\bar{\text{d}}$ and π^+ for $19.3 \cdot 10^6$ central Pb–Pb events [55].

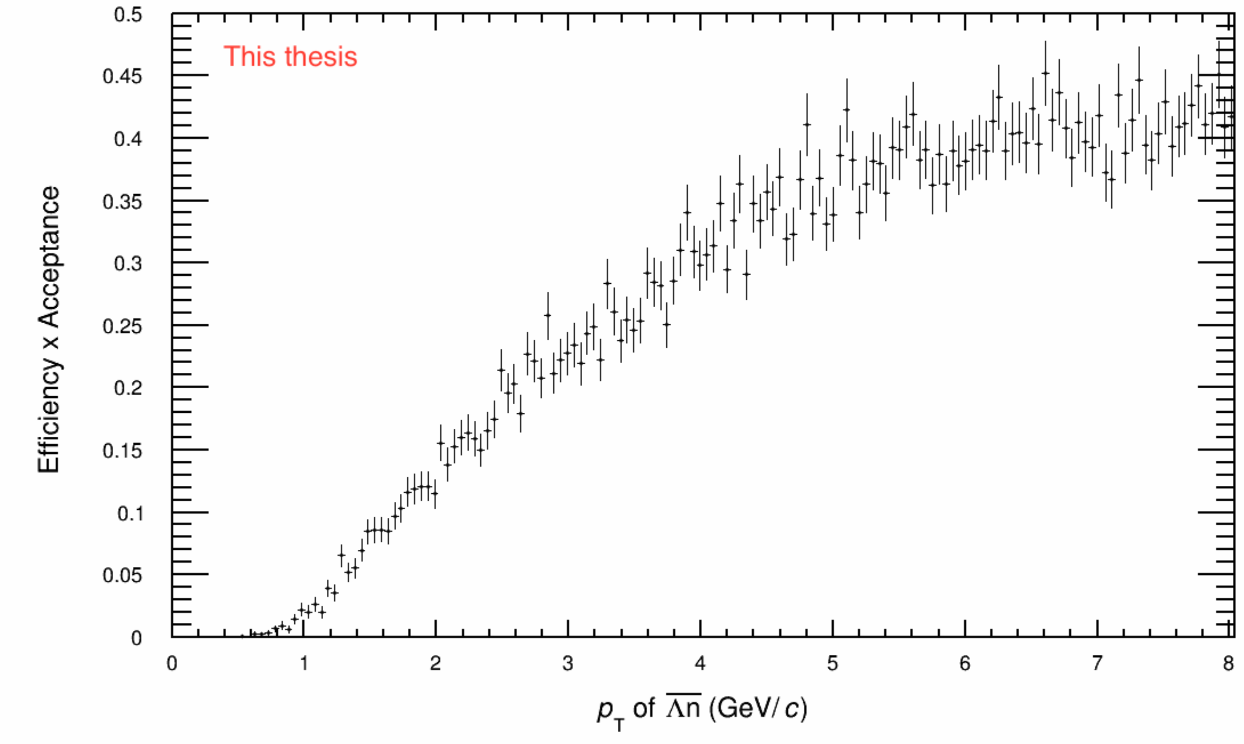

Figure 4.7: Product of acceptance and efficiency for the $\overline{\Lambda\text{n}}$ bound state.

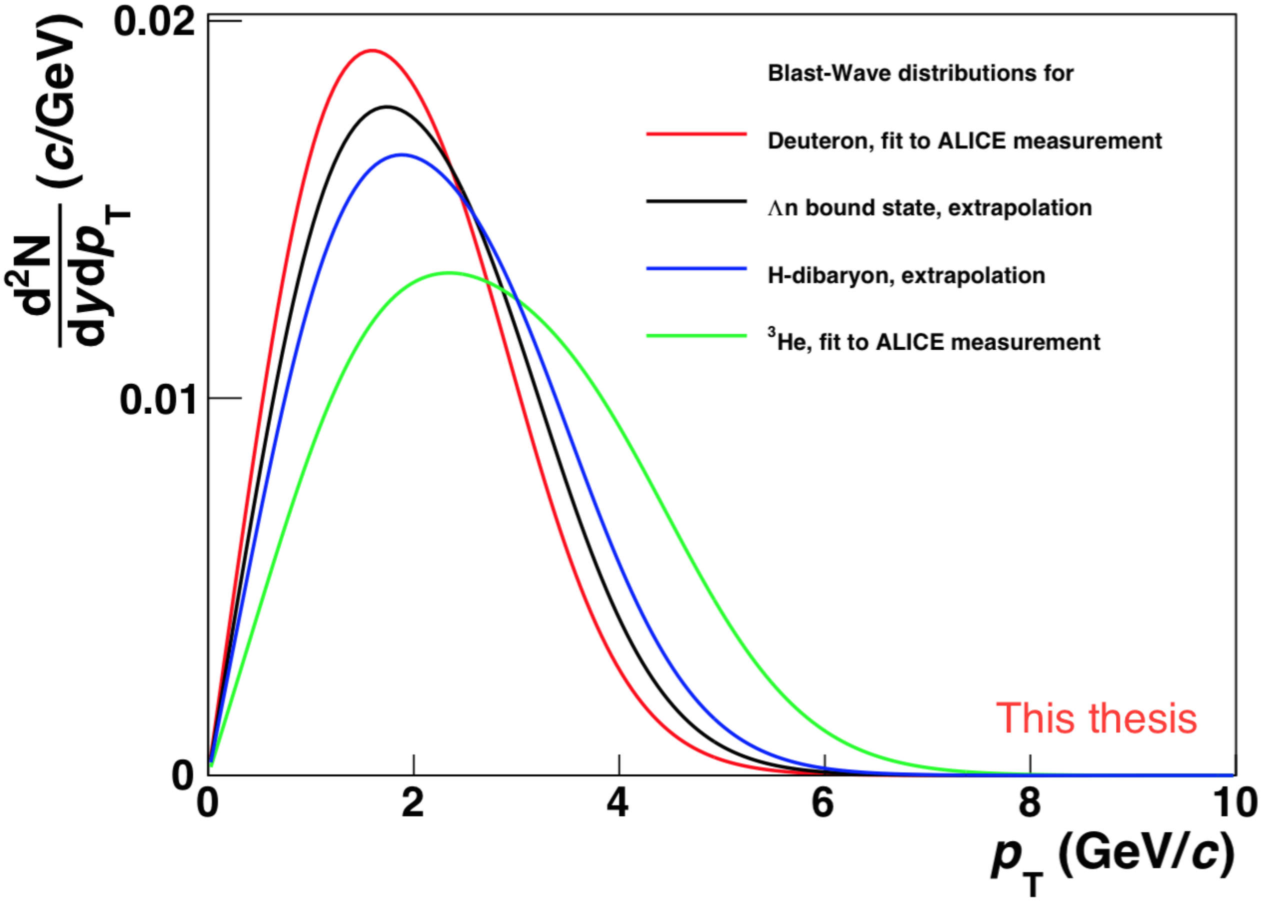

Figure 4.8: Blast-Wave calculation for Λn bound state (black) and H-dibaryon (blue), which is based on the nuclei Blast-Wave fit. The integral is normalized to one. In addition the distributions for deuterons (red) and ^{3}He (green), which were used to study the systematic uncertainty, are shown.

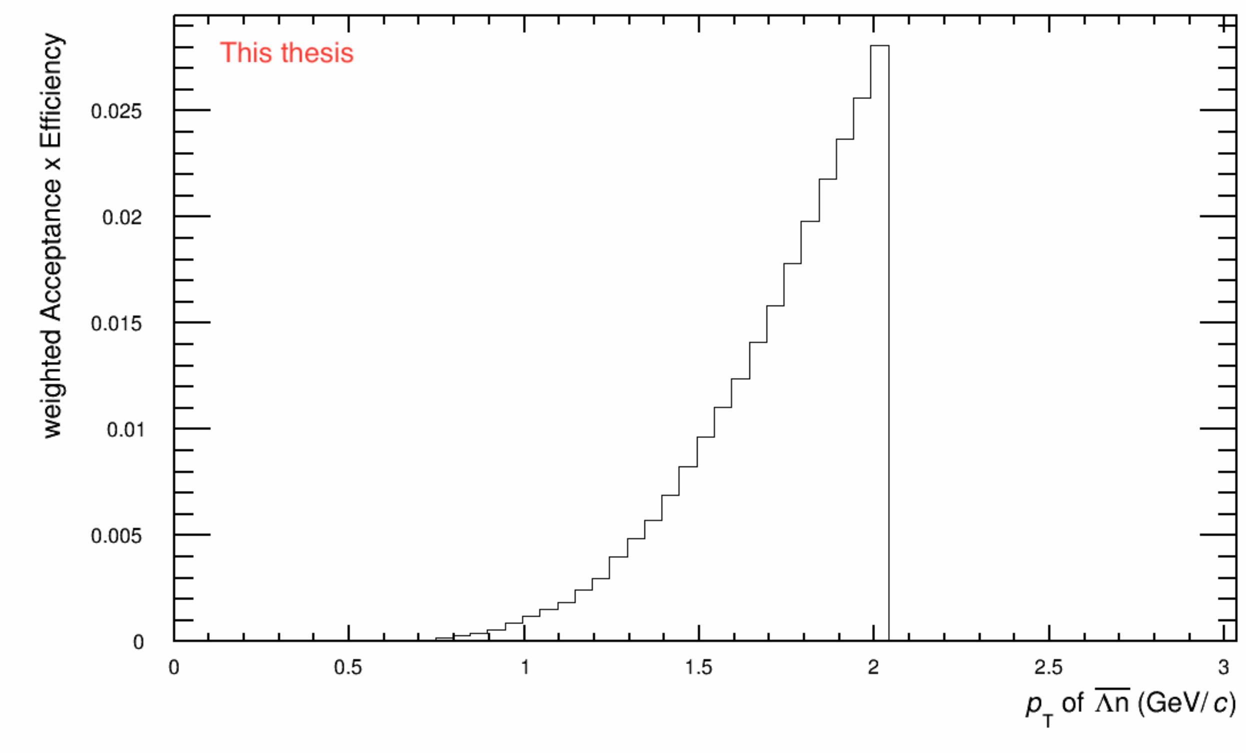

Figure 4.9: Convolution of the Blast-Wave calculation (Figure 4.8) for the $\overline{\Lambda\mathrm{n}}$ bound state with the product of Acceptance and Efficiency (Figure 4.7) extracted from Monte-Carlo.

$$N_{\overline{\Lambda\mathrm{n}},\,\mathrm{rec}} = \underbrace{1.93 \cdot 10^{7}}_{\text{events}} \cdot \underbrace{0.030}_{\text{eff.}} \cdot \underbrace{0.54}_{BR} \cdot \underbrace{0.0406}_{\frac{\mathrm{d}N}{\mathrm{d}y}} \cdot \underbrace{2}_{\mathrm{d}y} \approx 25388\,. \tag{4.1}$$

This prediction suggests, that more than 25k $\overline{\Lambda\mathrm{n}}$ bound states should be visible in the invariant mass distribution in Figure 4.6. Clearly no such signal is observed.

In conclusion, the expected yield is not observed and an upper limit of the production can be set. For the estimation of the upper limit, the ROOT package *TRolke* is used, which also takes into account the uncertainty on the efficiency. The resulting upper limit is 285 (375) at 95% (99%) confidence level for the observed background, which corresponds to a dN/dy of $4.56{\cdot}10^{-4}$ ($6.00{\cdot}10^{-4}$).

4.1.1 Systematic uncertainties

The major source of uncertainty on the obtained upper limit is the influence of the unknown shape of the p_T spectrum. In order to determine this uncertainty, the following consideration is done:
The mass of the $\overline{\Lambda\mathrm{n}}$ bound state should be a few MeV smaller than its constituents Λ and neutron. The mass of the Λ particle is 1115.683 MeV/c^2 [1], whereas the mass of the neutron is 939.565 MeV/c^2 [1]. Therefore the mass of the $\overline{\Lambda\mathrm{n}}$ bound state should be smaller than 2.055 GeV/c^2. Unless the $\overline{\Lambda\mathrm{n}}$ bound state would be bound by more than 179 MeV, which is very unlikely, its mean p_T has to lie in between the mean p_T of the deuteron ($m_d = 1.876$ GeV/c^2) and the one of ^{3}He ($m_{^3\mathrm{He}} = 2.809$ GeV/c^2). The mean p_T of deuteron and ^{3}He is shown together with the mean p_T values of π, kaon and proton in Figure 4.12. According to this consideration the Blast-Wave fit to the deuteron and ^{3}He spectra [9] are used as the extreme cases for the systematic studies. All used Blast-Wave distributions are shown in Figure 4.8. The

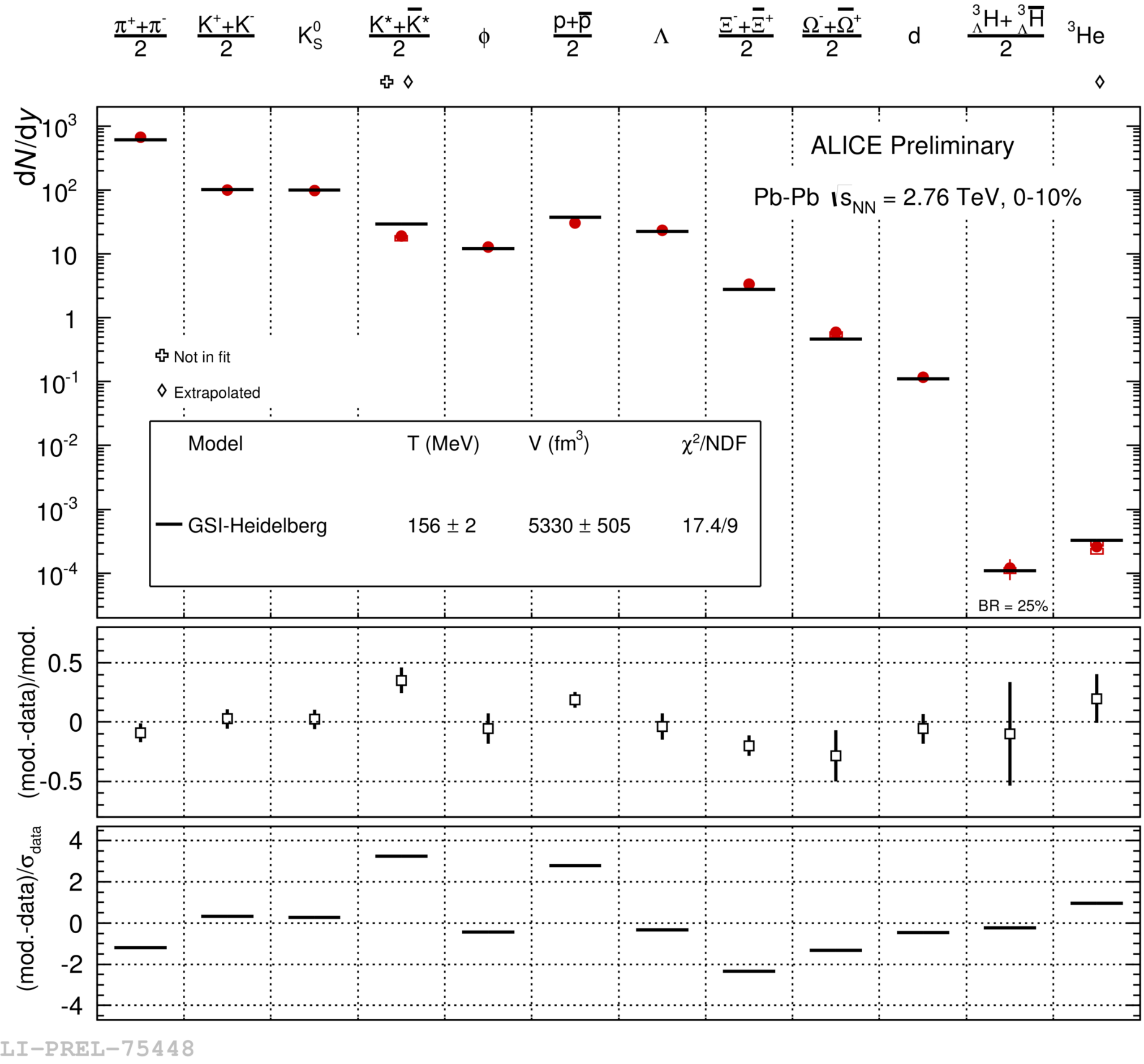

Figure 4.10: dN/dy from the statistical hadronization model (black lines) together with the ALICE measurements (red points) [4].

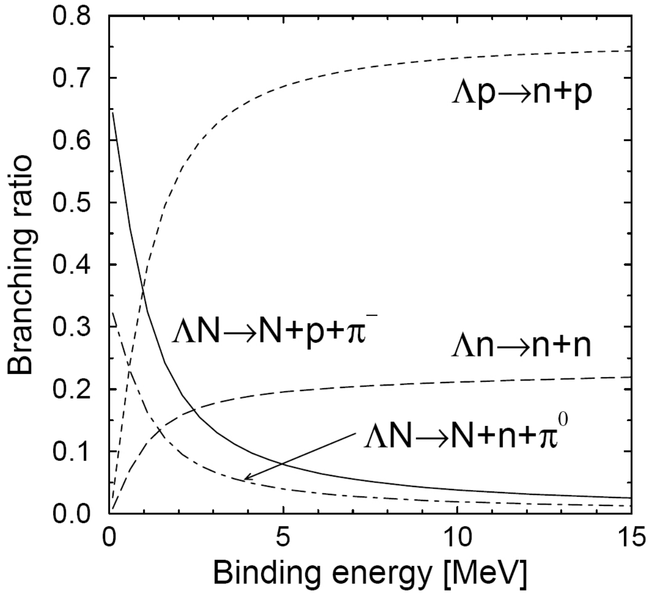

Figure 4.11: Theoretical calculation of the branching ratios of possible Λ-nucleon bound state decay channels [57].

evaluation of the weighted mean leads to a minimum efficiency of 0.021, corresponding to the Blast-Wave fit of the deuterons, and a maximum efficiency of 0.032, corresponding to the Blast-Wave fit of the ^{3}He. To further estimate the uncertainty of the upper limit depending on the efficiency and the measured invariant mass, the track cuts as well as the V0 and kinematic cuts (listed in Table 4.1) are systematically varied for data and Monte-Carlo. This leads to an overall systematic uncertainty of 30.04 % on the upper limit, with the main contribution coming from the unknown p_{T} shape. The contribution of each cut to the total uncertainty is summarized in Table 4.2. For the comparison of the determined upper limit to model predictions (see chapter 6) the upper limit is increased by the estimated systematic uncertainty.

4.1.2 Background study

Possible sources of π^- and $\overline{\mathrm{d}}$, not stemming from real decays of the $\overline{\Lambda\mathrm{n}}$ bound state, to describe the observed shape of the invariant mass distribution (Figure 4.6) are investigated. Therefore a "toy" Monte-Carlo has been produced, which uses the measured Blast-Wave distribution of primary pions and deuterons as input for the p_{T} spectra. For the invariant mass distribution shown in Figure 4.13 primary $\overline{\mathrm{d}}$ are combined with primary π^-. This reproduces the observed broad structure, but with the maximum at a higher mass than in the distribution from real data (Figure 4.6). In a second step the invariant mass was also reconstructed in a Monte-Carlo sample where the $\overline{\Lambda\mathrm{n}}$ bound states and the two-body ($^{3}_{\Lambda}\mathrm{H} \rightarrow ^{3}\mathrm{He} + \pi$) and three-body ($^{3}_{\Lambda}\mathrm{H} \rightarrow \mathrm{d} + \mathrm{p} + \pi$) decay of the hypertriton is injected. The resulting invariant mass distribution, using all secondary deuterons and pions in this sample, is shown in black in Figure 4.14. In red, the invariant mass distribution obtained only for deuterons and pions stemming from the three body decay of the hypertriton is shown, whereas for the blue distribution this decay is excluded. Taking all of this into account, the shape of the invariant mass distribution in real data can be explained by an accumulation of two sources: The first one are primary deuterons, which due to limited resolution were tagged as displaced. This can accidentally happen, if the momentum of the particles is so low that the resolution of the *DCA* of these tracks is not sufficient to distinguish between primary and secondary particles. The second source are deuterons from the three-body decay of the hypertriton. In addition, all possible combinatorial possibilities between these two sources contribute as well. The

cut	value	weighted efficiency	background	upper limit $\times 10^{-4}$	error in %	total error in %	
Track cuts							
$n_{clusters}$(TPC)	> 70	0.030	10550	6.00			
	> 60	0.031	11241	5.99	± 0.12	} ± 0.7	
	> 80	0.028	9423	6.08	± 1.28		
$\chi^2/cluster$	< 5	0.030	10550	6.00			
	< 4	0.029	10272	6.13	± 2.08	} ± 1.12	
	< 6	0.030	10581	6.01	± 0.15		
V0 and kinematic cuts							
Cosine of	> 0.999	0.030	10550	6.00			
pointing angle	> 0.9985	0.030	13915	6.89	± 14.80	} ± 14.74	
($\cos(\Theta)$)	> 0.9995	0.029	7169	5.12	± 14.67		
DCA V0 daughters (cm)	< 0.3	0.030	10550	6.00			
	< 0.4	0.032	12184	6.05	± 0.73	} ± 0.56	
	< 0.2	0.027	8474	5.98	± 0.38		
PID cut anti-deuteron (TPC)	3σ	0.030	10550	6.00			
	2σ	0.028	9371	6.06	± 10.01	} ± 7.32	± 8.57
	4σ	0.030	11550	6.28	± 4.62		
Energy loss dE/dx anti-deuteron	> 110	0.030	10550	6.00			
	> 105	0.030	13049	6.67	± 11.18	} ± 9.83	
	> 115	0.030	8831	5.49	± 8.48		
PID cut π^+ (TPC)	3σ	0.030	10550	6.00			
	2σ	0.027	8692	6.05	± 0.88	} ± 2.55	
	4σ	0.030	11462	6.25	± 4.22		
unknown p_T shape							
Blast-Wave function	$\overline{\Lambda}$n	0.030	10550	6.00			
	d	0.032	10550	5.63	± 6.25	} ± 24.56	
	^{3}He	0.021	10550	8.57	± 42.86		
Sum						**± 30.04**	

Table 4.2: Deviations of the efficiency (Monte-Carlo) and the background (data) after systematical variation of the cuts and the corresponding influence on the upper limit. In green the nominal cuts are listed, whereas the variation limits are highlighted in blue.

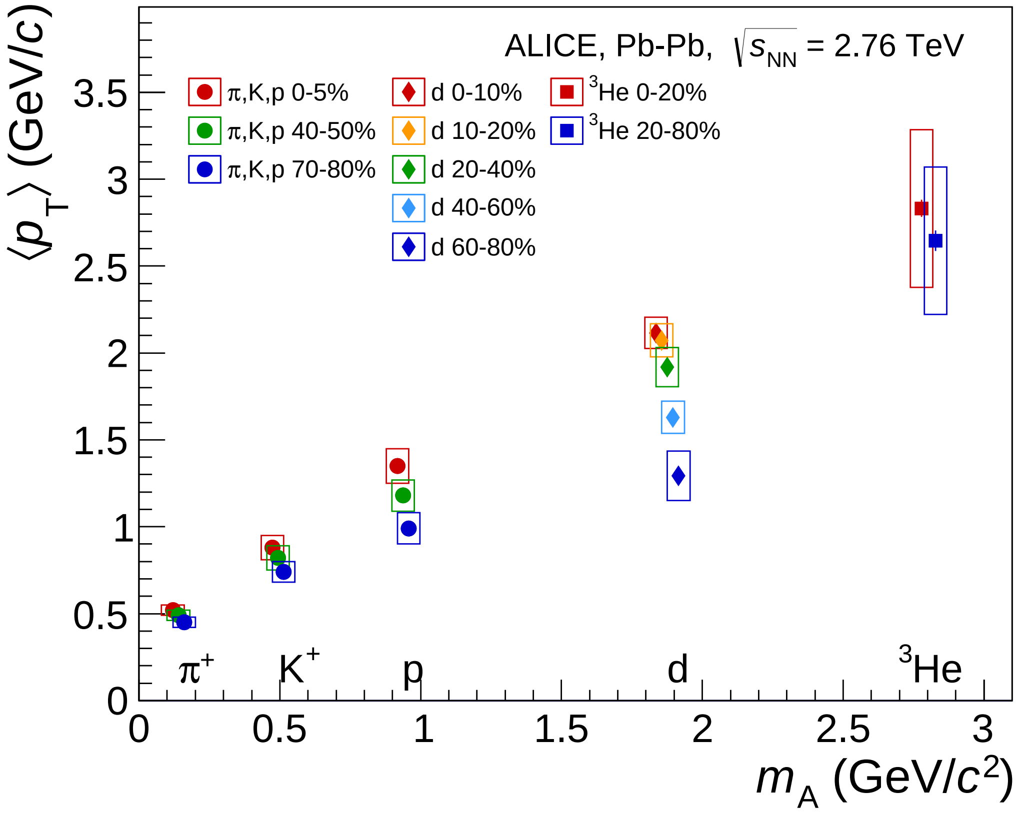

Figure 4.12: Mean p_T vs. mass for different particles and centralities [9].

shape is therefore of purely kinematic origin, with the major contribution from the three-body decay of the hypertriton. It reflects the momentum distributions of the used π^- and $\overline{d}$.

4.1.3 Lifetime studies

The lifetime of the $\overline{\Lambda n}$ bound state is needed as input for the determination of the efficiency based on Monte-Carlo productions. Therefore it influences the calculated upper limit as the efficiency depends strongly on the assumed lifetime. All results presented up to now have used a simulation in which the $\overline{\Lambda n}$ bound state is injected with the lifetime of the free Λ ($2.63 \cdot 10^{-10}$ s). This was chosen, because the lifetime of the hypertriton is of the same order as well. In addition, also the observation by the HypHI experiment is in agreement with this value [22][6]. In order to study the influence of the lifetime on the efficiency, seven different values varying between 0.5 and 38 times the Λ-lifetime are investigated, see Table 4.3. The behavior of the convoluted and integrated efficiency for the different lifetimes is shown in Figure 4.15. Here the cutoff around 2 GeV/c is not applied yet. The efficiencies, with the cutoff included, are shown in black in Figure 4.16. The efficiency increases slightly with larger lifetimes from 0.02 (0.5 ×Λ-lifetime) up to 0.04 (5.3 ×Λ-lifetime). For even longer lifetimes it drops again until it is back to 0.02 (38 ×Λ-lifetime). The upper limit therefore is strongest for the 5.3 ×Λ-lifetime, which is also visible in the black points in Figure 4.17. Table 4.3 summarizes the efficiencies as well as the upper limits for all investigated lifetimes.

---

[6] Meanwhile a resonance with a lifetime of 181 ps has been published [21].

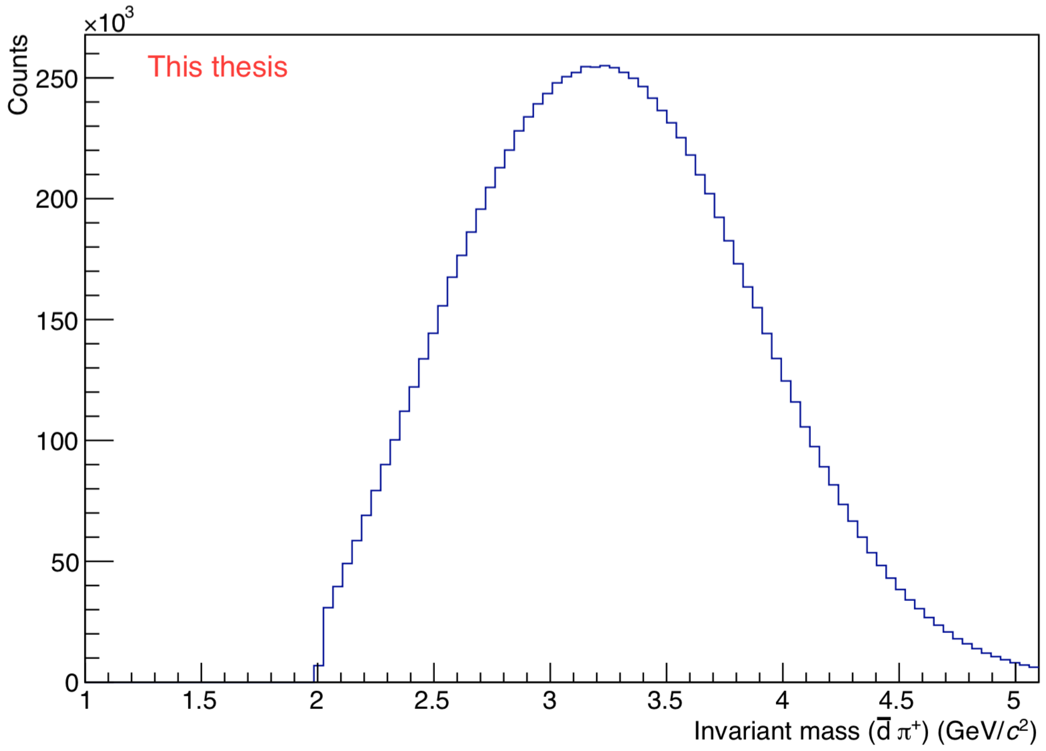

Figure 4.13: Invariant mass distribution in Monte-Carlo of primary deuterons and pions.

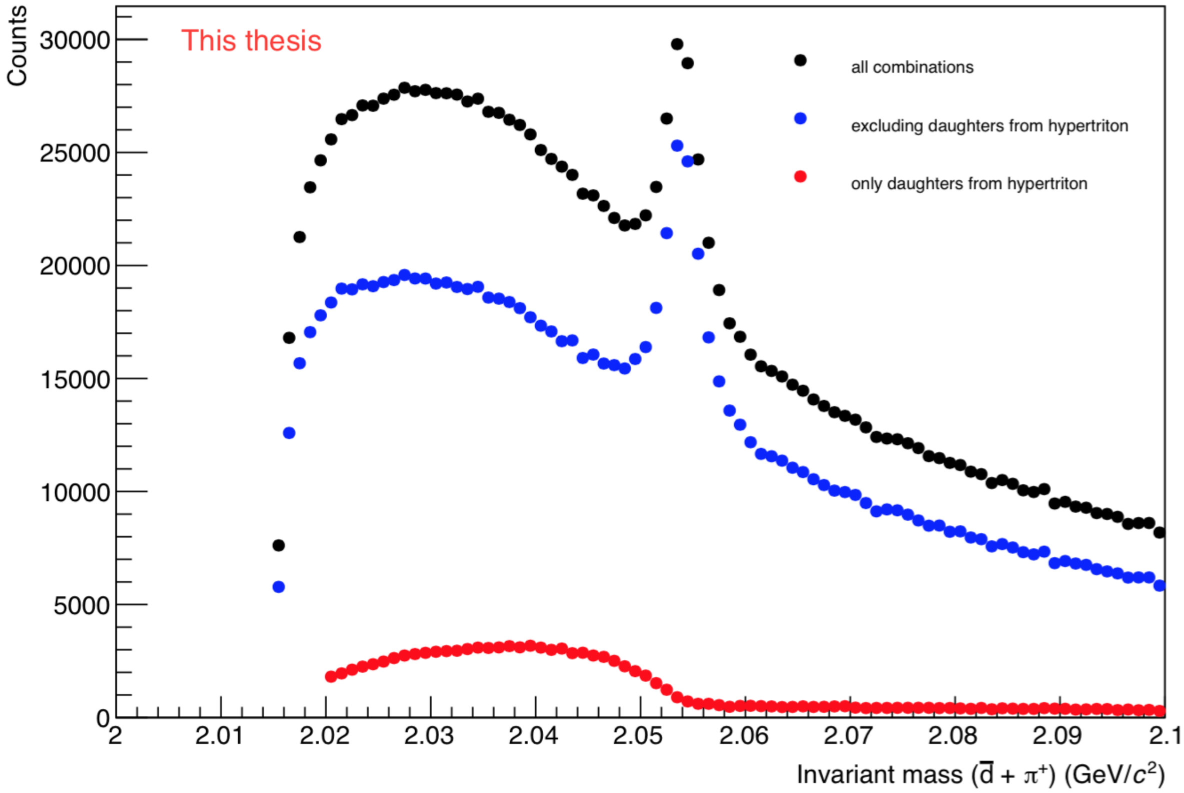

Figure 4.14: Invariant mass distribution in Monte-Carlo of deuterons and pions stemming from $\overline{\Lambda \text{n}}$ bound states and the three-body decay of the hypertriton (black), excluding the three-body decay of the hypertriton (blue) and stemming only from the three-body decay of the hypertriton (red).

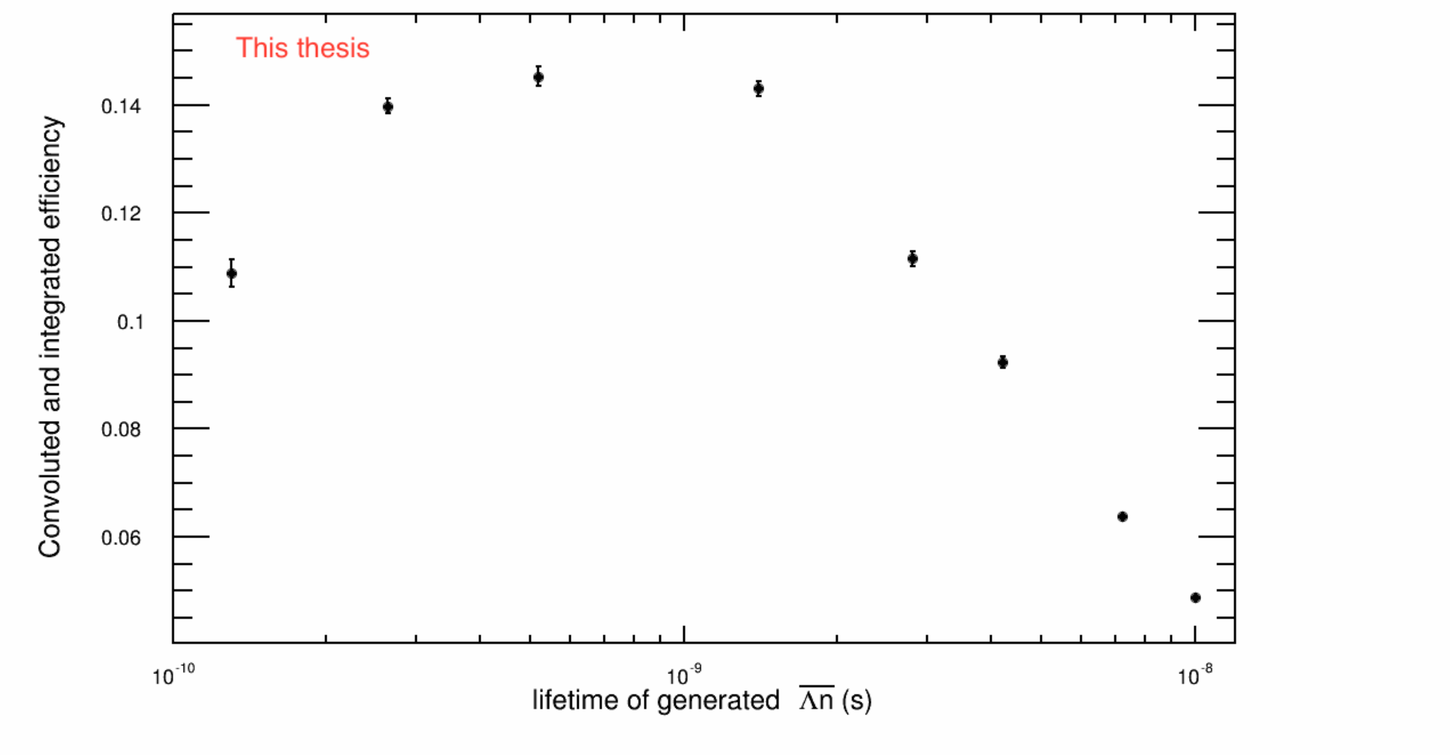

Figure 4.15: The convoluted and integrated efficiencies as a function of the lifetime of the $\overline{\Lambda}$n bound state **without** the cutoff around 2 GeV/c.

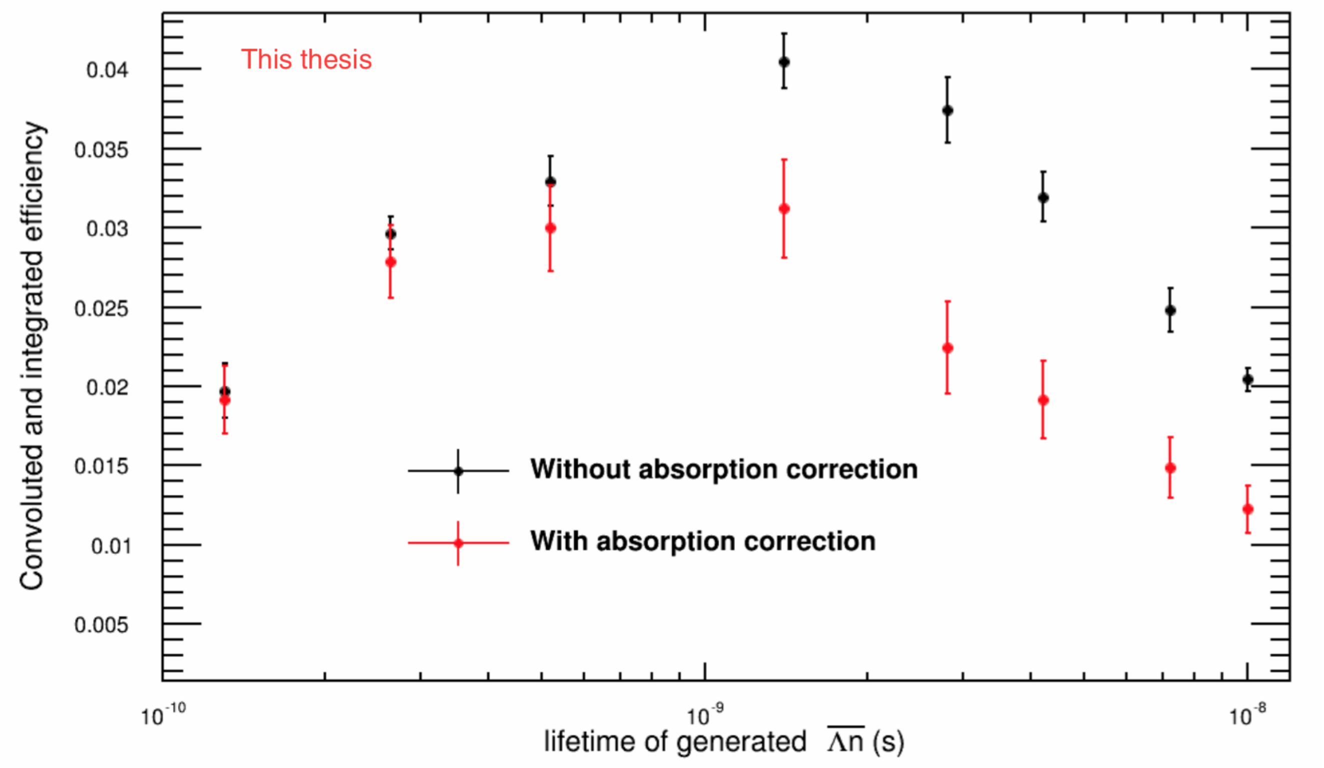

Figure 4.16: The convoluted and integrated efficiencies as function of the lifetime of the $\overline{\Lambda}$n bound state **without** the absorption correction in black and **with** the absorption correction in red.

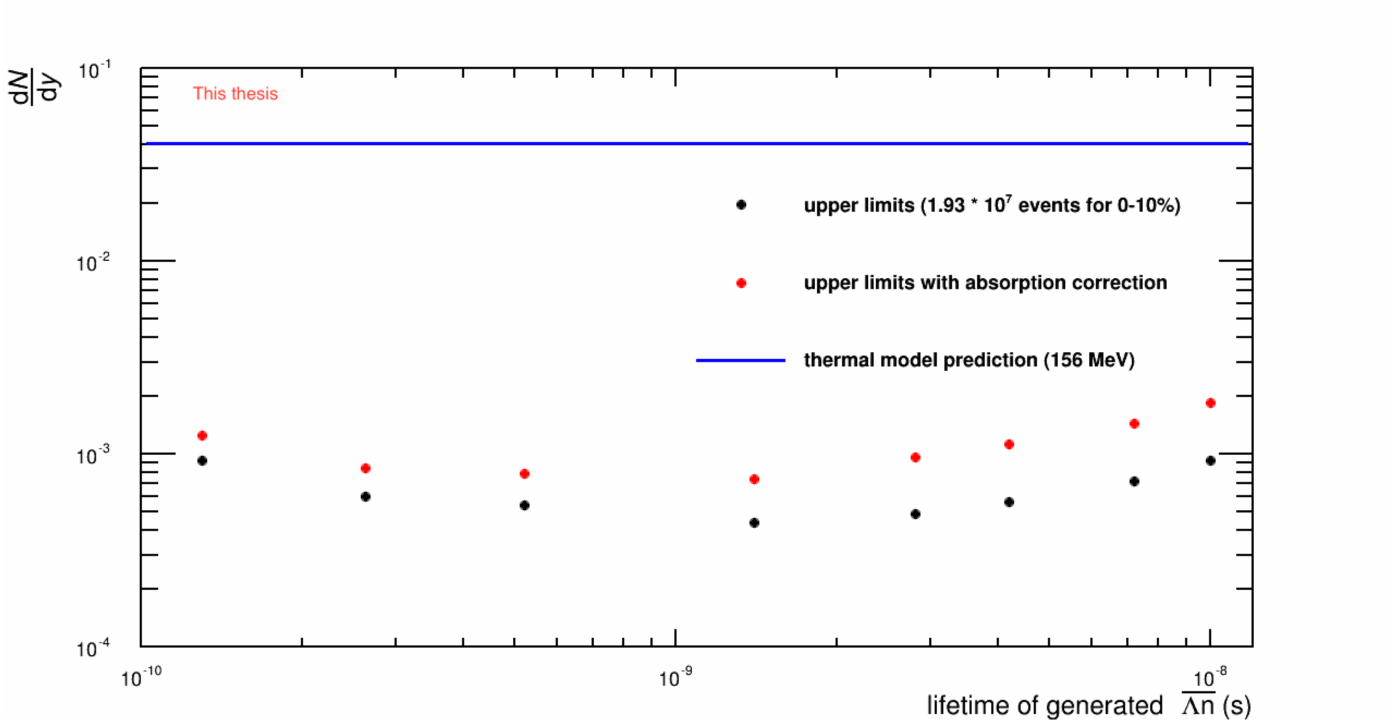

Figure 4.17: Upper limits as function of the lifetime of the $\overline{\Lambda n}$ bound state **without** the absorption correction in black and **with** the absorption correction in red. In addition, the prediction of the thermal model at 156 MeV is drawn.

lifetime (10^{-10} s)	decay length (cm)	multiple of Λ-lifetime	convoluted and integrated efficiency with cutoff	upper limit (99% CL)	absorption
1.3	3.95	0.5	0.020	$9.22 \cdot 10^{-4}$	3%
2.63	7.89	1	0.030	$6.03 \cdot 10^{-4}$	6%
5.2	15.8	2	0.033	$5.46 \cdot 10^{-4}$	9%
14	41.8	5.3	0.041	$4.39 \cdot 10^{-4}$	23%
28	83.6	10	0.037	$4.87 \cdot 10^{-4}$	40%
42	125.4	16	0.032	$5.63 \cdot 10^{-4}$	40%
72	214.97	27	0.025	$7.20 \cdot 10^{-4}$	40%
100	299.8	38	0.020	$9.22 \cdot 10^{-4}$	40%

Table 4.3: Efficiency, upper limit and fraction of absorbed $\overline{\Lambda n}$ bound states in dependence of the lifetime of the $\overline{\Lambda n}$ bound state.

4.1.4 Absorption correction

For the final values of the upper limits the possible absorption of the $\overline{\Lambda \mathrm{n}}$ bound states in the detector material has to be taken into account as well. So far the knowledge on the absorption of anti-nuclei is very poor. Therefore an estimation obtained by Ramona Lea for the anti-hypertriton analysis was used[7]. Table 4.3 summarizes in the last column the assumed fraction of absorbed $\overline{\Lambda \mathrm{n}}$ bound states, assuming that the absorption of the $\overline{\Lambda \mathrm{n}}$ bound states would be as strong as for the anti-hypertriton. The $\overline{\Lambda \mathrm{n}}$ bound state should have a smaller size than the anti-hypertriton, which additionally contains an anti-proton bound in comparison to the $\overline{\Lambda \mathrm{n}}$ bound state. As the absorption of a particle depends also on its size, the assumption that both particles would be absorbed equally strongly can be taken as an upper limit of the absorption of the $\overline{\Lambda \mathrm{n}}$ bound states. Taking the absorption into account, the efficiency has to be decreased by the fractions listed in the last column in Table 4.3. This leads to the red distribution in Figure 4.16, assuming a 7% error on the absorption correction[8]. As the efficiencies are decreasing due to the absorption correction, the upper limits will increase, which can be seen in the red distribution of Figure 4.17.

4.2 H-dibaryon

The search for the H-dibaryon is performed in the decay channel H-dibaryon $\rightarrow \Lambda + \mathrm{p} + \pi^-$, while the Λ is reconstructed in the decay channel $\mathrm{p} + \pi^-$, see also Figure 4.18. The analysis strategy is mainly based on topological particle identification. Compared to the $\overline{\Lambda \mathrm{n}}$ bound state search, the background from knock-out processes in the detector material is strongly reduced as both the Λ and the p come from secondary vertices. Therefore, the search on the particle side is feasible for the H-dibaryon.

For the particle identification of the protons and the pions, a 3σ $\mathrm{d}E/\mathrm{d}x$ cut in the TPC (see section 3.1) is used for both the true Λ and the V0-like topology at the H-dibaryon decay vertex.

The reconstruction of a possible H-dibaryon starts with the identification of a Λ. This uses the same algorithm for a V0 decay topology as in the search for the $\overline{\Lambda \mathrm{n}}$ bound state. If the V0 daughters are identified as a proton and a π^- the invariant mass of this pair is determined. The resulting distribution is shown in Figure 4.19. For the further analysis only those candidates are accepted as Λs, whose invariant mass lie in the 3σ window around of $m_\Lambda = 1.115\,\mathrm{GeV}/c^2$. Afterwards these Λ-candidates are combined with an additional secondary proton and π^-. The topology of this second proton and π^- is similar to a V0, but their invariant mass is different from the Λ. The invariant mass of the H-dibaryon candidate is then calculated from the Four-Vector of the Λ-candidate and the additional proton and π^- properties and is shown in Figure 4.20. Since the latest theoretical discussions (see chapter 1.2) conclude, that the H-dibaryon could either be a slightly bound state or an unbound resonance between the $\Lambda\Lambda$ and the Ξp threshold, these two thresholds are indicated with two arrows in Figure 4.20.

All used track, V0 and kinematic cuts are summarized in Table 4.4. They are especially tuned to cut away pions, which are the most abundant particles produced in central Pb–Pb collisions at the LHC and would otherwise produce a significant background.

For the efficiency estimation the same Monte-Carlo production as for the $\overline{\Lambda \mathrm{n}}$ bound state search is used. In this production also the H-dibaryons are injected flat in p_T. Therefore, in order to determine the p_T integrated efficiency, the Blast-Wave weighting method is used here as well. The used Blast-Wave is shown in blue Figure 4.8 and the resulting weighted efficiency in Figure 4.21. The efficiency before

---

[7] For details see [58].

[8] Uncertainty taken from Table 6 in [58].

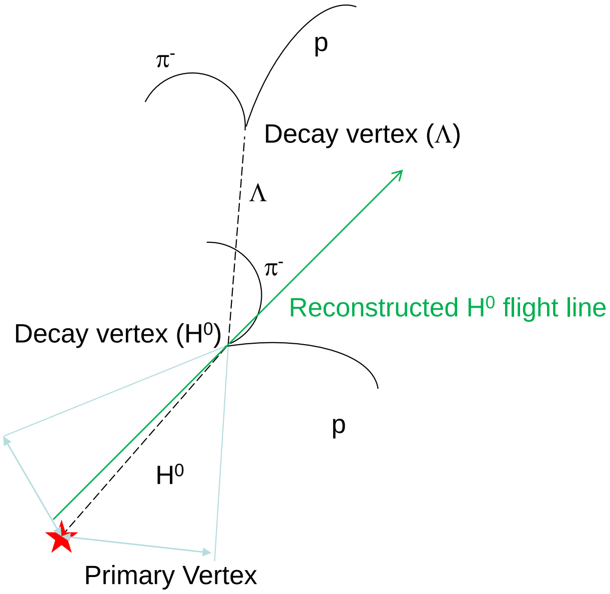

Figure 4.18: Decay topology of the H-dibaryon [56].

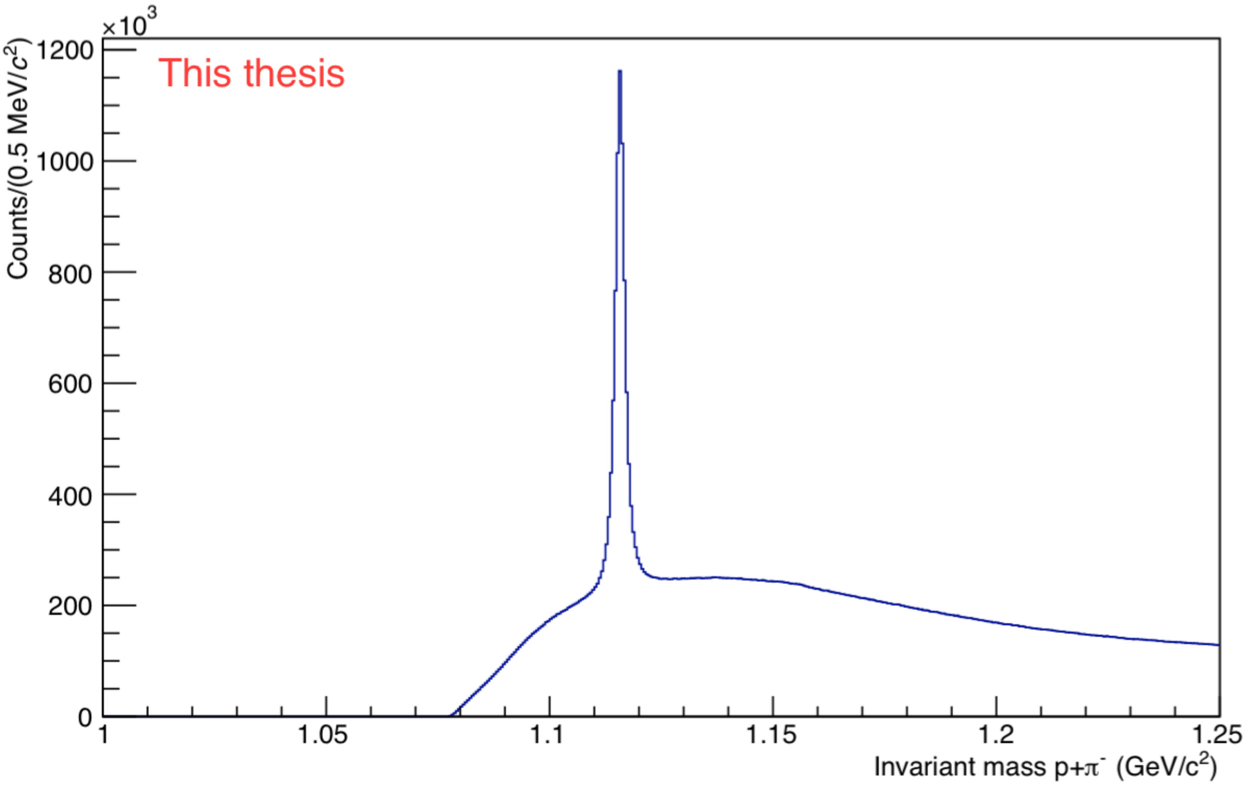

Figure 4.19: Invariant mass of p and π^- for $19.3 \cdot 10^6$ central Pb–Pb events.

cut	**value**
Track cuts	
Kink daughters	rejected
TPC	refit
n_{clusters}(TPC)	> 80
χ^2/cluster	< 5
Pseudo-rapidity	$\|\eta\| <0.9$
V0 and kinematic cuts	
Cosine of pointing angle of H-dibaryon	$\cos(\Theta) > 0.999$
DCA between the V0 daughters	$DCA < 1\,\text{cm}$
DCA between the H-dibaryon daughters	$DCA < 1\,\text{cm}$
DCA between all tracks to the primary vertex	$DCA > 2\,\text{cm}$
PID cut proton	3σ (TPC)
PID cut π^-	3σ (TPC)
Rapidity of mother	$\|y\| < 1$

Table 4.4: Cuts used for the H-dibaryon analysis.

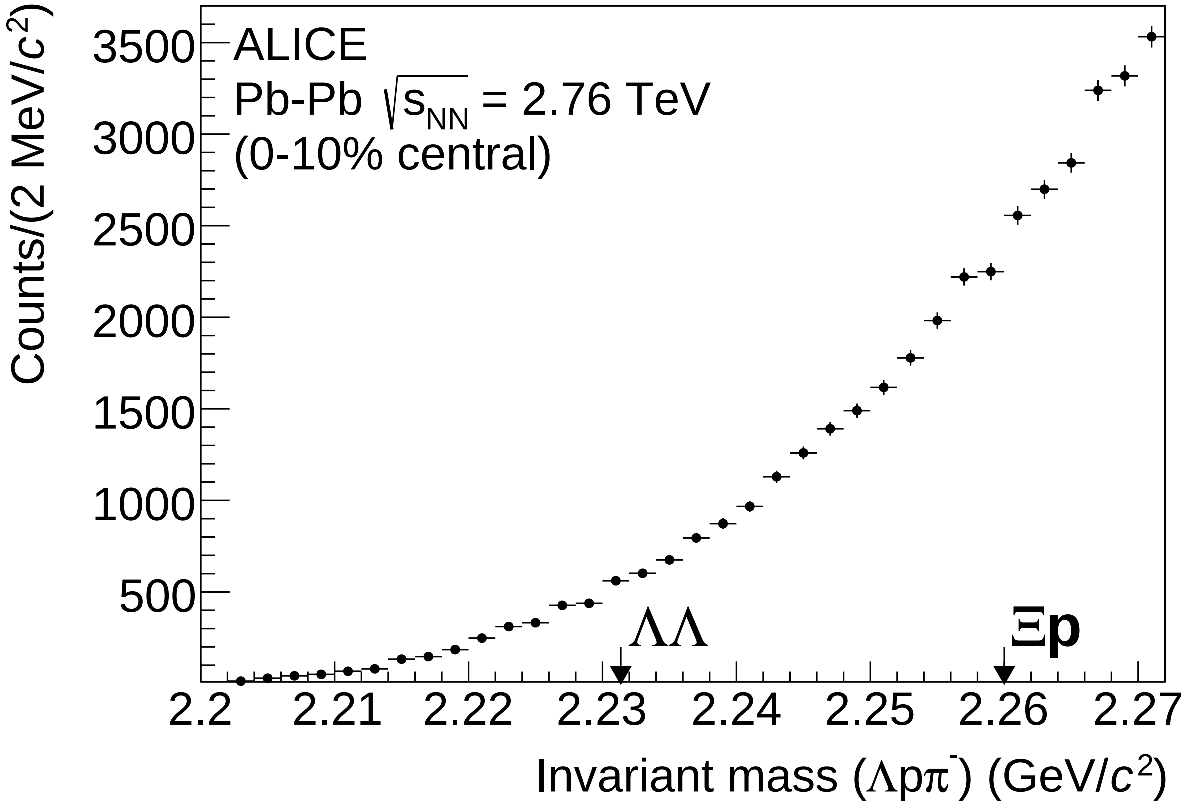

Figure 4.20: Invariant mass of the Λ, p and π^- for $19.3 \cdot 10^6$ central Pb–Pb events [55].

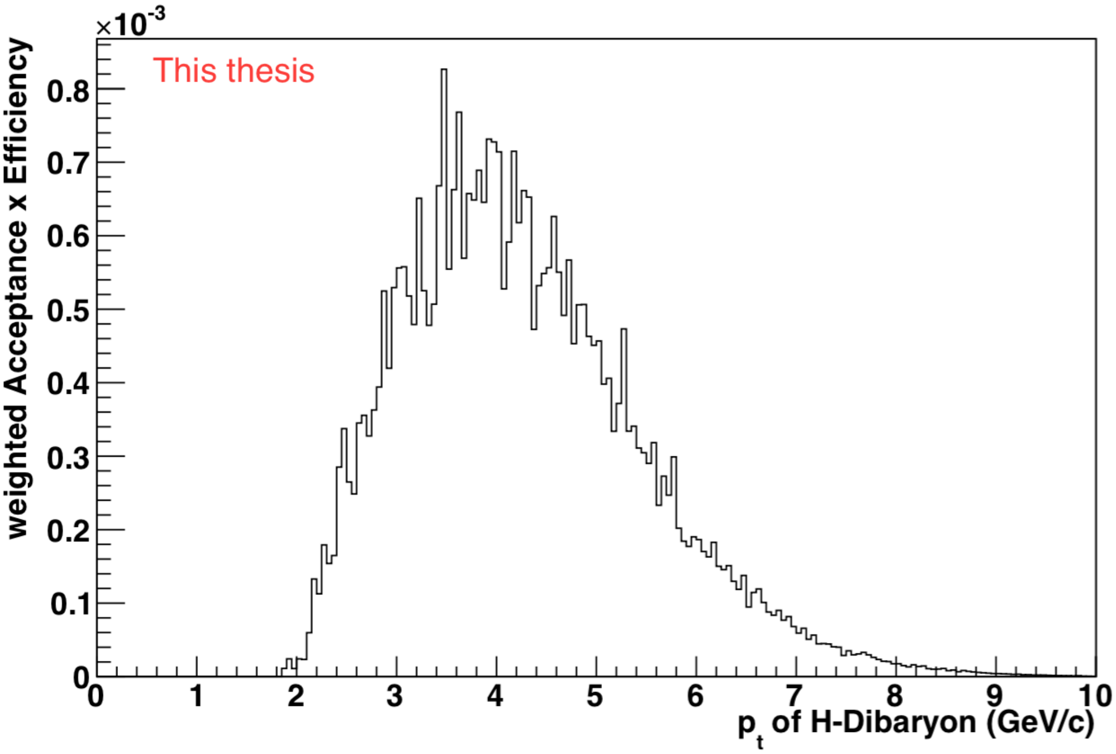

Figure 4.21: Convolution of the Blast-Wave calculation for the H-dibaryon with the extracted acceptance x efficiency from Monte-Carlo.

the weighting is determined to be of the order of 0.04, whereas the overall p_T weighted efficiency 0.0301.

The statistical hadronization model (described in section 1.4) predicts also a value for the possible yield per rapidity unit for the H-dibaryon. For 0 - 10% central Pb–Pb events ($N_\mathrm{part} = 350$) and at a chemical freeze-out temperature of 156 MeV this is $\mathrm{d}N/\mathrm{d}y = 6.03 \cdot 10^{-3}$ (see Figure 1.3). Taking this prediction into account, the number of expected H-dibaryon particles can be calculated in the same manner as for the $\overline{\Lambda \mathrm{n}}$ (see equation 4.1):

$$N_{\mathrm{H}^0,\,\mathrm{exp.\ w/o\ H^0\ BR}} = \underbrace{1.91 \cdot 10^7}_{\mathrm{events}} \cdot \underbrace{0.0301}_{\mathrm{eff.}} \cdot \underbrace{0.64}_{\mathrm{BR}(\Lambda)} \cdot \underbrace{6.03 \cdot 10^{-3}}_{\frac{\mathrm{dN}}{\mathrm{dy}}} \cdot \underbrace{2}_{\mathrm{dy}} \approx 4437\,. \tag{4.2}$$

To get an estimate for the expected yield at a given mass, this value has to be multiplied with the expected branching ratio of the H-dibaryon. From the calculation of J. Schaffner-Bielich and colleagues (see Figure 4.22) it ranges from 0.1 for a deeply bound H to 0.64 at the ΛΛ threshold. Therefore $4437.4 \times 0.1 \approx 444$ H candidates for a deeply bound state and $4437.4 \times 0.64 \approx 2840$ for weakly bound H close to the ΛΛ threshold are expected.

As the expected yield is not observed, the same strategy as for the $\overline{\Lambda \mathrm{n}}$ bound state utilizing the *TRolke* package is used to set an upper limit of the production. This leads to an upper limit of 2.26×10^{-4} for the lightly bound H and 1.18×10^{-4} for the strongly bound H.

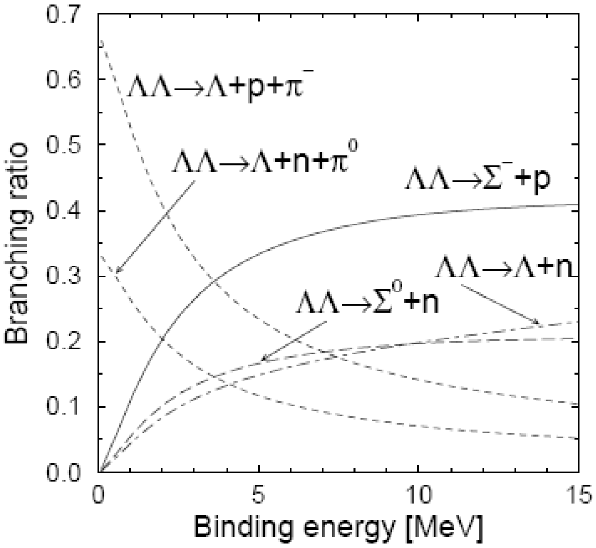

Figure 4.22: Theoretical calculation of the branching ratios of different H-dibaryon decay channels [59].

4.2.1 Systematic uncertainties

Similar to the case of the $\overline{\Lambda \mathrm{n}}$ bound state search the influence of the p_{T} spectrum is the major source of uncertainty, therefore the same strategy is used to determine it. As the mass of the H-dibaryon in the investigated cases should as well lie between the deuteron and the ^{3}He, their Blast-Wave fits (see Figure 4.8) can also be used here as the extreme cases for the systematic studies. The resulting uncertainty for the efficiency from the unknown p_{T}-distribution is 0.0083. To further estimate the uncertainty of the measured invariant mass, the topological cuts, which are shown in table 4.4, are varied for data and Monte-Carlo systematically. This leads to a change in the efficiency up to 25%, resulting in an total uncertainty of 30% on the upper limit.

4.2.2 Lifetime studies

The influence of the lifetime on the efficiency and therefore on the upper limit was studied using the same seven Monte-Carlo productions as for the $\overline{\Lambda \mathrm{n}}$ bound state. In each of these productions a different lifetime of the H-dibaryon was assumed (see section 4.1.3). The behavior of the efficiency is shown in Figure 4.23, whereas the result for the upper limit is shown in Figure 4.24. The upper limit is strongest for an assumed lifetime of the free Λ ($2.63 \cdot 10^{-10}$ s). It rises until it almost reaches the prediction from the statistical hadronization model for the longest, though very unlikely, investigated lifetime of $1 \cdot 10^{-8}$ s.

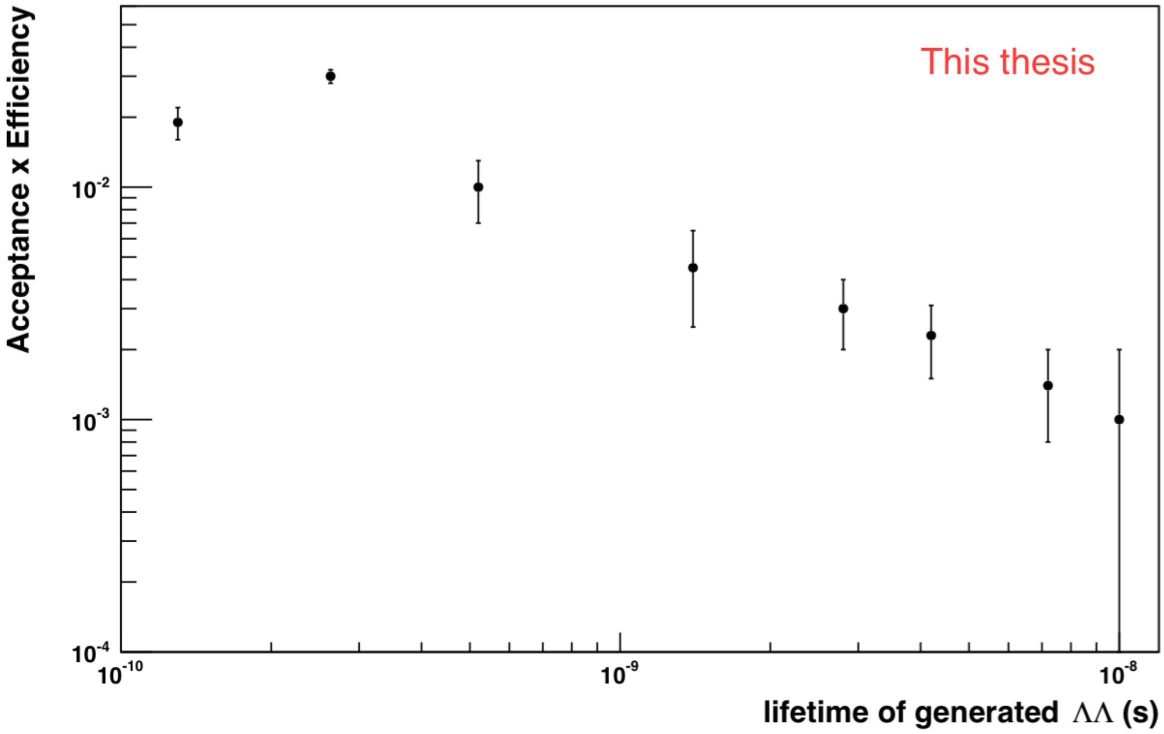

Figure 4.23: Efficiency dependence on the lifetime of the H-dibaryon.

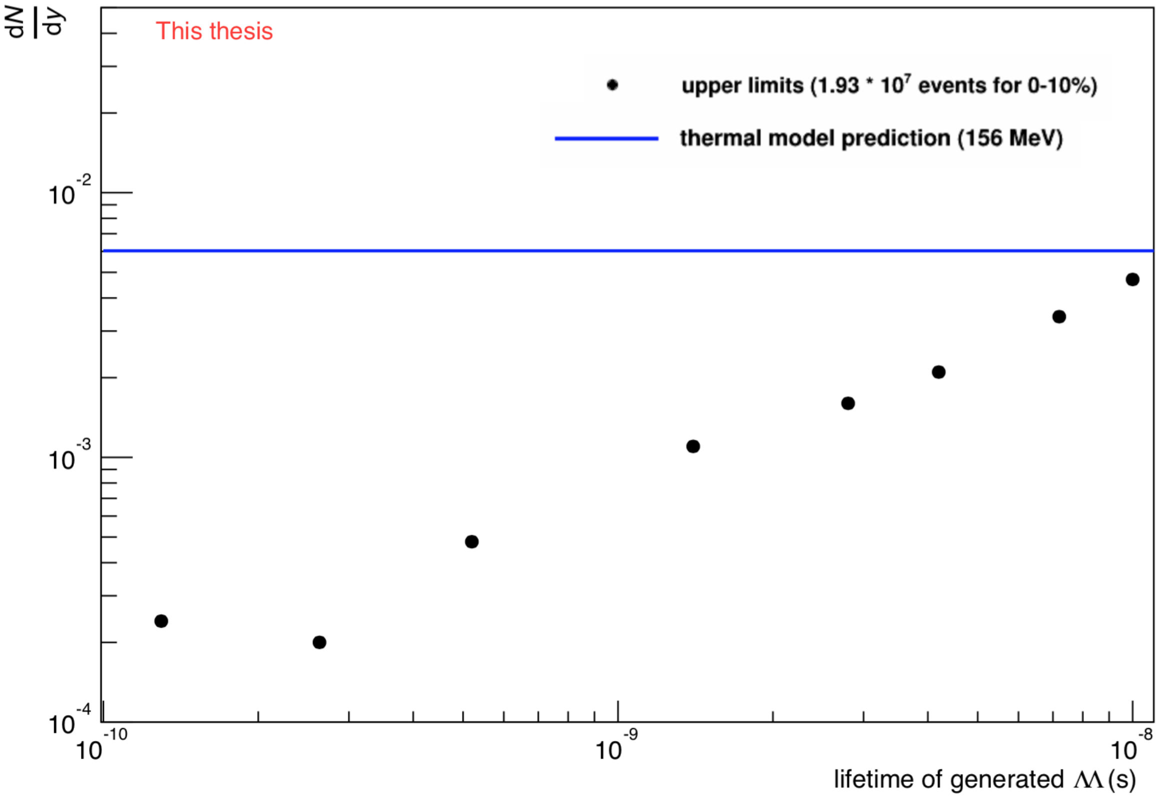

Figure 4.24: Upper limits as function of the lifetime of the H-dibaryon. In addition, the prediction of the thermal model at 156 MeV is drawn.

5 (Anti-)Alpha production

For the measurement of the alpha and anti-alpha production 38.75 million Pb–Pb events at $\sqrt{s_{\mathrm{NN}}} = 2.76$ TeV from the data taking period in 2011 are inspected. In order to gain as much statistics as possible, a mix of central, semi-central and minimum bias triggers is used. All events with a centrality between 0 and 80% and a primary vertex which falls within a radius $\mid V_z \mid < 10$ cm around the interaction point are accepted. The centrality selection is done using the VZERO detector (see chapter 2). Figure 5.1 shows the resulting centrality distribution, whereas Table 5.1 summarizes the number of events analyzed in each centrality class. In addition, the average $\mathrm{d}N/\mathrm{d}\eta$ for each centrality class is given. This is needed later in order to be able to determine the measured yield in only one centrality class, see section 5.5.

centrality	**number of events** $\times 10^6$	$\mathbf{d}N/\mathbf{d}\eta$
0 - 10 %	20.72	1447.5 ± 57
10 - 50 %	17.40	749 ± 47
50 - 80 %	0.63	86 ± 8

Table 5.1: Number of events analyzed in each centrality class and the corresponding $\mathrm{d}N/\mathrm{d}\eta$ [60].

The track cuts used in this analysis are listed in Table 5.2. They ensure a minimum quality of the tracks, but are on the other hand not very strict in order to avoid losing a ^{4}He or $^4\overline{\mathrm{He}}$ candidate. A restriction on the ***D**istance-of-**C**losest **A**pproach (DCA)* of the track to the primary vertex in the xy-plane (DCA_{xy}) and in the beam direction (DCA_z) is applied to ensure that only primary particles are selected. In addition, the matching of the tracks between the TPC and the TOF detector is required.

cut	**value**
Kink daughters	rejected
TPC	refit
$\mathrm{n}_{\mathrm{clusters}}$(TPC)	> 80
χ^2/clusters	< 4
$\mathrm{n}_{\mathrm{clusters}}$(ITS)	> 2
Track matching between TPC and TOf	required
DCA to the primary vertex	$DCA_{xy} < 0.1$ cm
DCA to the beam direction	$DCA_z < 1.0$ cm
Pseudo-rapidity	$\lvert\eta\rvert < 0.9$

Table 5.2: Summary of track cuts.

For the identification of the ^{4}He and $^4\overline{\mathrm{He}}$, the specific energy loss $\mathrm{d}E/\mathrm{d}x$ measured with the TPC is used, see section 3.1 for details. In a first step all events that have at least one particle with a $\mathrm{d}E/\mathrm{d}x$ corresponding to a ^{3}He, respectively $^3\overline{\mathrm{He}}$, or a higher z particle, are selected. This offline trigger is indicated with the red dashed line in Figure 5.2, on the left side for particles and right side for anti-particles.[1] Then the ^{4}He ($^4\overline{\mathrm{He}}$) candidates are identified in a 3σ range around their theoretical Bethe-Bloch curve.

---

[1] Figure 3.1 in chapter 3.1 shows the TPC $\mathrm{d}E/\mathrm{d}x$ spectrum for negative particles without this selection.

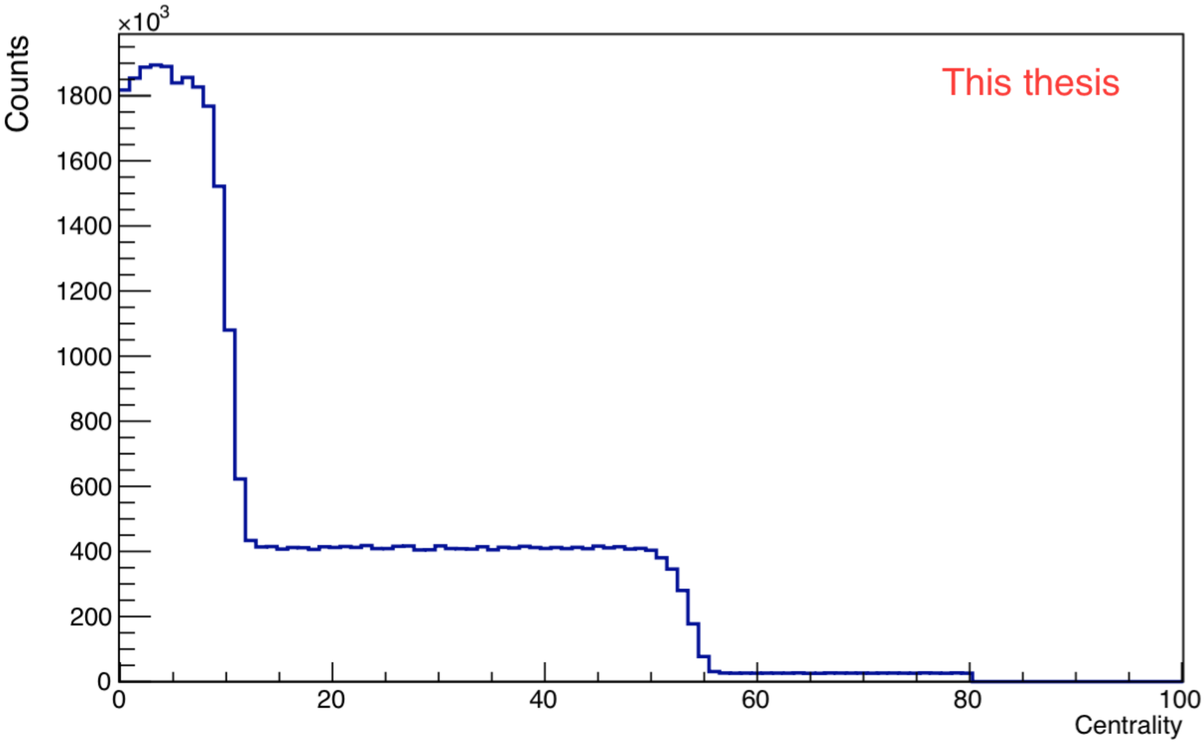

Figure 5.1: Centrality distribution including all analyzed minimum bias, central and semi-central events, in a 0-80% centrality range of the data sample used.

The 3σ TPC $\mathrm{d}E/\mathrm{d}x$ selection is not sufficient enough, especially at higher rigidity p/z (the momentum p of the particle divided by its charge number z) where the two Bethe-Bloch curves of ^{4}He ($^4\overline{\mathrm{He}}$) and ^{3}He ($^3\overline{\mathrm{He}}$) are very close. Therefore, additional information from the TOF detector (see chapter 2 and 3.2) is used.

With a mass $m = 3.73$ GeV/c^2 the corresponding m^2/z^2 for ^{4}He is 3.48 GeV^2/c^4. For ^{3}He with a mass $m = 2.83$ GeV/c^2 the m^2/z^2 is 2.00 GeV^2/c^4. Due to the finite resolution of the detector, the candidates will not show up exactly at this value in the m^2/z^2 distribution, but as a peak with a certain width. Therefore, a mass window, in which the (anti-)alpha candidates are expected, has to be defined by fitting a Gaussian with an exponential tail on the right side (because of the TOF signal shape) to the measured m^2/z^2 distribution:

$$\text{TOF signal function} = \begin{cases} P0 \cdot e^{-\frac{1}{2}\left(\frac{x-P1}{P2}\right)^2}, & \text{if } \mathrm{x} \leq \mathrm{P3}+\mathrm{P1} \\ P0 \cdot e^{-\frac{1}{2}\left(\frac{P3}{P2}\right)^2} \cdot e^{-P3 \cdot \frac{x-P3-P1}{P2^2}}, & \text{if } \mathrm{x} > \mathrm{P3}+\mathrm{P1} \end{cases} \tag{5.1}$$

where $P0$ is the normalization, $P1$ the mean value, $P2$ the sigma and $P3$ the value where the exponential tail on the right side of the TOF signal distribution starts to be effective. In order to increase the statistics for the fit, the distribution for alpha and anti-alpha particles are fitted simultaneously and, in addition, secondary alphas are also included. This is done by opening the cuts on the DCA. In the plane perpendicular to the beam axis the DCA_{xy} cut is opened from < 0.1 cm to < 3 cm, whereas the DCA_z cut along the beam axis is opened from < 1 cm to < 2 cm. The resulting fit together with the $\frac{m^2}{z^2}$ distribution is shown in Figure 5.3. The four points on the left side of the distribution belong to ^{3}He and $^3\overline{\mathrm{He}}$, but due

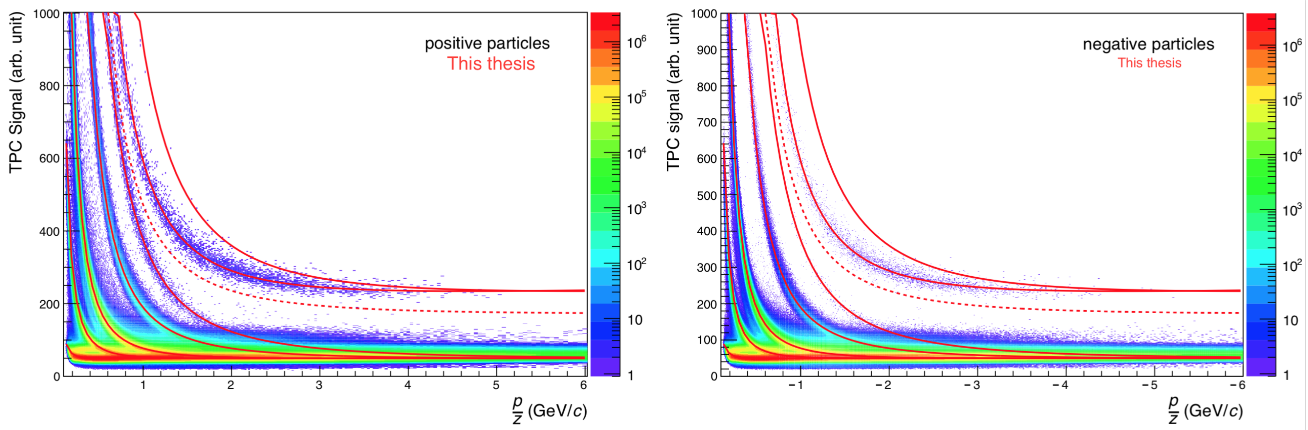

Figure 5.2: TPC dE/dx spectrum for positive (left) and negative (right) particles after a selection (indicated with the red dotted line) of events that contain at least one ^{3}He respectively $^3\overline{\text{He}}$ or ^{4}He respectively $^4\overline{\text{He}}$ candidate. In full red lines the Bethe-Bloch parametrization for the different particle species are also shown.

to the zoom to the mass region of (anti-)alphas, the corresponding peak is not fully visible. The resulting fit parameters are:

- Normalization ($P0$) = 22.35 counts
- Mean ($P1$) = 3.40 GeV$^2/c^4$
- Sigma ($P2$) = 0.18 GeV$^2/c^4$
- Tail ($P3$) = 0.14 GeV$^2/c^4$

Based on the fit result, the mass window can be defined as follows:

- Lower limit (left side): Mean - 3σ = (3.40 - 3 · 0.18) GeV$^2/c^4$ = 2.86 GeV$^2/c^4$.
- Upper limit (right side): Due to the tail on this side, the fit function has to be integrated until 99.74% has been reached, which corresponds to 3σ. Thus, the upper limit of the mass window is given by 4.87 GeV$^2/c^4$.

Therefore, ^{4}He or $^4\overline{\text{He}}$ particles are expected to lie in the range between $2.86\,(\text{GeV}^2/c^4) < \frac{m^2}{z^2} < 4.87$ (GeV$^2/c^4$).

The 3σ dE/dx selection with the TPC and requirement of a hit in the TOF is not sufficient to suppress the underlying background, either from ^{3}He ($^3\overline{\text{He}}$) contamination or from TOF mismatch. Therefore the ^{4}He and $^4\overline{\text{He}}$ particles can not be clearly identified, yet. This is the crucial part of the analysis in order to finally have a clear sample of ^{4}He and $^4\overline{\text{He}}$ particles.

The background due to mismatch in the TOF detector is reduced by applying a stricter cut in the dE/dx vs. $\beta\gamma = p/m_{\text{TOF}}$ distribution: All candidates which fulfill the track cuts and have a dE/dx value corresponding to the expectation of being at minimum a (anti-)^{3}He are selected. These candidates are filled in a 2D histogram, taking the TPC dE/dx on the y-axis and $\beta\gamma = p/m_{\text{TOF}}$ on the x-axis. The resulting 2D histograms are shown in Figure 5.4. The mean and the standard deviation σ of these distributions is determined via fits to the distributions. Afterwards, all candidates, which lie outside a ±3σ range

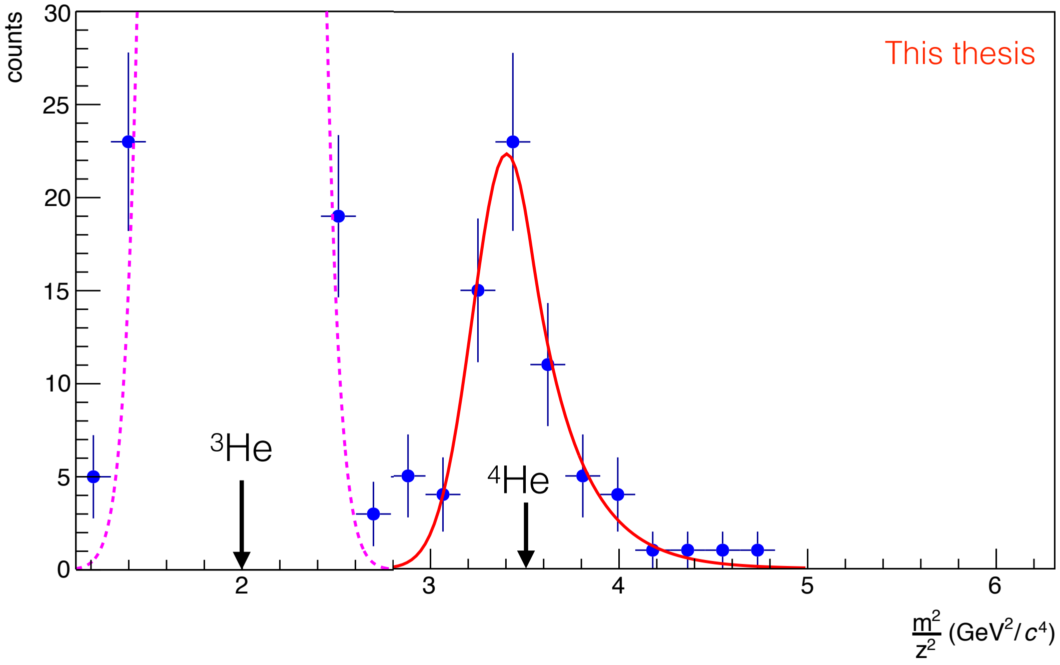

Figure 5.3: m^2/z^2 distribution for particles and anti-particles, including also secondary particles to increase the statistics for the fit. The fit result is shown in red. The y-axis is expanded in order to show the peak for alphas and anti-alphas. Therefore the peak corresponding to ^{3}He is not fully visible. Only the two points below 1 GeV$^2/c^4$, which correspond to the rise of the ^{3}He peak, and the points around 2.5 GeV$^2/c^4$, where the peak goes down again, are visible.

around the determined mean, are excluded from the further analysis.

To study systematic effects originating from the TPC PID selection stricter cuts on the specific energy loss measurement are investigated (the remaining background due to a possible ^{3}He ($^3\overline{\text{He}}$) contamination is investigated in section 5.2): whereas the upper limit of 3σ is always kept, the lower limit is decreased in units of 0.5 from 3σ down to 0σ. In this way the selection goes further and further away from the ^{3}He ($^3\overline{\text{He}}$) band in the TPC until only the upper half of the ^{4}He ($^4\overline{\text{He}}$) TPC band is kept.

Figure 5.5 and 5.6 (for positive particles) and 5.7 and 5.8 (for negative particles) show some example plots for m^2/z^2 (on the left) and the β_{TOF} (on the right) distributions with the $\pm 3\sigma$ cut in the dE/dx vs. $\beta\gamma$ distribution applied for the different TPC dE/dx selections. For the final yield the mean of all nine different TPC selections is determined (see section 5.7).

5.1 Contamination from secondary particle production

The production of anti-particles from the detector material is strongly suppressed and therefore negligible. However, for particles this is not the case and the alpha-particles stemming from these processes have to be estimated. The TPC dE/dx spectrum for true alpha particles is investigated in a Monte-Carlo simulation. Due to the low statistics of secondary alphas in the Monte-Carlo sample, the template fit method, which is successfully used for lighter nuclei [9], can not be used for this analysis. The amount of statistics needed is so large, that it will also not be possible to produce such a Monte-Carlo sample in the near future. Therefore, the TPC dE/dx spectrum for only primary and secondary alphas is investigated instead. The corresponding distributions are shown in Figure 5.9: In the left panel for primary and in the right panel for secondary alphas. Since the distribution for secondary alphas stops at $p/z = 2$ GeV/c, a cut $p/z > 2$ GeV/c seems to be reasonable in order to reject the background from knocked-out

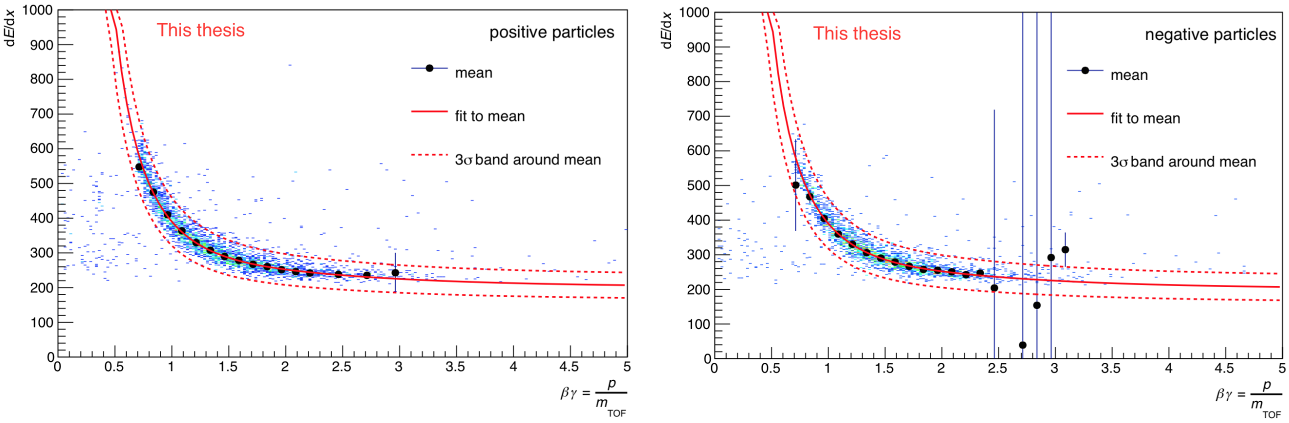

Figure 5.4: TPC dE/dx as function of $\beta\gamma = p/m_{\text{TOF}}$ for all candidates which fulfill the track cuts and have a dE/dx of at minimum a (anti-)^{3}He. The black dots show the mean of the distribution and the solid red line shows the fit to this mean. The red dotted lines indicate a 3σ range around the mean.
On the left side for positive particles and on the right side for negative Particles.

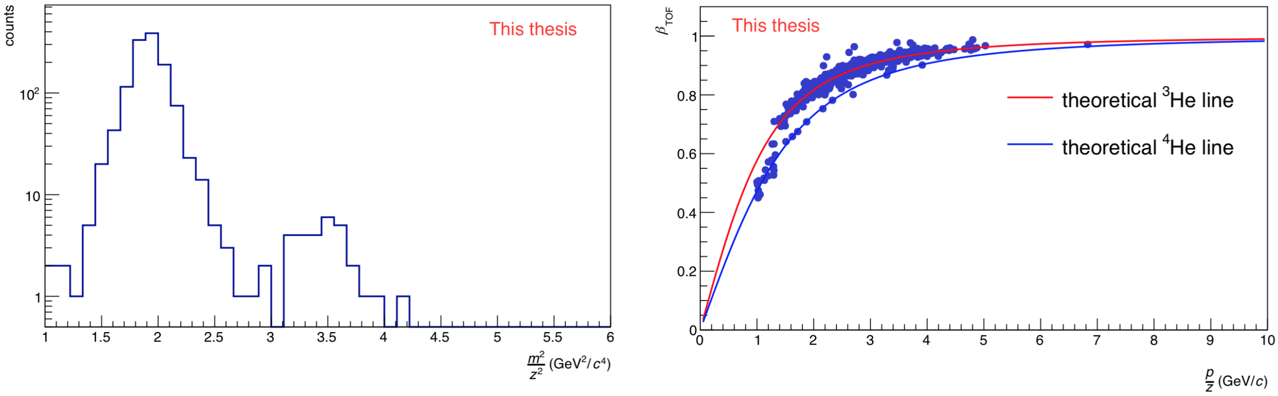

Figure 5.5: Distributions for positive particles using the track cuts listed in table 5.2, a -3σ to 3σ TPC dE/dx selection and a $\pm 3\sigma$ cut in dE/dx vs $\beta\gamma$.
Left: m^2/z^2 distribution. The ^{4}He particles are expected to lie between $2.86\,(\text{GeV}^2/c^4) < m^2/z^2 < 4.87\ (\text{GeV}^2/c^4)$.
Right: β_{TOF} as function of the rigidity (p/z). The two lines indicate the theoretical ^{3}He (red) and ^{4}He (blue) lines.

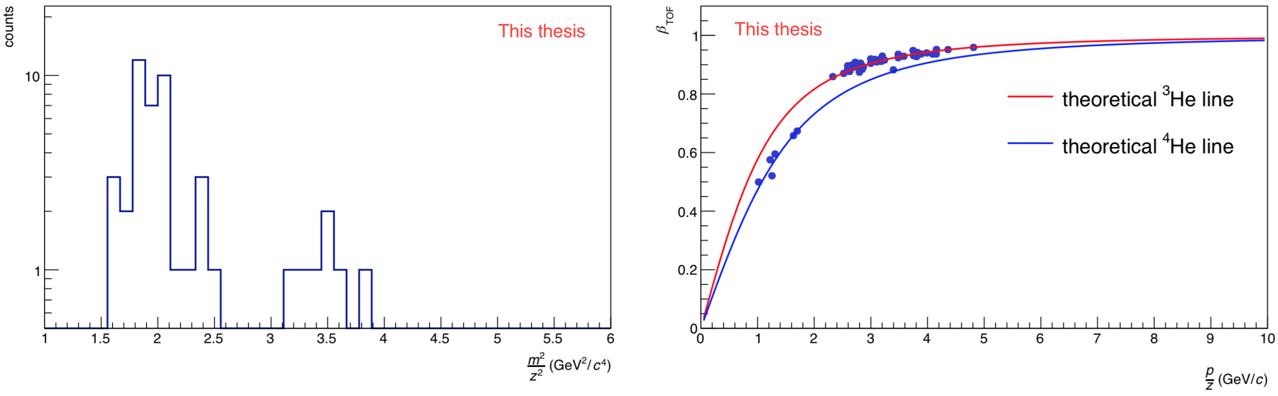

Figure 5.6: Distributions for positive particles using the track cuts listed in table 5.2, a 0σ to 3σ TPC $\mathrm{d}E/\mathrm{d}x$ selection and a $\pm 3\sigma$ cut in $\mathrm{d}E/\mathrm{d}x$ vs $\beta\gamma$.
Left: m^2/z^2 distribution. The ^{4}He particles are expected to lie between $2.86\,(\mathrm{GeV}^2/c^4) < m^2/z^2 < 4.87\ (\mathrm{GeV}^2/c^4)$.
Right: β_{TOF} as function of the rigidity (p/z). The two lines indicate the theoretical ^{3}He (red) and ^{4}He (blue) lines.

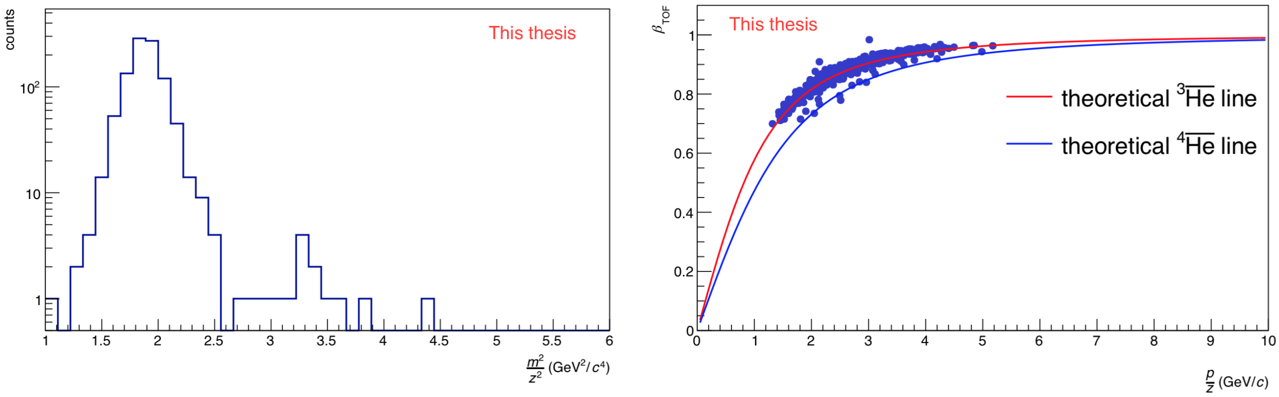

Figure 5.7: Distributions for negative particles using the track cuts listed in table 5.2, a -3σ to 3σ TPC $\mathrm{d}E/\mathrm{d}x$ selection and a $\pm 3\sigma$ cut in $\mathrm{d}E/\mathrm{d}x$ vs $\beta\gamma$.
Left: m^2/z^2 distribution. The $^{4}\overline{\mathrm{He}}$ particles are expected to lie between $2.86\,(\mathrm{GeV}^2/c^4) < m^2/z^2 < 4.87\ (\mathrm{GeV}^2/c^4)$.
Right: β_{TOF} as function of the rigidity (p/z). The two lines indicate the theoretical $^{3}\overline{\mathrm{He}}$ (red) and $^{4}\overline{\mathrm{He}}$ (blue) lines.

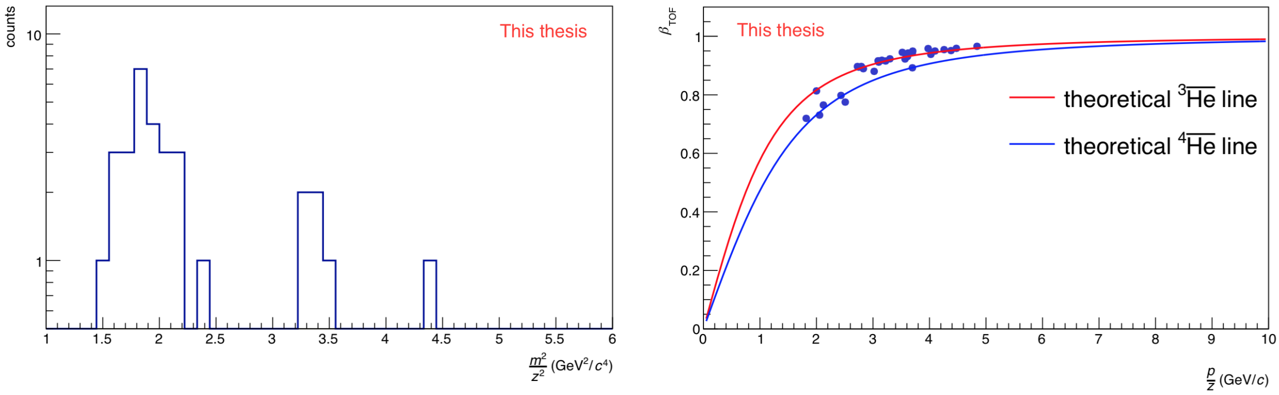

Figure 5.8: Distributions for negative particles using the track cuts listed in table 5.2, a 0σ to 3σ TPC $\mathrm{d}E/\mathrm{d}x$ selection and a $\pm 3\sigma$ cut in $\mathrm{d}E/\mathrm{d}x$ vs $\beta\gamma$.
Left: m^2/z^2 distribution. The $^4\overline{\text{He}}$ particles are expected to lie between $2.86\,(\text{GeV}^2/c^4) < m^2/z^2 < 4.87\ (\text{GeV}^2/c^4)$.
Right: β_{TOF} as function of the rigidity (p/z). The two lines indicate the theoretical $^3\overline{\text{He}}$ (red) and $^4\overline{\text{He}}$ (blue) lines.

alphas. The number of raw counts in $2.86\,(\text{GeV}^2/c^4) < m^2/z^2 < 4.87\ (\text{GeV}^2/c^4)$ without and including a $p/z > 2$ GeV/c cut are summarized in Table 5.3. For comparison here also the numbers for anti-alphas are listed, but the influence here is much smaller. This is expected because most (80 %) of the (anti-)^{4}He yield should sit above 2 GeV/c, see the Blast-Wave distribution in Figure 5.11.

	alpha		anti-alpha (only for comparison)	
sigma range TPC	**raw counts no p/z cut**	**raw counts with $p/z > 2$ GeV/c cut**	**raw counts no p/z cut**	**raw counts with $p/z > 2$ GeV/c cut**
-3σ to 3σ	30	9	14	11
-2.5σ to 3σ	30	9	13	11
-2σ to 3σ	28	8	13	11
-1.5σ to 3σ	26	7	12	11
-1.0σ to 3σ	25	7	11	10
-0.5σ to 3σ	20	4	10	9
0σ to 3σ	17	3	8	7

Table 5.3: Comparison of raw counts in $2.86\,(\text{GeV}^2 c^4) < \frac{m^2}{z^2} < 4.87\ (\text{GeV}^2/c^4)$ with and without using a $p/z > 2$ GeV/c cut. This will only be used for alphas, but for comparison the numbers for anti-alphas are also given.

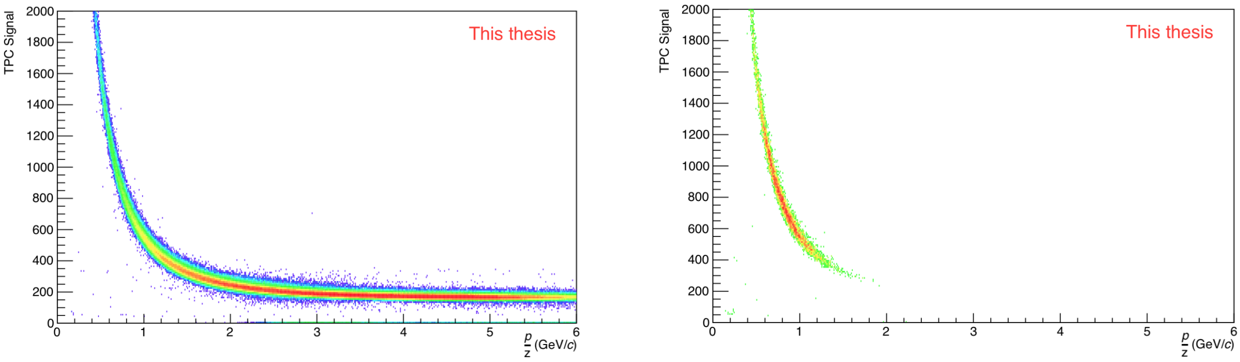

Figure 5.9: TPC dE/dx spectrum for true alphas in an (anti-)alpha enhanced Monte-Carlo sample. Left: Only primary alphas. Right: Only secondary alphas.

5.1.1 Estimation of the remaining contamination of secondary particle production

As it is not possible to simulate as many events in Monte Carlo as exist in data, the below described procedure is used in order to estimate the remaining secondary background above $p/z > 2$ GeV/c:
The TPC dE/dx spectrum for true secondary alphas in the alpha enhanced sample has been projected on the x-axis. The result is shown on the left side of Figure 5.10. The obtained distribution is fitted with an exponential function (shown in red). The fitted function is integrated above 2 GeV/c and the result is normalized to the bin width. This leads to a value of 0.9, which has to be weighted by the number of events in Monte-Carlo (269962) and in data ($38.74 \cdot 10^6$). Leading to a final secondary contamination above $p/z > 2$ GeV/c of $(0.9 \cdot 38.74 \cdot 10^6)/269962 = 129.3$ counts. So far this was done for all true secondary alphas in Monte-Carlo without applying the track cuts used in data. If the same track cuts from data are also applied in Monte-Carlo, only 5 secondary alphas from the former 5375 candidates survive. As such, the described procedure can not be done. Instead, the previously mentioned 129.3 counts will be reduced by a factor 1000 ($5/5375 \approx 1 \cdot 10^{-3}$), which is the difference in Monte-Carlo between the number of secondary alphas with and without using the track cuts. This leads to 0.13 counts above $p/z > 2$ GeV/c. Introducing a safety factor of 10 leads to the final value of an expected maximum of 1.3 counts for the remaining secondary alpha particles above $p/z > 2$ GeV/c. If the uncertainty of the fit is used instead, this leads to a maximum of 0.17 counts. Since the limited statistics in Monte-Carlo introduces a large uncertainty, the 1.3 counts will be assigned as systematic uncertainty for the secondary contamination.

5.2 Background estimation

Although the different TPC PID cuts, the TOF matching cut and the rigidity cut (only for alphas) reduce the underlying background in the m^2/z^2 distribution significantly, it is possible that still some background from TOF mismatch or (anti-)^{3}He particles in the mass region of (anti-)^{4}He remains. This magnitude of background needs to be estimated. Therefore, the cut on the TOF matching is inverted and the m^2/z^2 distributions are investigated outside the $\pm 3\sigma$ cut in dE/dx vs $\beta\gamma$. Afterwards, these candidates are filled into the m^2/z^2 distribution. A fit outside the (anti-)^{4}He mass region is performed, using a linear function. Empty bins are appropriately taken into account in the fit procedure. The results are summarized in Table 5.4.

Due to low statistics, this method can not be used for very strict TPC PID cuts as there are no counts in the m^2/z^2 distribution outside the peak region. Therefore, a different approach is used here, which assumes a constant ratio of ^{3}He to background counts (Constant ratio = (^{3}He / background counts)). In order

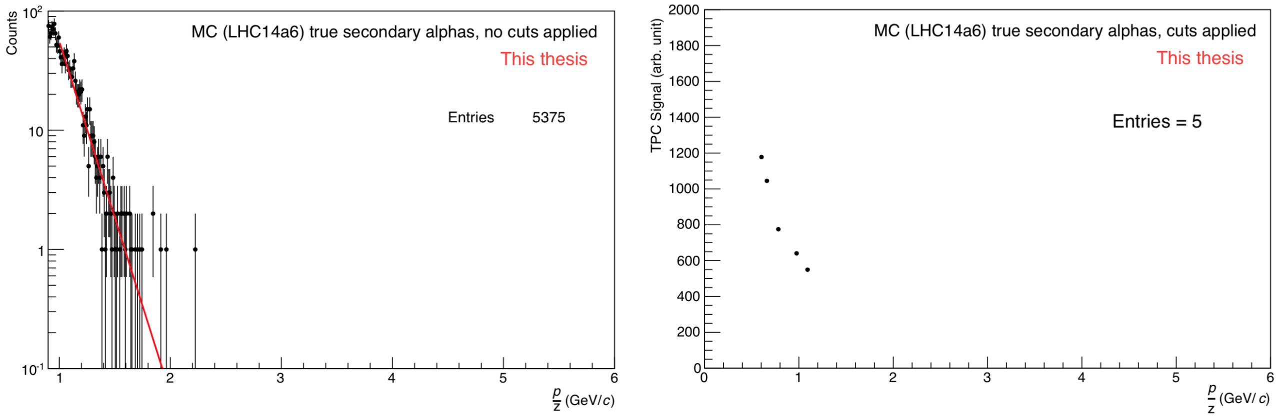

Figure 5.10: TPC dE/dx spectrum for true secondary alphas in Monte Carlo. On the left side the projection on the x-axis is shown together with an exponential fit. Here no track cuts have been applied. On the right side the same track cuts as in data have been applied.

	alpha				anti-alpha			
sigma range TPC	**raw counts ^{4}He**	**raw counts ^{3}He**	**estimated background**	**background subtracted raw counts**	**raw counts $^4\overline{\text{He}}$**	**raw counts $^3\overline{\text{He}}$**	**estimated background**	**background subtracted raw counts**
-3σ to 3σ	9	1082	3.28	5.72	14	1028	5.25	8.75
-2.5σ to 3σ	9	892	2.63	6.37	13	785	4.60	8.40
-2σ to 3σ	8	673	1.97	6.03	13	561	3.93	9.07
-1.5σ to 3σ	7	472	1.97	5.03	12	376	1.97	10.03
-1.0σ to 3σ	7	314	0.65	6.35	11	227	1.32	9.68
-0.5σ to 3σ	4	183	0.65	3.35	10	138	0.79	9.21
0σ to 3σ	3	109	0.32	2.68	8	75	0.43	7.57

Table 5.4: Summary of the raw counts and estimated background. The red marked background is estimated using a constant ratio of ^{3}He to background.

to use this estimation, the number of (anti-)^{3}He needs to be determined for each TPC PID selection. The ratio of ^{3}He to background counts is calculated for each TPC PID bin, in which the estimation with the likelihood fit was still possible. The mean value of this ratio is 343 for positive particles and 175 for negative particles. Therefore the background can be estimated with:

- Background $= \dfrac{^3\text{He}}{343}$ for positive particles
- Background $= \dfrac{^3\overline{\text{He}}}{175}$ for negative particles

5.3 Efficiency and acceptance correction

The Efficiency × Acceptance is determined by using the Monte Carlo production mentioned in section 5.1, which is enhanced with (anti-)alpha particles. The efficiency is p_{T} dependent, but due to the very low number of candidates the p_{T} spectrum of the (anti-)^{4}He particles can not be measured. Therefore, the efficiency has to be weighted with the shape of the p_{T} spectrum. For this a Blast-Wave calculation (see Figure 5.11) is used. This calculation uses a Blast-Wave fit to the measured deuteron and ^{3}He spectra in Pb–Pb [9] as input. The procedure is the same as for the search of the exotic bound

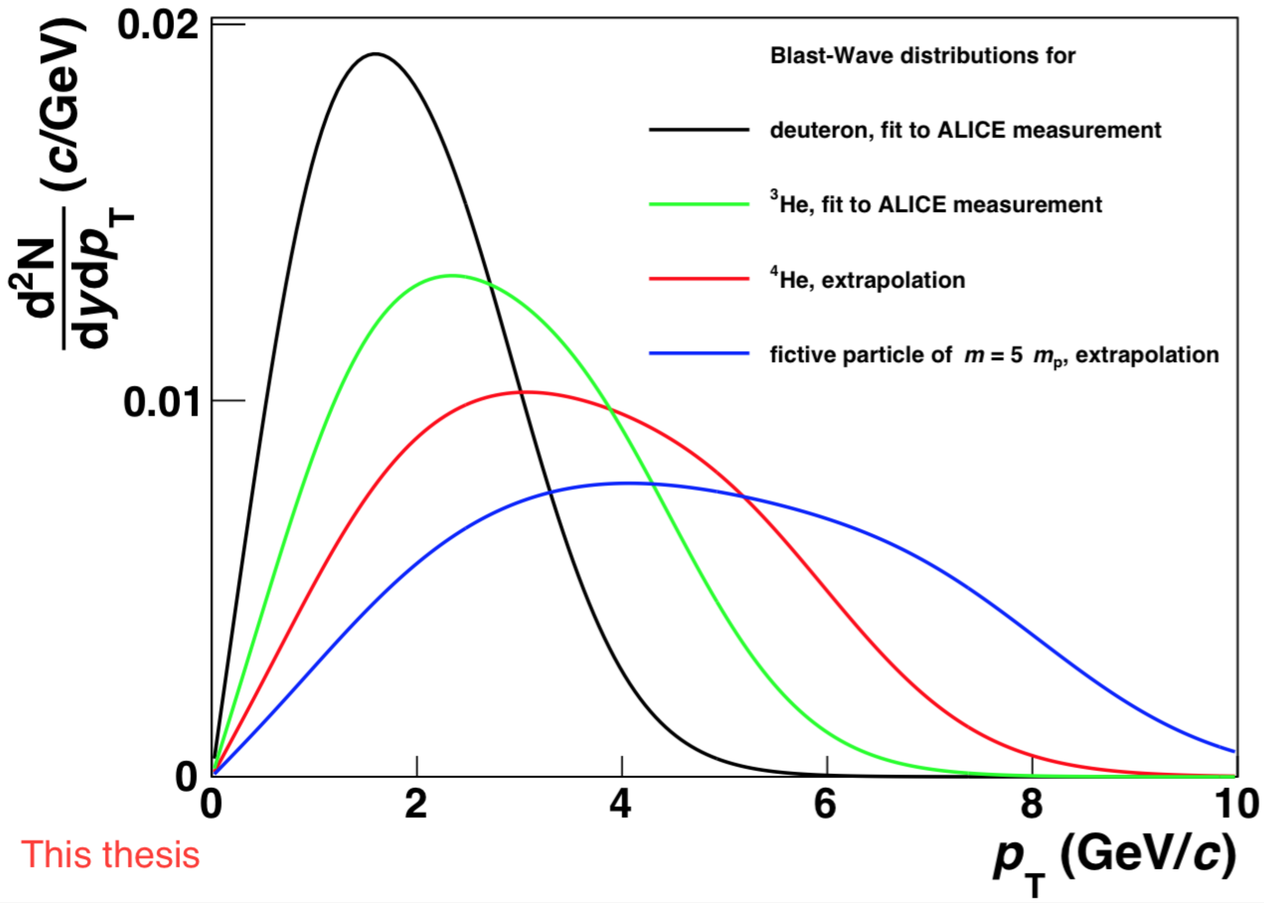

Figure 5.11: Blast-Wave distributions for deuterons (black), ^{3}He (green), ^{4}He (red) and a fictive mass 5 particle (blue). The Blast-Wave distributions for deuterons and ^{3}He are obtained by a fit to the measured spectra in Pb–Pb data. Whereas the curves for ^{4}He and a fictive mass 5 particle are extrapolations, which are based on the parameters obtained from the deuteron and ^{3}He fits. The integrals are normalized to one.

states (H-dibaryon and Λn bound state, see chapter 4). From the convolution of the efficiency with the Blast-Wave calculation one gets the true efficiency as the integral of the convoluted function shown in Figure 5.12. This leads to an overall p_T-weighted efficiency of 0.150 for alphas and 0.214 for anti-alphas. For this only the track cuts listed in Table 5.2 and the $p/z > 2$ GeV/c cut for alphas are taken into account. The other cuts (TPC nσ and TOF matching cut) are taken into account separately in the following section 5.3.1.

5.3.1 Efficiency and acceptance correction for the different cuts

The influence of the different TPC PID cuts and the TOF matching cut ($\pm 3\sigma$ cut in the dE/dx vs. $\beta\gamma$ distribution) on the Efficiency × Acceptance is studied. In order to take the TPC PID cut into account, the following method is used:
In a data driven approach the difference between the measured TPC signal for ^{3}He candidates and the theoretical Bethe-Bloch value for ^{3}He at the given momentum normalized to this value is obtained $\left(\mathrm{d}E/\mathrm{d}x_{\mathrm{TPC}} - \mathrm{d}E/\mathrm{d}x_{^3\mathrm{He}}\right) / \left(\mathrm{d}E/\mathrm{d}x_{^3\mathrm{He}}\right)$. The resulting distribution is fitted with a Gaussian. Now the percentage of counts inside the different investigated σ-ranges compared to the total number of counts in the histogram is calculated and the efficiency is weighted with the resulting percentage. The advantage of this method is, that it takes the tail on the right side of the distribution into account. The same

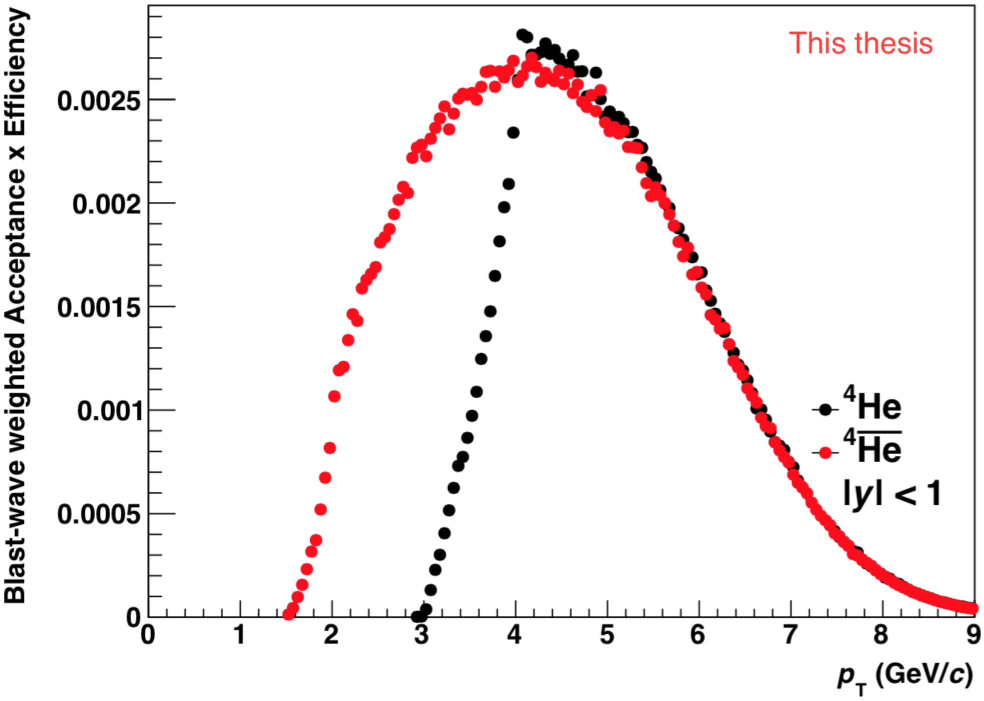

Figure 5.12: Convolution of the Blast-Wave calculation (Figure 4.8) with the extracted Acceptance x Efficiency distributions from Monte Carlo.

procedure is done to correct for the TOF matching cut. The resulting percentage in this case is 95.5 %, meaning the weighted efficiencies have to be reduced by 4.5 %. The results are summarized in Table 5.5.

5.4 Absorption

The possible absorption of the $^{4}\overline{\mathrm{He}}$ by the crossed material has been studied in the same way as for the $^{3}\overline{\mathrm{He}}$ in Pb–Pb [9]. This means, that the absorption is estimated by using the two different transport codes GEANT3 [61] and GEANT4 [62]. In order to take the absorption into account, the used GEANT3 is a slightly modified version compared to the standard. The measurements of anti-deuterons done at Serpukhov [63] were taken into account to implement an empirical optical model [64] for the absorption. Instead, in GEANT4 an implementation of a Glauber model is used, which is based on the measured hadronic interaction cross-section for (anti-)protons [65]. The final value for the absorption is taken

Sigma range TPC	Percentage of total yield	Alpha Weighted efficiency	 TOF matching corrected	 TPC $n\sigma$ corrected	Anti-Alpha Weighted efficiency	 TOF matching corrected	 TPC $n\sigma$ corrected	 Absorption corrected
-3σ to 3σ	94.9	0.150	0.143	0.136	0.214	0.204	0.194	0.180
-2.5σ to 3σ	94.1	0.150	0.143	0.135	0.214	0.204	0.192	0.179
-2σ to 3σ	92.2	0.150	0.143	0.132	0.214	0.204	0.189	0.175
-1.5σ to 3σ	88.3	0.150	0.143	0.126	0.214	0.204	0.180	0.168
-1.0σ to 3σ	79.8	0.150	0.143	0.114	0.214	0.204	0.163	0.152
-0.5σ to 3σ	65.2	0.150	0.143	0.093	0.214	0.204	0.133	0.124
0σ to 3σ	47.0	0.150	0.143	0.067	0.214	0.204	0.096	0.089

Table 5.5: Summary of the efficiency corrections due to the different nσ cuts in the TPC. For anti-alpha particles in addition the absorption correction is taken into account.

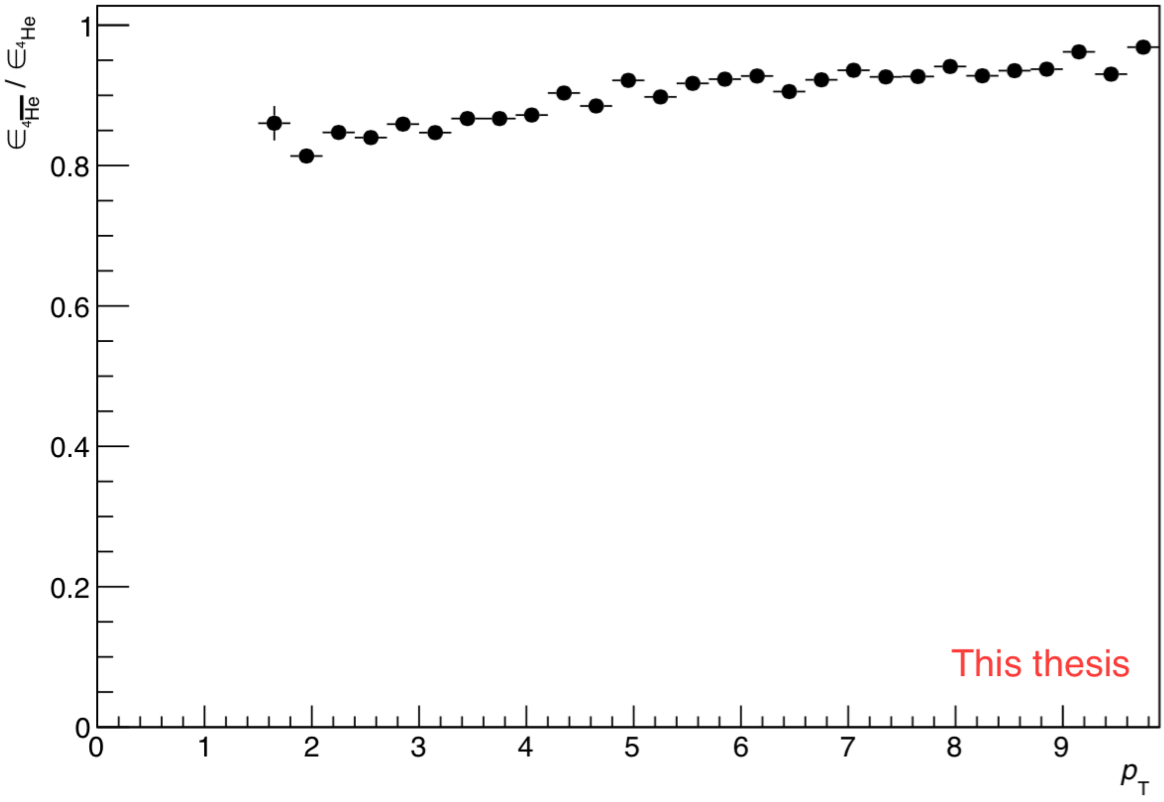

Figure 5.13: Ratio between the Efficiency x Acceptance of $^4\overline{\mathrm{He}}$ and ^{4}He using GEANT4.

from GEANT4, whereas the difference to the patched GEANT3 is taken as the systematic uncertainty. The resulting weighted efficiency, if using GEANT4, is 0.199 and the systematic uncertainty due to the poorly known absorption is 7 %. Figure 5.13 shows the difference between the efficiency of $^4\overline{\mathrm{He}}$ and ^{4}He using GEANT4. In the last column of Table 5.5 the Efficiency x Acceptance is reduced by 7% in order to correct for the absorption.

5.5 Corrected yield

The corrected yield is calculated using the following equation:

$$\frac{\mathrm{d}N}{\mathrm{d}y} = \frac{N_{^4\overline{\mathrm{He}},\,rec}}{N_{events} \cdot \text{efficiency} \cdot dy} \tag{5.2}$$

As the measurement is performed on a data set including central, semi-central and minimum bias triggered events and in a 0-80% centrality interval, this has to be corrected by the $\mathrm{d}N/\mathrm{d}\eta$ weighted with the number of events measured in each centrality class (see table 5.1):

$$\text{weighting factor} = \left(2.072 \cdot 10^7 \cdot 1447.5 + 1.740 \cdot 10^7 \cdot 749 + 0.063 \cdot 10^7 \cdot 86\right) / 3.874 \cdot 10^7 \approx 1112 \tag{5.3}$$

This leads to the final calculation of the yield of

$$\frac{\mathrm{d}N}{\mathrm{d}y}(0-10\%) = \frac{N_{^4\overline{\mathrm{He}},\,rec}}{N_{events} \cdot \text{efficiency} \cdot \mathrm{d}y} \cdot \frac{1447.5}{1112} \tag{5.4}$$

Sigma range TPC	Alpha Background corrected raw counts	Corrected weighted efficiency	dN/dy (0-10 %) $\times 10^{-7}$	Anti-Alpha Background corrected raw counts	Corrected weighted efficiency	dN/dy (0-10 %) $\times 10^{-7}$
-3σ to 3σ	5.72	0.136	7.06	8.75	0.180	8.14
-2.5σ to 3σ	6.37	0.135	7.94	8.40	0.179	7.89
-2σ to 3σ	6.03	0.132	7.67	9.07	0.175	8.69
-1.5σ to 3σ	5.03	0.126	6.68	10.03	0.168	10.04
-1.0σ to 3σ	6.35	0.114	9.33	9.68	0.152	10.72
-0.5σ to 3σ	3.35	0.093	6.03	9.21	0.124	8.14
0σ to 3σ	2.68	0.067	6.68	7.57	0.089	14.23

Table 5.6: Summary of dN/dy in 0-10%.

This way of weighting the yield assumes a constant ratio ^{4}He/π. Table 5.6 summarizes the obtained corrected yields.

5.6 Systematic uncertainties

In order to estimate the systematic uncertainty of the measured dN/dy depending on the efficiency and the measured counts in the m^2/z^2 distribution, the used cuts are varied systematically for Monte-Carlo and data. Table 5.7 shows how the efficiencies change when the variation of the track cuts is performed. This variation is done before taking into account the different factors for TOF matching (× 95.5 %), for the different nσ TPC cuts (× 94.9 % (-3 to 3σ) down to 47 % for 0 to 3σ) and in case of the anti-alpha also for the absorption correction (× 93 %). The total systematic uncertainties are summarized in Table 5.8. Figure 5.14 summarizes the dN/dy for all the different nσ TPC cuts together with the statistical uncertainties as vertical lines and the systematic uncertainties as boxes, in blue for alphas and in red for anti-alphas. The main contributions to the systematic uncertainty are:

- Unknown p_{T} shape → Blast wave convolution 13 %
- $p/z > 2$ GeV/c cut for alphas, around 4 to 13%
- Absorption correction for anti-alphas 7 %
- Remaining secondary contamination above $p/z > 2$ GeV/c for alphas of 1.3 counts leading to a uncertainty of 20 % to 49 %

Other contributions are

- The systematic uncertainty on the chosen TPC PID cut, varying between 1 and 19 %.
- The contributions from track cuts are negligible (< 1 %).
- The systematic uncertainty on the dE/dx vs. $\beta\gamma$ is varying between 1 and 18 %.

5.7 Final dN/dy

For the final values of dN/dy the mean of all the different cut sets is calculated. The mean value for alphas is $\mathrm{d}N/\mathrm{d}y_{^4\mathrm{He}} = (0.8 \pm 0.4\ (\mathrm{stat}) \pm 0.3\ (\mathrm{syst})) \times 10^{-6}$, whereas for anti-alpha the corresponding mean value is $\mathrm{d}N/\mathrm{d}y_{^4\overline{\mathrm{He}}} = (1.1 \pm 0.4\ (\mathrm{stat}) \pm 0.2\ (\mathrm{syst})) \times 10^{-6}$. The ratio anti-alpha/alpha is $1.4 \pm 0.8(\mathrm{stat}) \pm 0.5(\mathrm{syst})$.

Track Cut	**Value**	**Alpha efficiency**	**Anti-alpha efficiency**
Nominal value	not corrected for TPC PID, TOF matching and absorption	0.150	0.214
Minimum clusters TPC	80		
	70	0.150	0.214
	90	0.149	0.212
Maximum χ^2 per Cluster TPC	4		
	3	0.150	0.214
	5	0.150	0.214
Minimum cluster ITS	2		
	1	0.150	0.214
	3	0.148	0.212
DCA_{xy}	< 0.1 cm		
	< 0.05 cm	0.150	0.214
	< 0.15 cm	0.150	0.214
DCA_z	< 1.0 cm		
	< 0.5 cm	0.150	0.213
	< 1.5 cm	0.150	0.214
p/z	> 2 GeV/c		-
	> 1.5 GeV/c	0.196	-
	> 2.5 GeV/c	0.101	-

Table 5.7: Summary of the change of the efficiencies due to systematic changes of the track cuts and the rigidity cut.

	Systematic uncertainty	
Sigma range TPC	**Alpha**	**Anti-alpha**
-3σ to 3σ	30.7%	22.6%
-2.5σ to 3σ	26.6%	21.9%
-2σ to 3σ	25.8%	18.2%
-1.5σ to 3σ	33.0%	16.3%
-1.0σ to 3σ	31.5%	16.2%
-0.5σ to 3σ	45.7%	16.6%
0σ to 3σ	52.1%	17.3%

Table 5.8: Summary of the total systematic uncertainty for the different nσ TPC cuts.

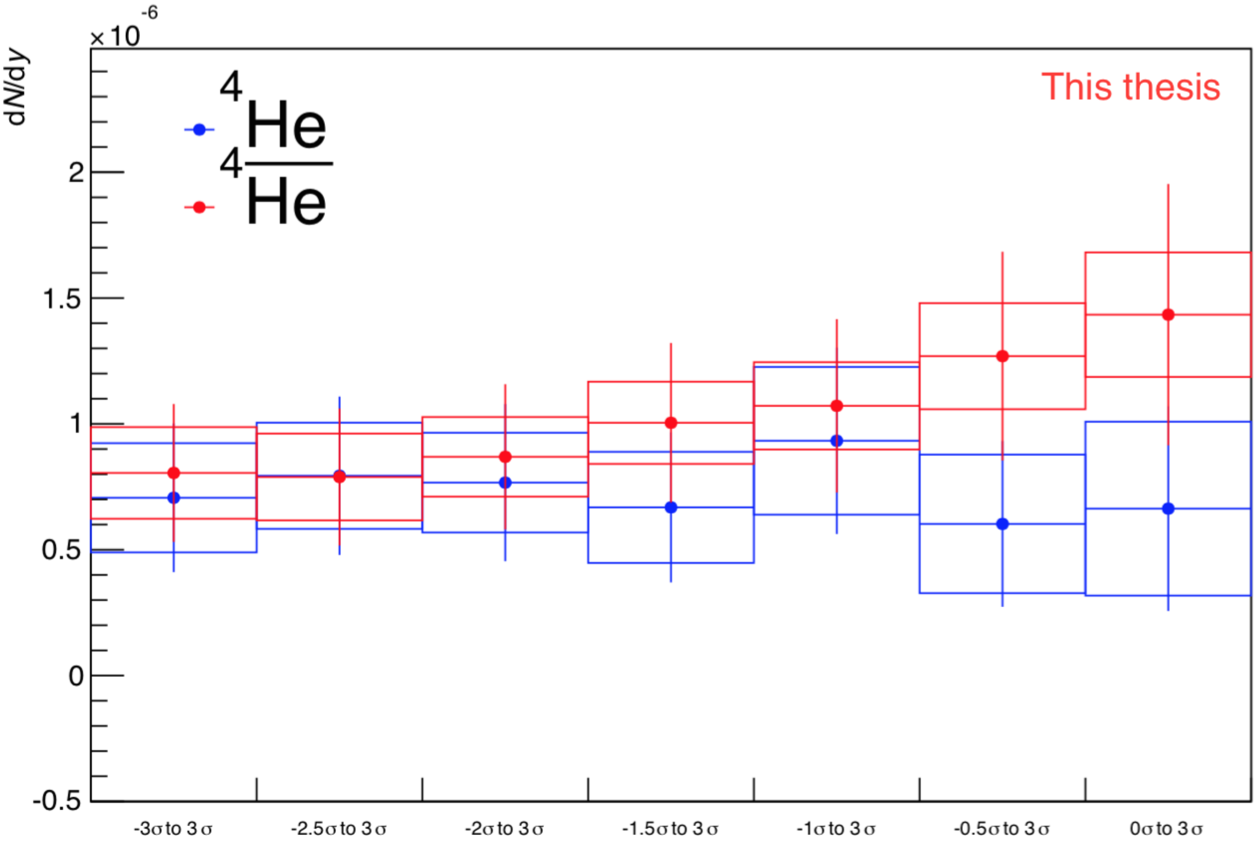

Figure 5.14: Summary of dN/dy in 0-10% for the different nσ cuts in the TPC. Blue for alpha and red for anti-alpha. The vertical lines represent the statistical uncertainties, whereas the boxes represent the systematic uncertainties.

6 Discussion

The search for the $\overline{\Lambda \mathrm{n}}$ bound state and for the H-dibaryon ($\Lambda\Lambda$) did not lead to the observation of a signal in the corresponding invariant mass distributions. Thus, upper limits on the production rate $\mathrm{d}N/\mathrm{d}y$ have been set. For the determination of the upper limits the branching ratio is needed. In order to cancel the uncertainty related to the unknown branching ratio, the upper limits have also been determined independent from the branching ratio. These results are shown as black lines in Figure 6.1. As these are the experimentally obtained results, they are constant values. The different theory predictions on the other hand are drawn for all theoretically possible branching ratios and are therefore not constant.

The following three theories have predictions for both exotic bound states: The non-equilibrium thermal model [66], its prediction is drawn in green. The predictions from the equilibrium thermal model [67] for a temperature of 164 MeV are shown in blue full line and for a temperature in 156 MeV in blue with a dashed line. The temperature of 156 MeV is the result of the current best fit to the available data [4], whereas the temperature of 164 MeV was the predicted temperature for LHC Pb–Pb collisions before data was available [68]. Finally, there is also a prediction from a hybrid UrQMD calculation [69], which is drawn in yellow. Available predictions for the H-dibaryon from coalescence models are shown in red. The full red line corresponds to a prediction which assumes quark coalescence, whereas the dashed red line shows the prediction that assumes hadron coalescence. Both coalescence predictions are taken from [70]. A short description of the different models was presented in chapter 1.

For a wide range of the branching ratio the obtained upper limits are well below the predictions from the different referred theories. The predictions are at least a factor of 5 above the obtained upper limits, if the branching ratio is greater than 5% in case of the $\overline{\Lambda \mathrm{n}}$ bound state or greater than 20% in case of the H-dibaryon.

For the branching ratio independent comparison to the different model predictions the lifetime of the exotic bound states was assumed to be the same as the one of the free Λ hyperon ($2.63\ \times 10^{-10}$s). Yet, the determined upper limits also strongly depend on the assumed lifetime, see Figure 6.2. For all investigated lifetimes the upper limits stay below the prediction of the thermal model for a temperature of 156 MeV, which is shown as a blue dashed horizontal line in Figure 6.2. Only for very long lifetimes, with a decay length of 2 or more meters, the upper limits for the H-dibaryon come close to the model prediction. However, it is very unlikely that the two investigated bound states have a lifetime which is much longer than the one of the free Λ hyperon and small branching ratios. Therefore, there the obtained limits are at least a factor 5 below the predictions.

On the other hand, alpha and anti-alpha particles have been observed. Although these particles are seldom produced, it was possible to measure the rapidity densities. The resulting $\mathrm{d}N/\mathrm{d}y$ corresponding to 0-10% centrality for alphas is $\mathrm{d}N/\mathrm{d}y_{^4\mathrm{He}} = (0.8 \pm 0.4\ (\mathrm{stat}) \pm 0.3\ (\mathrm{syst})) \times 10^{-6}$, whereas for anti-alpha particles the corresponding value is $\mathrm{d}N/\mathrm{d}y_{^4\overline{\mathrm{He}}} = (1.1 \pm 0.4\ (\mathrm{stat}) \pm 0.2\ (\mathrm{syst})) \times 10^{-6}$. This is good agreement with the prediction of the thermal model, which states 6.91×10^{-7} for a centrality of 0-10% and for a temperature of 156 MeV. The obtained rapidity densities $\mathrm{d}N/\mathrm{d}y$ are also in agreement with a penalty factor of about 300 for the $\mathrm{d}N/\mathrm{d}y$ for each additional nucleon, which has been previously observed for protons, deuterons and ^{3}He [9, 71]. Figure 6.3 summarizes all so far measured rapidity densities and shows in addition in blue exponential fits to the data points, which resulted in the penalty

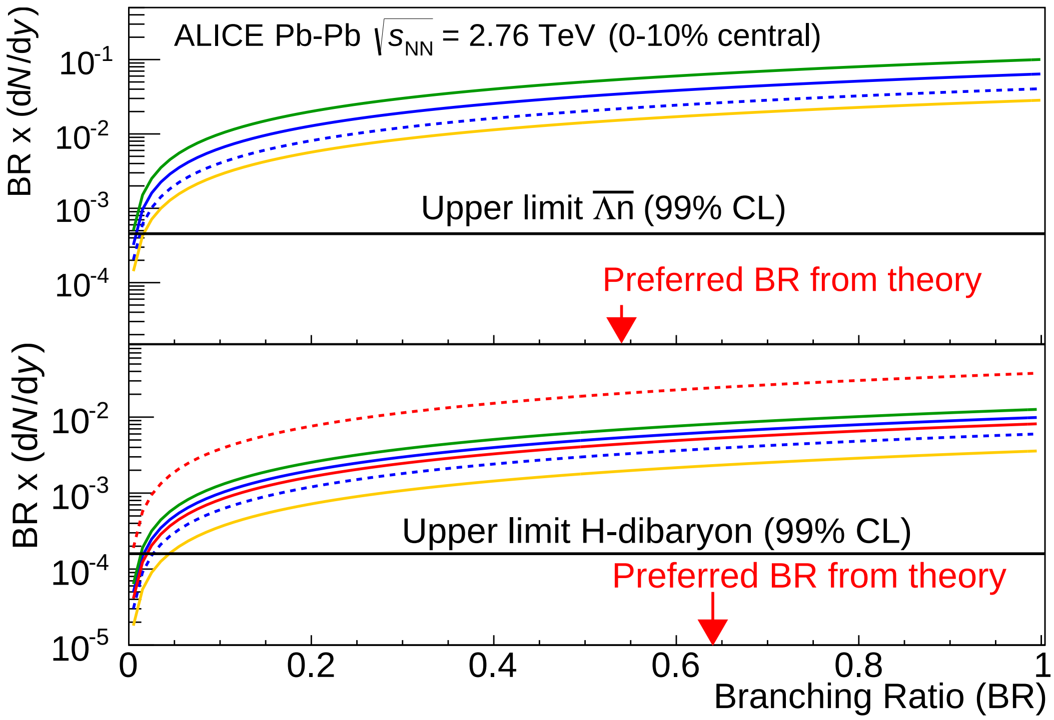

Figure 6.1: The BR × $(\mathrm{d}N/\mathrm{d}y)$ as function of the branching ratio (BR). In the upper panel for $\overline{\Lambda}$n and in the lower panel for ΛΛ. The upper limits, which have been determined under the assumption of a lifetime of the exotic bound states equal to the one of the free Λ hyperon, are shown in black lines. For these limits the branching ratio has not been taken into account. On the contrary, the theory predictions (colored lines) are drawn for all possible branching ratios. The color code for the different theories is explained in the text. The red arrows show the most likely branching ratio of 54% ($\overline{\Lambda}$n) and 64% (ΛΛ) taken from [57, 59]. The Figure has been also published in [55].

factor of about 300.

The very loosely bound hypertriton, which is a bound state of a proton, a neutron and a Lambda hyperon, has a separation energy of the Lambda from the deuteron of 130 keV and has also been measured with ALICE [6]. The determined $\mathrm{d}N/\mathrm{d}y$ is also in agreement with the thermal model prediction for 156 MeV.

In conclusion, the ALICE experiment has shown that it has the capability to measure particles with small production rates (alpha and anti-alpha particles) or loosely bound objects (hypertriton). Lighter nuclei (deuterons and ^{3}He) have also been measured already [9]. In all cases the determined rapidity densities are in good agreement with the predictions of the thermal model, see Figure 6.4. Therefore, one can also assume that the prediction for the production yield of the $\overline{\Lambda}$n bound state and of the H-dibaryon from the thermal model is as well reasonable and the existence of the two exotic bound states is questionable.

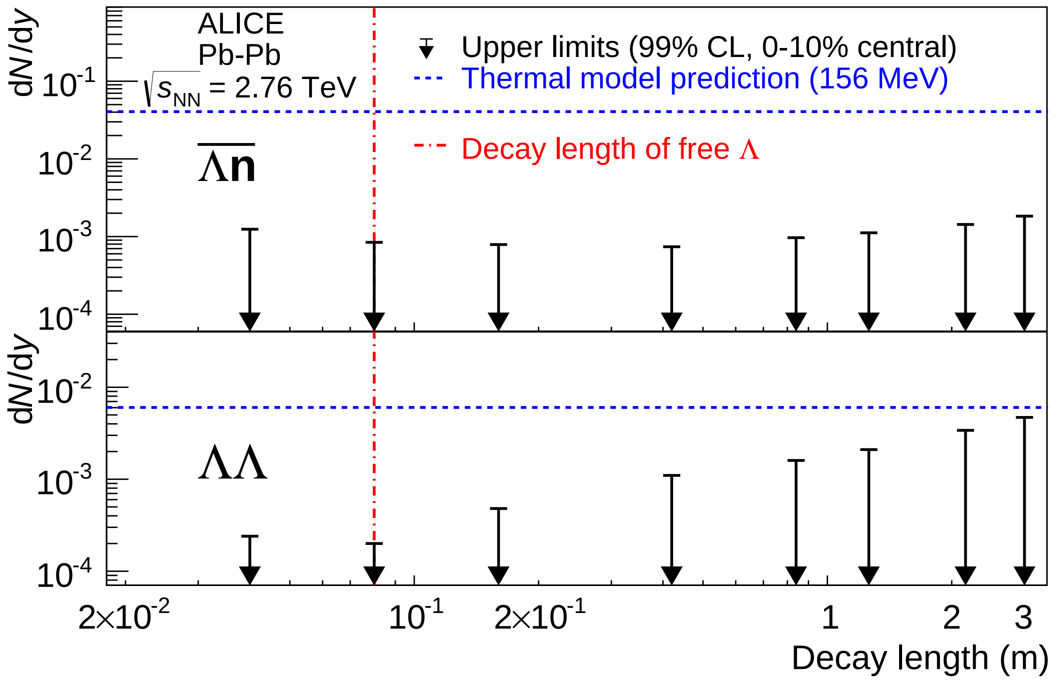

Figure 6.2: Upper limits as function of lifetime. For all lifetimes the assumed branching ratio is 54% for the $\overline{\Lambda n}$ and 64% for the H-dibaryon. The dashed blue horizontal line indicates the prediction of the thermal model for 156 MeV, whereas the dashed red vertical line indicates the lifetime of the free Λ-particle. The Figure has been also published in [55].

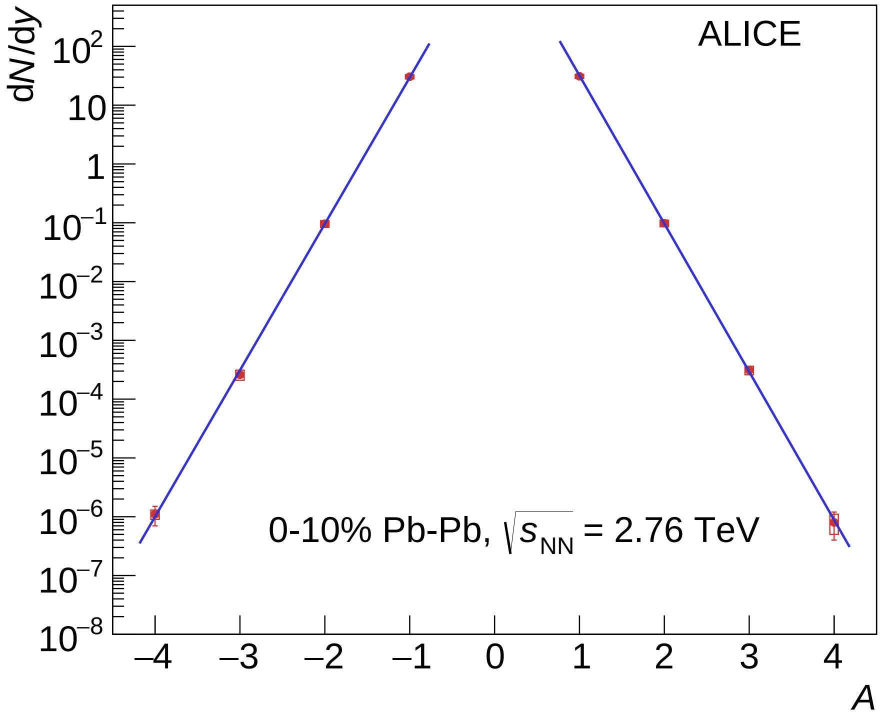

Figure 6.3: Summary of the so far measured nuclear rapidity densities $\mathrm{d}N/\mathrm{d}y$ for the nuclear mass number A. The blue lines are exponential fits to the data points, which results in a penalty factor of about 300 for each added nucleon. The $\mathrm{d}N/\mathrm{d}y$ for protons, deuterons and ^{3}He are taken from [9, 71]. The Figure has also been published in [72].

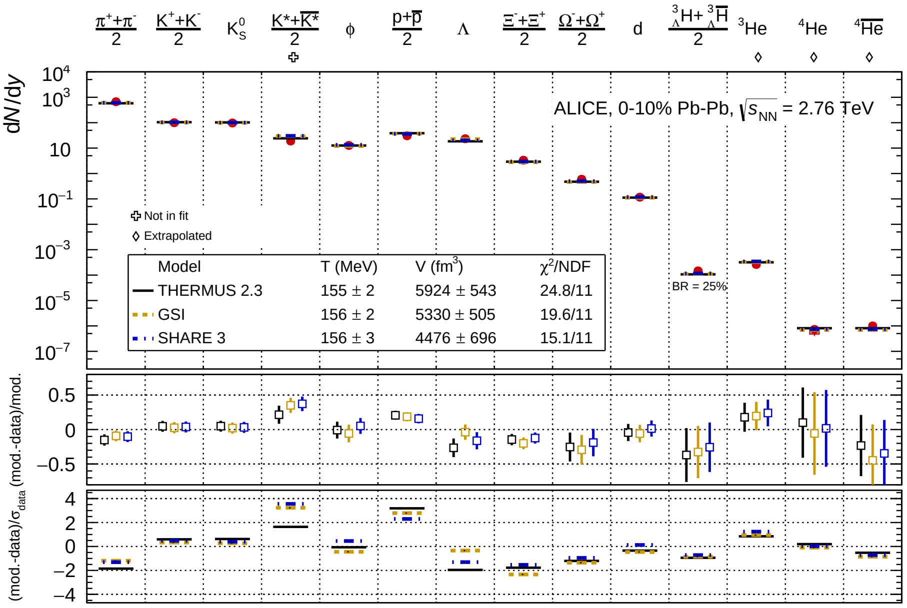

Figure 6.4: Fits of thermal models to ALICE data including for the first time also alpha and anti-alpha particles. For details see original publication [72].

7 Summary and Outlook

The knowledge of the existence of light bound states beyond the deuteron is of great interest for hadron physics. As the prediction of such states from theoretical considerations needs very high precision calculations, experimental investigations can help to improve the present understanding of the interaction between light baryons. Therefore, within this thesis a search for two exotic bound states has been performed. The H-dibaryon has been investigated in the decay channel $\mathrm{H} \rightarrow \Lambda + p + \pi^-$, whereas the search for the $\overline{\Lambda \mathrm{n}}$ bound state was based on in the decay channel $\overline{\Lambda \mathrm{n}} \rightarrow \overline{d} + \pi^+$. In both invariant mass distributions no signal has been observed, although the thermal model predicts around 25.000 $\overline{\Lambda \mathrm{n}}$ and depending on the binding energy between 440 (strongly bound) and 2800 (weakly bound) H-dibaryons for the investigated data ($19.3 \cdot 10^6$ events in a centrality range of 0-10% from the 2011 data set of Pb–Pb collisions at $\sqrt{s_{\mathrm{NN}}} = 2.76$ TeV). Upper limits on the rapidity densities have been set. For reasonable lifetimes and branching ratios these upper limits are well below different theory predictions from equilibrium, non-equilibrium, hybrid UrQMD and coalescence models.

The alpha and anti-alpha particles have been detected in 38.75 million Pb–Pb events in a mix of central, semi-central and minimum bias triggers. They are the heaviest nuclei produced and detected in a ultra-relativistic heavy-ion collision so far and the anti-alpha is the heaviest anti-nucleus which has ever been observed. The determined rapidity densities in 0-10% centrality are $\mathrm{d}N/\mathrm{d}y_{^4\mathrm{He}} = (0.8 \pm 0.4\ (\mathrm{stat}) \pm 0.3\ (\mathrm{syst})) \times 10^{-6}$ and $\mathrm{d}N/\mathrm{d}y_{^4\overline{\mathrm{He}}} = (1.1 \pm 0.4\ (\mathrm{stat}) \pm 0.2\ (\mathrm{syst})) \times 10^{-6}$. They are in good agreement with the prediction of the thermal model of 6.91×10^{-7} at a chemical freeze-out temperature of 156 MeV. This temperature was determined by fitting the already measured results of lighter particles. For the resulting temperature is does not matter much, if the nuclei are included in the fit or not. The ratio of anti-alpha/alpha is $1.4 \pm 0.8(\mathrm{stat}) \pm 0.5(\mathrm{syst})$. Within the substantial errors, this is in good agreement with the assumption that the same amount of matter and anti-matter is produced from the fireball as expected by thermal and coalescence models [73].

For higher precision measurements of the (anti-)alpha rapidity densities and the anti-alpha/alpha ratio more statistics is needed. This will be available with the new run 2, which has been started in spring 2015 after the long shut down 1. Further statistics will also be gained with run 3, which will start in 2021 after the long shutdown 2, which will begin in 2018. For run 3 for example, around 5500 alpha particles are expected in Pb–Pb collisions at $\sqrt{s_{\mathrm{NN}}} = 5.5$ TeV. This will not only decrease the statistical uncertainty, but will clearly also allow for the measurement of a transverse momentum spectrum. Therefore, the largest systematic uncertainty due to the lack of knowledge of the shape of the transverse momentum spectrum will be reduced. In addition, a new Monte Carlo simulation with much more statistics will be needed. This would decrease the uncertainty on the secondary correction for the alpha analysis, because with more statistics so called "template" fits are possible like they are already done for the deuteron analysis [9]. These fits allow for a more precise determination of the secondary contamination and therefore it will be possible to measure also alpha particles with a rigidity smaller than 2 GeV/c.

In addition, the measurement of the absorption of anti-deuterons has started with the available Pb–Pb data from 2011. This measurement will help to understand also the absorption of anti-^{3}He and anti-alpha. This knowledge will not only decrease the uncertainties, but it will help in understanding the interaction between matter and anti-matter. Further, the measurement of $\Lambda\Lambda$ correlations and the search for a possible Λnn bound state are already ongoing with the existing data. Although for the correlation measurement it also seems that more statistics will be needed. With the new data even more exotic bound states like the Ξp will be accessible, if they exist.

In conclusion, it has been shown that with the ALICE detector it is possible to measure rarely produced particles like the light nuclei as well as loosely bound objects as the hypertriton. All determined rapidity densities agree with the predictions of the 156 MeV thermal model. With the observation and the determination of the rapidity density of the hypertriton is has also been shown, that even very loosely bound objects survive the hot and dense medium. Therefore, also the H-dibaryon and the $\overline{\Lambda n}$ bound state should have been observed, if they exist.

List of Figures

Bibliography

[1] K. A. Olive et al. (Particle Data Group). *Chin. Phys. C*, 38, 090001 (2014) and 2015 update.

[2] A. Bazavov et al. Equation of state in $(2+1)$-flavor QCD. *Phys. Rev. D*, 90:094503, Nov 2014.

[3] S. Borsányi et al. Is there still any T_c mystery in lattice QCD? Results with physical masses in the continuum limit III. *JHEP*, 2010(9):1, 2010.

[4] M. Floris. Hadron yields and the phase diagram of strongly interacting matter. *Nuclear Physics A*, 931:103, 2014. QUARK MATTER 2014 XXIV international conference on ultrarelativistic nucleus-nucleus collisions.

[5] A. Bazavov et al. Chiral and deconfinement aspects of the QCD transition. *Phys. Rev. D*, 85:054503, Mar 2012.

[6] J. Adam et al. ${}^{3}_{\Lambda}\mathrm{H}$ and ${}^{3}_{\bar{\Lambda}}\overline{\mathrm{H}}$ production in Pb-Pb collisions at $\sqrt{s_{\mathrm{NN}}}$=2.76 TeV. *Phys. Lett. B*, 754:360 – 372, 2016.

[7] H. Agakishiev et al. Observation of the antimatter helium-4 nucleus. *Nature*, 473:353, 2011. Erratum ibid. 475:412, 2011.

[8] STAR Collaboration. Observation of an antimatter hypernucleus. *Science*, 328:58, 2010.

[9] J. Adam et al. Production of light nuclei and anti-nuclei in pp and Pb-Pb collisions at energies available at the CERN Large Hadron Collider. *Phys. Rev. C*, 93:024917, 2016.

[10] B. Abelev et al. Centrality dependence of π, K, p production in Pb–Pb collisions at $\sqrt{s_{\mathrm{NN}}} = 2.76$ TeV. *Phys. Rev. C*, 88:044910, 2013.

[11] B. Abelev et al. K^0_s and Λ production in Pb–Pb collisions at $\sqrt{s_{\mathrm{NN}}} = 2.76$ TeV. *Phys. Rev. Lett.*, 111:222301, 2013.

[12] B. Abelev et al. Multi-strange baryon production at mid-rapidity in Pb-Pb collisions at $\sqrt{s_{\mathrm{NN}}} = 2.76$ TeV. *Physics Letters B*, 728:216, 2014.

[13] B. Abelev et al. $\mathrm{K}^*(892)^0$ and $\phi(1020)$ production in Pb-Pb collisions at $\sqrt{s_{\mathrm{NN}}} = 2.76$ TeV. *Phys. Rev. C*, 91:024609, 2015.

[14] J. Weber et al. Neutron star interiors and the equation of state of ultra-dense matter. *AIP Conference Proceedings*, 892(1):515, 2007.

[15] H. Heiselberg. Phases of dense matter in neutron stars. In *6th Colloque Cosmologie Paris, France, June 16-18, 1999*, 1999.

[16] I. Vidaña. Hyperons and neutron stars. *Nuclear Physics A*, 914:367, 2013.

[17] D. Lonardoni, F. Pederiva, and S. Gandolfi. From hypernuclei to the inner core of neutron stars: A quantum monte carlo study. *Journal of Physics: Conference Series*, 529(1):012012, 2014.

[18] B. W. Downs and R. H. Dalitz. Analysis of the Λ-hypernuclear three-body systems. *Phys. Rev.*, 114:593, 1959.

[19] A. Budzanowski et al. High resolution study of the Λp final state interaction in the reaction p + p → K^+ + (Λp). *Phys. Lett. B*, 687:31, 2010.

[20] A. Budzanowski et al. Upper limits for a narrow resonance in the reaction p + p → K^+ + (Λp). *Phys. Rev. D*, 84:032002, 2011.

[21] C. Rappold et al. Search for evidence of $^3_\Lambda$n by observing d + π^- and t + π^- final states in the reaction of ^{6}Li + ^{12}C at 2A GeV. *Phys. Rev. C*, 88:041001, 2013.

[22] http://www.bnl.gov/hhi/files/talks/takehikosaito.pdf.

[23] R. L. Jaffe. Perhaps a Stable Dihyperon. *Phys. Rev. Lett.*, 38:195, 1977. Erratum ibid. 38:617, 1977.

[24] R. E. Chrien. H particle searches at Brookhaven. *Nucl. Phys. A*, 629:388c, 1998.

[25] B. H. Kim et al. Search for an H-Dibaryon with a Mass near $2m_\Lambda$ in $\Upsilon(1S)$ and $\Upsilon(2S)$ Decays. *Phys. Rev. Lett.*, 110:222002, 2013.

[26] L. Adamczyk et al. The ΛΛ Correlation Function in Au + Au collisions at $\sqrt{s_{\mathrm{NN}}} = 200$ GeV. *Phys. Rev. Lett.*, 114:022301, 2015.

[27] K. Morita, T. Furumoto, and A. Ohnishi. Lambda-Lambda interaction from relativistic heavy-ion collisions. *Phys. Rev. C*, 91:024916, 2015.

[28] T. Inoue et al. Bound Dibaryon in Flavor SU(3) Limit of Lattice QCD. *Phys. Rev. Lett.*, 106:162002, 2011.

[29] S. R. Beane et al. Evidence for a Bound H Dibaryon from Lattice QCD. *Phys. Rev. Lett.*, 106:162001, 2011.

[30] P. E. Shanahan, A. W. Thomas, and R. D. Young. Mass of the H Dibaryon. *Phys. Rev. Lett.*, 107:092004, 2011.

[31] J. Haidenbauer and U.-G. Meißner. To bind or not to bind: The H-dibaryon in light of chiral effective field theory. *Phys. Lett. B*, 706:100, 2011.

[32] P. Braun-Munzinger, K. Redlich, and J. Stachel. invited review in: R.C. Hwa, X.N. Wang Eds., Quark Gluon Plasma, vol. 3, World Scientific Publishing. arXiv:nucl-th/0304013.

[33] F. Becattini, J. Manninen, and M. Gaździcki. Energy and system size dependence of chemical freeze-out in relativistic nuclear collisions. *Phys. Rev. C*, 73:044905, 2006.

[34] A. Andronic, P. Braun-Munzinger, and J. Stachel. Thermal hadron production in relativistic nuclear collisions: The hadron mass spectrum, the horn, and the QCD phase transition. *Phys. Lett. B*, 673:142, 2009. Erratum ibid. 678:516, 2009.

[35] J. Cleymans and K.Redlich. Chemical and thermal freeze-out parameters from 1A to 200A GeV. *Phys. Rev. C*, 60:054908, 1999.

[36] A. Andronic. private communication. *model described in [68] and references therein*, 2013.

[37] G. Torrieri, S. Steinke, W. Broniowski, W. Florkowski, J. Letessier, and J. Rafelski. SHARE: Statistical hadronization with resonances. *Comput. Phys. Commun.*, 167:229, 2005.

[38] G. Torrieri, S. Jeon, J. Letessier, and J. Rafelski. SHAREv2: fluctuations and a comprehensive treatment of decay feed-down. *Comput. Phys. Commun.*, 175:635, 2006.

[39] S. T. Butler and C. A. Pearson. Deuterons from high-energy proton bombardment of matter. *Phys. Rev. Lett.*, 7:69, 1961.

[40] S. T. Butler and C. A. Pearson. Deuterons from high-energy proton bombardment of matter. *Phys. Rev.*, 129:836, 1963.

[41] H. Petersen, J. Steinheimer, G. Burau, M. Bleicher, and H. Stöcker. Fully integrated transport approach to heavy ion reactions with an intermediate hydrodynamic stage. *Phys. Rev. C*, 78:044901, 2008.

[42] E. Schnedermann, J. Sollfrank, and U. Heinz. Thermal phenomenology of hadrons from 200 A GeV S+S collisions. *Phys. Rev. C*, 48:2462–2475, Nov 1993.

[43] K. Aamodt et al. The ALICE Experiment at the CERN LHC. *JINST*, 3:S08002, 2008.

[44] CERN. *Website*, 2013. [Online] https://cds.cern.ch/record/1621583.

[45] L. Betev and P. Chochula. Definition of the ALICE Coordinate System and Basic Rules for Subdetector Components Numbering. *ALICE note ALICE-INT-2003-038*, 2003.

[46] K. Aamodt et al. Alignment of the ALICE Inner Tracking System with cosmic-ray tracks. *JINST*, 5:P03003, 2010.

[47] B. Abelev et al. Performance of the ALICE Experiment at the CERN LHC. *Int. J. Mod. Phys. A*, 29:1430044, 2014.

[48] J. Alme et al. The ALICE TPC, a large 3-dimensional tracking device with fast readout for ultra-high multiplicity events. *Nucl. Inst. Meth. A*, 622:316, 2010.

[49] ALICE Collaboration. Technical Design Report of the Time of Flight System. *CERN/LHCC 2000-012*, 2000.

[50] B. Abelev et al. Centrality determination of Pb-Pb collisions at $\sqrt{s_{NN}} = 2.76$ TeV with ALICE. *Phys. Rev. C*, 88:044909, 2013.

[51] ALICE Collaboration. Technical Design Report on Forward Detectors: FMD, T0, V0. *CERN/LHCC 2004-025*, 2004.

[52] H. Bethe. Zur Theorie des Durchgangs schneller Korpuskularstrahlen durch Materie. *Annalen der Physik*, 397:325, 1930.

[53] H. Bethe. Bremsformel für Elektronen relativistischer Geschwindigkeit. *Z. Phys.*, 76:293, 1932.

[54] W. Blum and L. Rolandi. *Particle Detection with Drift Chambers*. Berlin, Heidelberg, New York, 1993.

[55] J. Adam et al. Search for weakly decaying $\overline{\Lambda\mathrm{n}}$ and $\Lambda\Lambda$ exotic bound states in central Pb–Pb collisions at $\sqrt{s_{\mathrm{NN}}} = 2.76$ TeV. *Phys. Lett. B*, 752:267 – 277, 2016.

[56] B. Dönigus. Investigation Of Baryons With Strangeness And Search For Weakly Decaying Exotics With ALICE At The LHC. Dissertation, Darmstadt 2013.

[57] J. Schaffner-Bielich. private communication, calculation based on [59], 2012.

[58] R. Lea. Hypertriton production in Pb–Pb collision at $\sqrt{s_{\mathrm{NN}}} = 2.76$ TeV with ALICE at LHC - final results. *unpublished Analysis Note*, https://aliceinfo.cern.ch/Notes/node/259.

[59] J. Schaffner-Bielich et al. *Phys. Rev. Lett.*, 84, 2000.

[60] K. Aamodt et al. Centrality dependence of the charged-particle multiplicity density at midrapidity in Pb-Pb collisions at $\sqrt{s_{\rm NN}} = 2.76$ TeV. *Phys. Rev. Lett.*, 106:032301, 2011.

[61] R. Brun, F. Carminati, and S. Giani. GEANT detector description and simulation tool. 1994.

[62] S. Agostinelli et al. GEANT4: A simulation toolkit. *Nucl. Inst. Meth. A*, 506:250, 2003.

[63] V. V. Abramov et al. Production of deuterons and antideuterons with large pT in pp and pa collisions at 70 GeV. *Yad. Fiz.*, 45:1362, 1987.

[64] A. A. Moiseev and J. F. Ormes. Inelastic cross section for antihelium on nuclei: an empirical formula for use in the experiments to search for cosmic antimatter. *Astropart. Phys.*, 6:379, 1997.

[65] V. Uzhinsky et al. Antinucleus-nucleus cross sections implemented in GEANT4. *Phys. Lett. B*, 705:235, 2011.

[66] M. Petráň. private communication, based on [37] and [38], 2013.

[67] J. Stachel, A Andronic, P Braun-Munzinger, and K Redlich. Confronting LHC data with the statistical hadronization model. *J. Phys.: Conf. Series*, 509:012019, 2014.

[68] A. Andronic et al. Production of light nuclei, hypernuclei and their antiparticles in relativistic nuclear collisions. *Phys. Lett. B*, 697:203–207, 2011.

[69] J. Steinheimer. private communication, based on [74], 2013.

[70] S. Cho et al. Exotic hadrons in heavy ion collisions. *Phys. Rev. C*, 84:064910, 2011.

[71] B. Abelev and others. Pion, kaon, and proton production in central Pb-Pb collisions at $\sqrt{s_{\rm NN}}$=2.76 TeV. *Phys. Rev. Lett.*, 109:252301, Dec 2012.

[72] Shreyasi Acharya et al. Production of ^{4}He and $^4\overline{\rm He}$ in Pb-Pb collisions at $\sqrt{s_{\rm NN}} = 2.76$ TeV at the LHC. 2017. arXiv:nucl-ex/1710.07531.

[73] J. Cleymans et al. Antimatter production in proton-proton and heavy-ion collisions at ultrarelativistic energies. *Phys. Rev. C*, 84:054916, Nov 2011.

[74] J. Steinheimer, K. Gudima, A. Botvina, I. Mishustin, M. Bleicher, and H. Stöcker. Hypernuclei, dibaryon and antinuclei production in high energy heavy ion collisions: Thermal production vs. coalescence. *Phys. Lett. B*, 714:85, 2012.

Danksagung

Mein Dank gilt zu allererst Prof. Dr. Braun-Munzinger für die gute Betreuung und Begleitung bei meiner Doktorarbeit. Ich hatte immer das Gefühl, dass ich mit allen Fragen und Problemen zu ihm kommen kann. Dafür bin ich sehr dankbar. Das gilt natürlich auch für Priv.-Doz. Dr. Silvia Masciocchi, die sich immer sehr für mich eingesetzt hat und mir immer das Gefühl gegeben hat, in der Gruppe willkommen zu sein. Auch Priv.-Doz. Dr. Helmut Oeschler, dem ich meinen Dank leider nicht mehr persönlich ausdrücken kann, hat mich immer unterstüzt und auch in schwierigen Zeiten ermutigt, weiter an meinen Zielen zu arbeiten. Desweiteren möchte ich mich bei Prof. Dr. Guy Moore dafür bedanken, dass er sich bereit erklärt hat, der zweite Gutachter für meine Arbeit zu sein. Prof. Pietralla und Prof. Walther danke ich dafür, dass sie sich als Prüfer in meiner Kommission zur Verfügung stellen.

Mein besonderer Dank gilt Benjamin Dönigus, den ich immer mit all meinen Fragen löchern durfte. Auch wenn es sicher nicht immer einfach war, erinnere ich mich gerne an viele gemeinsame Stunden, oft bis spät Abends oder Nachts in denen wir gemeinsam gearbeitet haben, zurück. Auch Alexander Kalweit bin ich sehr dankbar. Nicht nur bei meinem Aufenthalt am CERN sondern insbesondere auch immerwieder zwischen durch, hat er mir wenn immer möglich und nötig bei den kleineren und gröÃ§eren physikalischen Problemen geholfen. Ich weiß, dass ich ohne die beiden heute nicht dort angekommen wäre wo ich jetzt bin. Herzlichen Dank.

Nicht zu vergessen natürlich die ganze GSI-ALICE Gruppe. Allen voran Dr. Ralf Averbeck, der mir nicht nur als mein Mentor in meinen PhD-Committee, mit gutem Rat geholfen hat. Sowie Krzysztof Redlich für seine Geduld und seine guten Ratschläge in meinem PhD-Committee. Dr. Anton Andronic, Dr. Marian Ivanov, Dr. Ana Marin, Dr. Dariusz Miskowiec, Dr. Jacek Otwinowski, Dr. Ilya Selyuzhenkov, Dr. Kai Schweda und Dr. Maria Nicassio vielen Dank für offene Ohren und immer wieder kritisches Nachfragen, sowie für viel Unterstützung. Es war sehr wichtig für mich zu wissen, dass ich immer jemandem habe an den ich mich mit meinen Fragen wenden kann.

Vielen Dank auch an Jochen Thäder, Mikolaj Krewicki, Markus Fasel, Markus Köhler, Michael Knichel, Jan Wagner, Jaap Onderwaater, Steffen Weber, Julius Gronefeld, Lukas Kreis, Alexander Deisting, Tona Bustamate und Edgar Perez für viele gemeinsame Stunden im Büro, bei Konferenzen und Workshops. Ohne euch wäre die Zeit nur halb so lustig und unterhaltsam gewesen.

Ich danke der ALICE Kollaboration, insbesondere den verschiedenen Convenern meiner "Physics Working Group" Dr. Michele Floris, Dr. Lee Stuart Barnby, Dr. Domenico Elia, Dr. Roberto Preghenella, Dr. David Dobrigkeit Chinellato, Dr. Francesca Bellini and Dr. Stefania Bufalino.

Ich danke der Helmholtz Research School H-QM und der Graduiertenschule HGS-HIRe für die Möglichkeit zur Teilnahme an diversen lecture weeks und Softskill Seminaren und für die Bereitstellung von Reisemitteln zu Konferenzen und meinen zweimonatigen Aufenthalt am CERN. Auch bei Sandra Schecker, Karin Stix und Denise Engel möchte ich mich für die Unterstützung, vor allem bei organisatorischen Angelegenheiten, bedanken.

Ganz besonderer Dank gilt meiner Familie. Insbesondere meinem Mann Bastian und meiner Tochter Mara. Ihr habt mich immer wieder aufgebaut und ich konnte mich auch in schwierigen Zeiten immer auf euch verlassen. Auch meiner Mama Inge, ihrem Lebensgefährten und meinen Ersatzpapa Matthias, meinen Schwestern Stefanie und Melanie, sowie meinen Schwiegereltern Elke und Ulli und meinem Schwager Timo bin ich sehr dankbar. Es ist für mich immer unendlich wertvoll zu wissen, dass ihr immer hinter mir steht und ich bin sehr froh und dankbar Teil einer so wunderbaren Familie zu sein.

Lebenslauf

Persönliche Angaben

Name	Nicole Alice Löher geb. Martin
Anschrift	Grillparzerstraße 4, 64291 Darmstadt
Geburtsdatum	7. November 1984
Geburtsort	Wiesbaden
Staatsangehörigkeit	Deutsch
E-Mail	nicole.loeher@l-dot.de

Ausbildung

2012–2018	Dissertation in Physik Technische Universität Darmstadt und ExtreMe Matter Institute EMMI and Research Division GSI Helmholtzzentrum für Schwerionenforschung
2008–2011	Master of Science in Physics der Technischen Universität Darmstadt
2005–2008	Bachelor of Science in Physics der Technischen Universität Darmstadt
2004–2005	Diplomstudium der Biologie Goethe-Universität Frankfurt am Main
2004	Abitur
2001–2004	Oberstufengymnasium Martin-Niemöller-Schule in Wiesbaden
1995–2001	Integrierte Gesamtschule Helene-Lange-Schule in Wiesbaden

Sprachkenntnisse

Deutsch	Muttersprache
Englisch	Verhandlungssicher in Wort und Schrift
Französich	UNIcert I

Darmstadt, 29. November 2018